Multiple Scattering Of Light In Inhomogeneous Media And Applications

2004

Claudia Mujat
University of Central Florida

MULTIPLE SCATTERING OF LIGHT IN INHOMOGENEOUS MEDIA AND APPLICATIONS

by

CLAUDIA MUJAT
B.S. University of Bucharest, 1994
M.A. Temple University, 1998
M.S. University of Central Florida, 2001

A dissertation submitted in partial fulfillment of the requirements
for the degree of Doctor of Philosophy
in the School of Optics
at the University of Central Florida
Orlando, Florida

Spring Term
2004

ABSTRACT

Light scattering-based techniques are being developed for non-invasive diagnostics of inhomogeneous media in various fields, such as medicine, biology, and material characterization. However, as most media of interest are highly scattering and have a complex structure, it is difficult to obtain a full analytical solution of the scattering problem without introducing approximations and assumptions about the properties of the system under consideration. Moreover, most of the previous studies deal with idealized scattering situations, rarely encountered in practice. This dissertation provides new analytical, numerical, and experimental solutions to describe subtle effects introduced by the properties of the light sources, and by the boundaries, absorption and morphology of the investigated media. A novel Monte Carlo simulation was developed to describe the statistics of partially coherent beams after propagation through inhomogeneous media. The Monte Carlo approach also enabled us to study the influence of the refractive index contrast on the diffusive processes, to discern between different effects of absorption in multiple scattering, and to support experimental results on inhomogeneous media with complex morphology. A detailed description of chromatic effects in scattering was used to develop new models that explain the spectral dependence of the detected signal in applications such as imaging and diffuse reflectance measurements. The quantitative and non-invasive characterization of inhomogeneous media with complex structures, such as porous membranes, diffusive coatings, and incipient lesions in natural teeth was then demonstrated.

To my son
Victor Mujat
and
to my sister
Raluca Popa

ACKNOWLEDGEMENTS

This was quite a journey, and there were times when I thought I will never make it. Somehow there was always somebody that extended a hand, an advice, a shoulder to cry on, or even a piece of candy to get me through the day. It's now time to recognize them.

I am grateful to my advisor, Dr. Aristide Dogariu, for making this a great learning opportunity. I thank him for guiding and advising me throughout the years, and for his inspiring dedication and intuition.

I thank Dr. ten Bosch for introducing me to the field of dental research, for teaching me to trust myself and my instincts, and for being always ready to share a good Dutch word of wisdom.

CREOL is a great place to study, do research and interact with peers. I extend my thanks to the outstanding faculty, my fellow students and to the friendly staff. As I will go on to the next step into my career, I will keep with me their teachings, friendship and support.

All the people in Random group, thanks for making me be a part of a great team. Lorrene, Adela and Gabi, thanks also for being great friends.

Finding yourself after nine hours of flight on South Street, Philadelphia, in a country that almost spans a continent can be an overwhelming experience. If not for my husband Mircea, I would have probably taken the first flight back. Thanks Mircea, for being there, then and now.

I got here mostly because of my parents and their love. Thank you very much, or as we say it in Romanian "Multumesc frumos". To my sister Raluca thanks for showing me the true meaning of strength. Victor, whatever you get to do in this life, do it because you want it, not because you can.

TABLE OF CONTENTS

LIST OF FIGURES

LIST OF TABLES

LIST OF SYMBOLS

a - particle radius, $[a] = m$;
C - speckle contrast; C - imaging contrast;
d - dimension of the particle, $[d] = m$;
D - diffusion coefficient, $[D] = m$;
$\mathbf{E}_i$ - incident electric field vector, $[\mathbf{E}_i] = V/m$;
$\mathbf{E}_o$ - electric field amplitude, $[\mathbf{E}_o] = V/m$;
f - scattering amplitude, $[f] = m$; f - volume fraction;
F_{rel} -relative fluorescence;
g - scattering anisotropy;
G - pair correlation function;
H_g - Henyey Greenstein distribution, $[H_g] = sr^{-1}$;
$H^{(2)}_{n+1/2}$ - Bessel function of the 2nd kind;
$\mathbf{J}$ - photon current density, $[\mathbf{J}] = m^{-2}s^{-1}$;
$J_{n+1/2}$ - Bessel function of the 1st kind;
$\mathbf{k}$ - wave vector, $[\mathbf{k}] = m^{-1}$;
l_c - coherence length, $[l_c] = m$;
l_s - scattering length, $[l_s] = m$;
l_a - absorption length, $[l_a] = m$;
l_t - transport mean free path, $[l_t] = m$;
L - thickness, $[L] = m$;
l - depth, $[l] = m$;
ml - mineral loss, $[ml] = vol\%$;
M - mass; $[M] = kg$;
$M(\omega)$ - spectral modifier;
n - refractive index;
OD - optical density;
$p(\mathbf{u}, \mathbf{u}_0)$ - scattering phase function;
$p_s(l)$ - probability density of scattering length; $[p_s(l)] = m^{-1}$;
$p(\theta)$ - probability density of scattering angle;
$p(I)$ - probability density function of the intensity;

P_r - scattered power density; $[P_r] = W/m^3$;

P_i - incident power density; $[P_a] = W/m^3$;

$P(s)$ - optical pathlength probability density; $[P(s)] = m^{-1}$;

q - degree of global coherence;

Q_{sca} - scattering efficiency;

$\mathbf{r}$ - position vector, $[\mathbf{r}] = m$;

r - Pearson correlation factor;

R - beam radius of curvature, $[R] = m$; R - modulus of position vector difference, $[R] = m$; R - reflectance;

s - optical pathlength, $[s] = m$;

S - spectral density;

$< s >$ - average optical pathlength;

t_c - drying time, $[t_c] = s$;

Tc – dimensionless decay time;

$T(\theta)$ - angular distribution of waves;

$\mathbf{u}$ - scattered unit vector;

$\mathbf{u}_0$ - incident unit vector;

v - speed, $[v] = m/s$;

V - volume, $[V] = m^3$;

W - cross spectral density;

w_0 - photon weight;

ϖ - beam width, $[\varpi] = m$;

Y - structure factor;

z - thickness, $[z] = m$;

z_e - extrapolation coefficient;

$d\Omega$ - differential solid angle, $[d\Omega] = srad$;

$\Delta F(\%)$ - fluorescence loss;

$\Delta\lambda$ - bandwidth, $[\Delta\lambda] = m$;

$\Delta(z)$ - expansion coefficient, $[\Delta(z)] = m$;

ΔZ - demineralization, $[\Delta Z] = vol\% \cdot \mu m$;

ε_r - electric permeability relative to vacuum;

φ - angular flux, $[\varphi] = m^{-2}s^{-1}sr^{-1}$; φ - azimuth, $[\varphi] = rad$;

Φ - phase of spectral degree of coherence; Φ - photon flux, $[\Phi] = m^{-2}s^{-1}$;

λ - wavelength, $[\lambda] = m$;

μ - spectral degree of coherence;

μ_a - absorption coefficient, $[\mu_a] = m^{-1}$;

μ_s - scattering coefficient, $[\mu_s] = m^{-1}$;

η - heterodyne detection efficiency;

Ω - solid angle, $[\Omega] = srad$;

ρ - number density, $[\rho] = m^{-3}$;

σ_I - width of spectral degree of coherence, $[\sigma_I] = m$;

σ_g - width of spectral density, $[\sigma_g] = m$;

σ_s - scattering cross section, $[\sigma_s] = m^2$;

σ_t - extinction cross section, $[\sigma_t] = m^2$;

σ_a - absorption cross section, $[\sigma_a] = m^2$;

σ_b - backscattering cross section, $[\sigma_b] = m^2$;

θ - scattering angle, $[\theta] = rad$;

ψ_n - Ricatti-Bessel function;

ζ_n - Ricatti-Bessel function;

CHAPTER 1

INTRODUCTION

Noninvasive diagnostics of inhomogeneous media is desirable for a wide range of applications, such as medicine, biology and material characterization. Recently, many such investigative methods have been developed and are starting to replace diagnostics tools that require sample acquisition and destruction, or exposure to high levels of damaging radiation. An important category of noninvasive methods, the light scattering-based techniques, make use of the interaction of light with matter for inferring desired characteristics of the observed medium. Most applications were developed for the characterization of particulate systems, specifically for determining their size, size distributions, index of refraction, shape and concentration. Various applications in medicine and biology have also emerged, such as, for example, measurements of the blood flow in either the capillary bed or the deep layers of tissue and tomographical imaging of different organs.

The light scattering process has been studied extensively, and has been the subject of numerous papers and books. However, as most media of interest are highly scattering and have a complex structure, obtaining a full analytical solution of the light propagation is practically impossible, as it is difficult to take into consideration all the scattering, absorption and interference effects that take place inside the medium. Thus, in all attempts at inhomogeneous media characterization through light scattering there are approxima-

tions and assumptions that have to be made about the properties of the system under consideration. A brief review of this assumptions and approximation is included in Chapter 2. Moreover, most of the studies and models were developed for idealized cases, rarely encountered in practical applications. Although their contribution is invaluable to the development of new diagnostic techniques, one must also consider the subtle effects that are induced by the particular characteristics of *"non-ideal"* inhomogeneous media. Accordingly, the aim of this dissertation is two-fold. First we will elaborate on the theoretical framework needed to describe the influence of certain particular characteristics of the light scattering system such as the properties of the radiative sources, scattering and absorption regimes, particle size distributions, and boundary conditions. We will then use the new knowledge in developing novel approaches for noninvasive characterization of different media of interest.

The properties of the radiative sources will influence the scattering regime in the inhomogeneous media under investigation. In many practical situations, laser sources are commonly used for light scattering experiments, because of their high power, directionality and coherence of the radiation. Moreover, the scattering processes have usually been described in terms of scattering of plane waves. More recently, however, it has been realized that there are certain advantages in using partially coherent sources, such as the capability of filtering out the multiple scattering component and decreasing the coherent noise, and/or increasing the imaging depth resolution in interferometric set-ups. Consequently, there is an increasing need to accurately describe the effects of the coherence of the light sources on the outcome of a scattering process. The influence of both the

spatial coherence, determined by the correlations between the fields emitted by different points across the surface of the source, and the temporal coherence, determined by the correlations between the fields emitted at different times, on the scattering process will be studied in Chapter 3. Monte Carlo simulations have been used extensively to study energy transport in multiple scattering media by taking advantage of the probabilistic nature of the light propagation in such media. In this technique, energy packets, i.e. photons, are sent one by one inside the scattering sample, and their trajectories are followed as they are scattered, reflected and/or absorbed in the medium. The statistical nature of the technique, however, has been considered the main impediment in treating wave coherent phenomena, as the photons are not being sent and followed all at once inside the medium. A novel approach for solving the problem of partially coherent beams propagating through scattering media numerically using Monte Carlo simulations, will be introduced in Chapter 3. We will show that, using Monte Carlo simulations, one can study the characteristics of beams with adjustable spatial coherence properties that propagate through highly scattering media. The method, subject to certain conditions and limitations that will be presented in detail, has the advantage of providing solutions for problems not covered by analytical descriptions and approximations. The influence of the temporal coherence of the source on the light scattering process, and in particular the bandwidth dependence of the heterodyne efficiency in a low coherence interferometry set-up, will also be addressed in Chapter 3. Low coherence interferometry is an optical technique that has been greatly developed over the last years, however, most of the models introduced to explain images of inhomogeneous media acquired with this technique

use a quasi-monochromatic description of the heterodyne detection process. We will show that, although neglected in current formalisms, the spectral changes induced by scattering alone will in general decrease the detection efficiency in a heterodyne detection process. The effect is stronger when the bandwidth of the incoming radiation is increased and it is dependent on the specific scattering system. Thus, the bandwidth dependence needs to be carefully considered when low coherence interferometry is used as a quantitative tool for characterizing inhomogeneous media.

The boundaries of the inhomogeneous medium will also affect the outcome of a scattering experiment. The diffusion approximation of light transport has been introduced to describe the propagation of light inside heavy multiple scattering media. Solving the diffusion equation for bounded media requires setting special boundary conditions, such that the behavior of the energy density at the interfaces is taken into account. Both the index contrast and the roughness of the boundary will influence the diffusion process. A careful analysis of the influence of the last scattering event on the diffusion process will be presented in Chapter 4. We will show using a Monte Carlo simulation, that for smooth boundaries, the scattering process close to the boundary is fundamentally different from the bulk diffusion, in the sense that it is affected by the scattering properties of the individual centers. Hence, the extrapolation length, introduced to describe the diffusion process for bounded media, is not only dependent on the refractive index contrast at the boundary, but depends also on the anisotropy of the scattering centers. We will also show that for rough boundaries, modeled as a single scattering layer, the spectral reflectance increases monotonically with the wavelength. Hence, despite strong bulk dif-

fusion, a wavelength dependence is practically generated through a mechanism other than absorption. The implications will be discussed in the context of several applications.

Absorption is yet another process that affects the outcome of a scattering experiment. To infer the scattering and absorption properties of inhomogeneous media, most existent techniques use either sophisticated time of flight configurations, or measurements of the diffuse reflectance and mean arrival time from a medium at different source-detector separation, or various modulation frequencies of the light source. In Chapter 4 we will asses the capability of simultaneous determination of scattering and absorption coefficients, using a single measurement of the pathlength distribution of light inside the sample, determined with optical pathlength spectroscopy. Moreover, we will study the absorption distribution inside the sample, which provides significant insights, since the realistic case where the absorbing centers are also the scatterers has barely been studied before.

Other problem that needs to be considered is the morphology of the investigated medium, as for example in samples consisting of interconnected network of pores or multiple layers with different optical properties. In Chapter 5, we will describe the novel use of optical pathlength spectroscopy and diffuse reflectance spectroscopy to quantitatively characterize structurally complex, highly scattering media, ranging from membrane filters and diffusive coatings to caries lesions in natural teeth enamel. For membrane filters, we will show that an important characteristic of the medium, the transport mean free path, can be recovered by fitting the pathlength resolved reflectance either with the results of the diffuse approximation in semi-infinite or bounded media, or with distributions obtained by Monte Carlo simulations. Different approaches are necessary depending on the thick-

ness of the membrane, as this will dictate the scattering regime in the sample. For diffuse coatings, we will show that, using optical measurements over a large range of wavelengths, one can obtain information on the pore size distribution of the pore structure as well as the porosity of the medium. Another porous medium of interest is dental tissue, and the non-invasive characterization of its demineralization is necessary for the correct assessment of a treatment plan. A basic understanding of the light scattering processes that take place inside the dental tissue (either sound or carious) will be obtained using both measurements of the photon pathlength distribution of light inside such media and Monte Carlo simulations. We will show that one can find correlations between the physical parameters of lesions and the moments of the pathlength distribution of light inside the samples, provided that the optical measurements are performed such that there is high refractive contrast at the tooth surface. Since the refractive index contrast inside the scattering sample will influence the strength of a scattering process, one would expect that monitoring the refractive index contrast changes in a scattering medium could bring additional knowledge on the properties of the medium under consideration. Accordingly, we will study the effects of drying on the optical pathlengths in natural incipient caries lesions, with the goal of quantifying the porosity of the surface layer of a lesion, and thus determine the speed at which the caries process will continue in time.

Final conclusions and a summary of the original contributions of this dissertation will be presented in Chapter 6.

CHAPTER 2

MULTIPLE LIGHT SCATTERING - AN OVERVIEW

This chapter reviews (1) the analytical approaches, (2) the investigative methods, and (3) the factors influencing the light scattering processes. Without trying to be exhaustive, the analytical approaches section describes the basic concepts of light scattering theory. Moreover, an introduction of the treatment of different scattering regimes is included. The investigative methods section includes a review of the experimental and numerical methods that have been used in this work. In the third section, several factors that influence the scattering process are considered. The direct problem of finding the field scattered from a given scattering center of known size, shape and composition is generally a complicated task. Due to the complex interferences of the fields scattered by different regions of the scattering center, the inverse problem of describing the scatterer as fully as possible from a suitable scattering experiment is even more complex. Nevertheless, solving the inverse problem is important in practice as it is the basis for the noninvasive characterization of inhomogeneous media and this is the main goal of this dissertation.

2.1 Analytical approaches

The concentration of scatterers and the number of scattering events that the light experiences before being detected influences considerably the outcome of a scattering

experiment. Although practical situations are generally more complicated, analytical solutions have been obtained for two limiting regimes, the single scattering and the multiple scattering one. A brief description of the concepts and approximations that are used to describes these two regimes are presented in the following.

2.1.1 Single scattering regime - scattering from a particle or a collection of particles

Let us assume that a plane wave $\mathbf{E}_i = \mathbf{E}_o \exp(i\mathbf{k}\cdot\mathbf{r})$ is incident on a scattering center of arbitrary size and shape. The scattering center is characterized by its relative dielectric constant, $\varepsilon_r(r) = \varepsilon_r'(r) + i\varepsilon_r''(r)$, with the real part describing the index of refraction and the imaginary part the loss properties. In the far field, at a distance R ($R >> d^2/\lambda$,with d the dimension of the particle and λ the wavelength of the radiation), where the amplitude and phase variations due to interferences of waves scattered by different parts of the scattering center can be neglected, the scattered field can be described by an outgoing spherical wave $\mathbf{E}_s = \mathbf{E}_o \frac{\exp(ikr_s)}{R} f(\mathbf{u},\mathbf{u}_0)$ [1]. Here $f(\mathbf{u},\mathbf{u}_0)$ is the so-called scattering amplitude and represents the amplitude, phase and polarization of the field scattered by the scattering center in the direction $\mathbf{u}$ when illuminated from direction $\mathbf{u}_0$ with a plane wave. A more commonly known and used quantity in light scattering theory is the scattering cross section, related to the scattering amplitude through the relation:

$$\sigma_s = \int_{4\pi} |f(\mathbf{u},\mathbf{u}_0)|^2 \, d\Omega \tag{1}$$

with $d\Omega$ being the differential solid angle. The scattering cross section has units of area, and describes the total power a scattering center will scatter at all angles. The total power

which is absorbed by a scattering center is described by the absorption cross section σ_a, and, finally, the sum of the scattering and absorption cross sections determines the total (extinction) cross section $\sigma_t = \sigma_s + \sigma_a$. Another commonly used quantity, especially in the radiative transfer theory, is the phase function

$$p(\mathbf{u}, \mathbf{u}_0) = \frac{4\pi}{\sigma_t} \left| f(\mathbf{u}, \mathbf{u}_0) \right|^2 , \tag{2}$$

which describes the anisotropy of the scattering process.

Finding the field scattered by a scattering center that is being illuminated by a given incident field implies solving Maxwell's equations with the appropriate boundary conditions. However, there are approximations that can be made depending on the size of the scattering center, its dielectric constant and the wavelength of the incident field [2], [3]. One simplification can be introduced when the size d is very small compared to the incident wavelength ($d << \lambda$). In this regime, called the Rayleigh scattering regime, the field inside the scattering center can be assumed to be uniform, hence, the angular dependence of the scattered field is the same as for an electric dipole oriented along the direction of the field inside the scattering center. In Rayleigh approximation, the scattering cross section becomes inverse proportional to the fourth power of the wavelength, i.e. shorter wavelengths suffer stronger scattering, and proportional to the square of the volume. In the Rayleigh-Gans regime, assumptions are made not only on the relation between the size and the wavelength, but also on the dielectric constant of the scattering center. Specifically, the dielectric constant has to satisfy the relation $|\varepsilon_r - 1| << 1$, and the restriction on the size is somewhat relaxed such that $d << \frac{\lambda}{(\varepsilon_r - 1)}$. In these conditions,

the scattering amplitude is proportional to the Fourier transform of $(\varepsilon_r - 1)$ evaluated at $k_s = 2k\sin(\frac{\theta}{2})$, and the scattering is not isotropic anymore, like in the Rayleigh regime. A rigorous solution for spherical particles that are not subject to the above restrictions has been found by Mie in 1908. His solution for the scattering cross section, for spheres of arbitrary radius a, is a complicated function of Ricatti-Bessel functions ψ and ζ

$$\begin{aligned} \psi_n(z) &= (\frac{\pi z}{2})^{1/2} J_{n+1/2}(z) \\ \zeta_n(z) &= (\frac{\pi z}{2})^{1/2} H^{(2)}_{n+1/2}(z) \end{aligned} \tag{3}$$

of arguments ka and $k\varepsilon_r a$. Here, $J_{n+1/2}$ and $H^{(2)}_{n+1/2}$are the Bessel functions of the first kind and second kind, respectively. For example, a Mie solution of the scattering efficiency $Q_{sca} = \frac{\sigma_s}{\pi a^2}$ for spheres of refractive index 1.5 and no absorption as a function of the size parameter ka is illustrated in Figure 2.1.

In practical applications however, we are often confronted with scattering by collections of scattering centers. Considering only single scattering allows considerable simplifications in the study of light scattered by such collections of scattering centers. In this approximation, the total scattered field is sufficiently small such that each center scatters the incident field independent of the other scattering centers, and the total scattered field is obtained as a sum of the contributions from each scattering center. Accordingly, if P_i is the incident power density on a collection of identical scattering centers of number density ρ and scattering amplitude $f(\mathbf{u}, \mathbf{u}_0)$, the total scattered power density from a volume dV at a distance R is given by $P_r = \frac{\rho |f(\mathbf{u},\mathbf{u}_0)|^2}{R^2} P_i dV$.

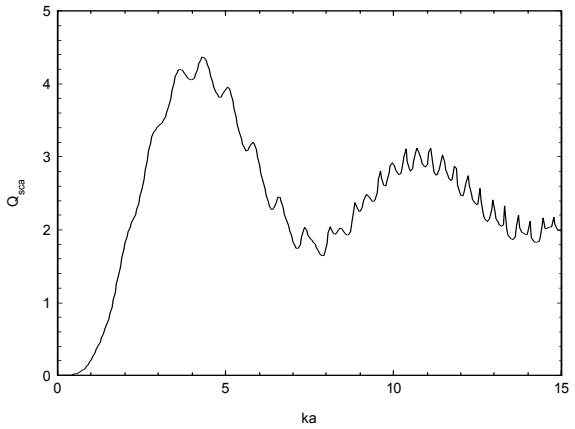

Fig. 2.1 Scattering efficiency Q_{sca} as a function of the size parameter ka for spheres with refractive index 1.5 and no absorption.

2.1.2 Multiple scattering regime - transport theory and the diffusion approximation

The single scattering approximation loses its validity as the concentration of scattering centers is increased and the scattered field becomes comparable with the incident one. In this case, light reaches the detector after being scattered at least several times and the field incident on each particle depends on the fields scattered by all the other scatterers. For this multiple scattering regime, a full solution of the light propagation is very complex, as it is very difficult to take into consideration all the scattering, absorption and interference effects that take place inside the inhomogeneous media.

A transport theory has been developed to describe multiple scattering in dense media, and deals directly with the energy transport in an inhomogeneous media [4]. Although diffraction and interference effects are considered for the scattering and absorption of a single particle, no interference effects are considered between fields scattered by different

particles. Transport theory's basic differential equation, similar to Boltzmann's equation, is obtained by balancing all the contributions to the photon density inside a volume V, and it is generally written in the form

$$\frac{1}{v}\frac{\partial\Phi(\mathbf{r},t)}{\partial t} + \nabla\mathbf{J}(r,t) + (\mu_s + \mu_a)\Phi(\mathbf{r},t) =$$

$$= \mu_a\Phi(\mathbf{r},t) + s(\mathbf{r},t). \tag{4}$$

Here, $\Phi(\mathbf{r},t)$ is the photon flux and $\mathbf{J}(r,t)$ the photon current density, which can be both expressed as a function of the angular photon flux $\varphi(\mathbf{r},\mathbf{\Omega},t)$ as

$$\begin{aligned} \Phi(\mathbf{r},t) &= \int_{4\pi}\varphi(\mathbf{r},\mathbf{\Omega},t)d\Omega \\ \mathbf{J}(\mathbf{r},t) &= \int_{4\pi}\mathbf{\Omega}\varphi(\mathbf{r},\mathbf{\Omega},t)d\Omega \end{aligned} \tag{5}$$

In the transport equation, the other quantities describing the source and the inhomogeneous media, respectively, are the photon source $s(\mathbf{r},t)$ and the scattering (μ_s) and absorption (μ_a) coefficients. The angular photon flux $\varphi(\mathbf{r},\mathbf{\Omega},t)$ is related to the density of photons $n(\mathbf{r},\mathbf{\Omega},t)$ that propagate within the solid angle interval $[\Omega,\Omega+d\Omega]$ through

$$\varphi(\mathbf{r},\mathbf{\Omega},t) = v\cdot n(\mathbf{r},\mathbf{\Omega},t) \tag{6}$$

with $v\cdot\mu_s$ being the frequency of interaction.

Generally, the transport equation can be solved only numerically; for an analytical solution further approximations are required. For instance, assuming that the angular flux $\varphi(\mathbf{r},\mathbf{\Omega},t)$ is only linearly anisotropic, i.e. from the expansion in Legendre polynomials of the angular flux only the two first terms are kept (the so-called P1 approximation),

$$\varphi(\mathbf{r}, \mathbf{\Omega}, t) \simeq \frac{1}{4\pi}\Phi(\mathbf{r}, t) + \frac{3}{4\pi}\mathbf{J}(\mathbf{r}, t) \cdot \mathbf{\Omega} \tag{7}$$

the source is isotropic, and the photon flux varies very slowly in time, a relation called Fick's law is found between the photon flux and the photon current density

$$\frac{1}{3}\nabla\Phi(\mathbf{r}, t) + \mathbf{J}(\mathbf{r}, t) = 0. \tag{8}$$

The P1 approximation mentioned above requires the absorption to be smaller than the scattering ($\mu_a << \mu_s^{'}$), mainly because it assumes a small intensity gradient, which is incompatible with large absorption. Inserting Fick's law into the radiative transfer equation (Eq.4), leads to the diffusion approximation for the photon flux $\Phi(\mathbf{r}, t)$:

$$\frac{1}{v}\frac{\partial\Phi(\mathbf{r}, t)}{\partial t} - D\nabla^2\Phi(\mathbf{r}, t) + \mu_a\Phi(\mathbf{r}, t) = s(\mathbf{r}, t), \tag{9}$$

where D is the diffusion coefficient ($D = \frac{1}{3\mu_s(1-g)}$) and g is the anisotropy factor defined as the average cosine of the scattering angle ($g = \int \mathbf{\Omega} \cdot \mathbf{\Omega'} p(\mathbf{\Omega}, \mathbf{\Omega'}) d\Omega$). For example, $g \to 0$ indicates an isotropic scattering event, while $g \to 1$ indicates an anisotropic, mostly forward scattering event. By solving Eq.9 with appropriate boundary conditions for the inhomogeneous media of interest, the reflectance or transmission of the medium can be obtained analytically. Again, it is important to emphasize that this equation holds only for dense scattering media, in the approximations that the angular photon flux is only linearly anisotropic, the source is isotropic, and the photon flux varies very slowly in time.

2.2 Investigative methods

Both experimental and numerical techniques have been used as investigative methods for the inhomogeneous media characterizations, and they are described in detail below.

2.2.1 Experimental techniques

Light scattered by inhomogeneous media has been used extensively in the last decades for the characterization of either the light source or the medium when the properties of the other one were known. Most experiments examined the angular spectrum, the polarization or the coherent properties of the optical waves transmitted by the inhomogeneous medium. Single scattering, diffusive and more recently sub-diffusive regimes of light scattering have been tackled.

The light scattering characterization techniques I have used in this work are ballistic attenuation of light in single scattering colloids, for the characterization of absorption in colloidal suspensions, diffuse reflectance spectroscopy, for the characterization of diffuse coatings on transparent substrates and inorganic samples and optical pathlength spectroscopy, for the characterization of incipient caries lesions in natural teeth.

Ballistic attenuation of light in single scattering colloids - is a technique that measures the extinction of a beam when passing an attenuating medium (Figure 2.2). Because multiple scattering effects induce deviations from a Beer-Lambert type attenuation $I = I_0 \exp(-\mu_t z)$, with $\mu_t = \mu_s + \mu_a$ and z the thickness of the medium, the method can be

used only in the single scattering regime. A variable thickness cell is generally used to experimentally determine the extinction coefficients of particulate suspensions.

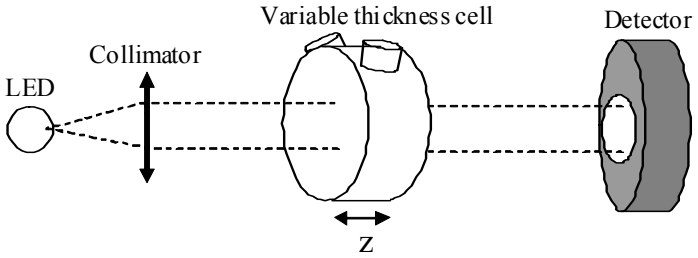

Fig. 2.2 Experimental set-up for measuring the ballistic attenuation of light in single scattering colloids

Diffuse reflectance spectroscopy - measures the wavelength dependent diffuse reflectance of a multiple scattering object with the help of an integrating sphere. A spectrophotometer equipped with an integrating sphere accessory has been used in these measurements. A brief schematic of the accessory is presented in Figure 2.3. The dual beam optics allows for simultaneous measurements of both sample and reference without moving samples.

Optical pathlength spectroscopy - uses the principles of low coherence interferometry to obtain information on the multiple scattering of light inside the sample, acquiring volume information on the scattering medium with very good resolution and significant dynamic range [5]. Due to its ability to experimentally determine the pathlength distribution $P(s)$ of waves inside the scattering medium, it has already been successfully used to investigate fundamental problems in scattering theory such as reflections at the boundaries and sub-diffusive regimes [6, 7].

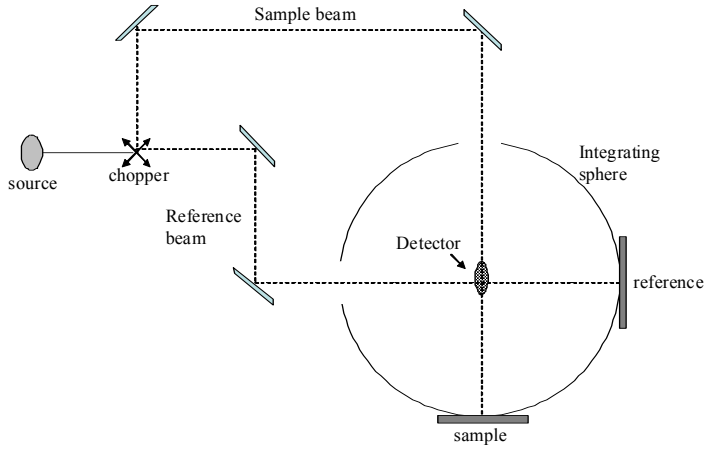

Fig. 2.3 Dual beam integrating sphere used for diffuse reflectance measurements

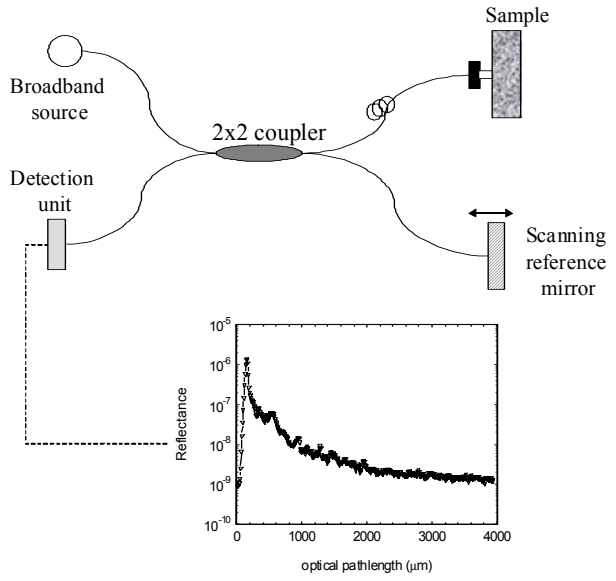

Fig. 2.4 Optical pathlength spectroscopy experimental set-up and typical reflectance curve obtained from a multiple scattering medium

The experimental set-up is basically an all fiber optic, low coherence interferometer (Figure 2.4), with a near IR ($\lambda = 1300nm$) low coherence ($l_c = 10\mu m$) light source. Light from the source is split into a reference and a probe beam, which, after being retroreflected from the reference mirror and scattering sample respectively, are recombined into a detector that measures their interference. Adjusting the position of the reference mirror, waves that have traveled a specific pathlength inside the medium are detected. Very high resolution ($\simeq 20\mu m$) in measuring the optical distance is achieved due to the low coherence of the source, while the heterodyne detection increases considerably the dynamic range of the measurement ($90dB$). A typical reflectance versus optical pathlength curve is also included in Figure 2.4. After an initial peak that represents the specular reflection of the sample surface, the rest of the distribution corresponds to waves that have experienced multiple scattering inside the inhomogeneous media. The number of scattering events that the wave experienced before being detected is directly correlated with the position in the pathlength distribution curve.

2.2.2 Monte Carlo simulation procedures

Whenever a complete analytical description of a phenomenon is either not available, or very complicated numerical experiments are sometimes the only viable approach. Among the wide range of numerical methods developed up to now, the Monte Carlo simulation (MCS), uses statistical sampling, i.e. sequences of random numbers, to give approximate solutions to a physical problem. Problems that have or have not a probabilistic content,

from very diverse fields, can be solved as long as the system under consideration is described by probability density functions (PDF). The statistical error in the results can be predicted, and generally many realizations (trials) are needed in order to have a very low statistical error, increasing significantly the computation time. However, many variance reduction techniques and parallelization algorithms have been recently developed to allow Monte Carlo methods to be implemented efficiently.

Light propagation in inhomogeneous media is inherently a random process, and the way a photon is scattered and absorbed can be described by corresponding PDF [8, 9, 10]. Moreover, inhomogeneities in scattering and absorption (multiple layers), boundary effects (refractive index contrast, roughness) and different sources (pencil beam, isotropic) can be readily introduced (Figure 2.5).

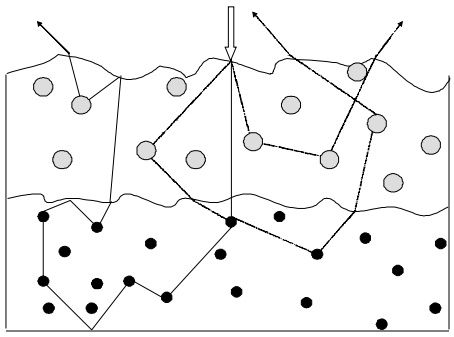

Fig. 2.5 General layout for a Monte Carlo simulation. Scattering, absorption, reflection at the boundaries, roughness and multiple layers can be considered. Three distinct trajectories of photons inside the medium are shown.

Generally, wave features such as phase and polarization are not accounted for in the simulations, as most MCS only deal with the energy transport in the inhomogeneous

medium. In Chapter 3, however, a novel approach is introduced to deal with random interferences specific to coherent propagation of light inside the inhomogeneous media.

Once the PDF for the problem at hand are known, random numbers are selected from these probabilities to determine the distance over which a photon will be either scattered or absorbed and its polar and azimuthal angles of scattering (Figure 2.6).

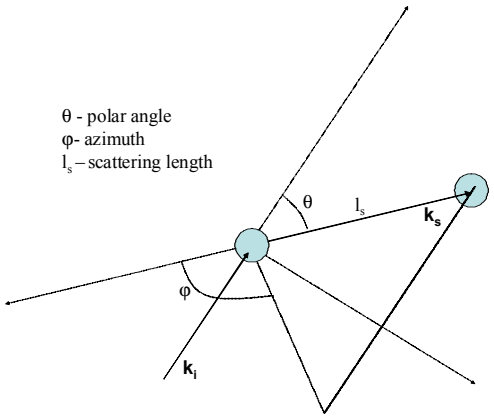

Fig. 2.6 Scattering geometry in spherical coordinates

Generally, the PDF that describe the scattering of a photon is given by

$$p_s(l) = \frac{1}{l_s} \exp(-\frac{l}{l_s}) \tag{10}$$

with $l_s = \frac{1}{\mu_s}$ being the scattering length. The azimuth φ is usually chosen from a flat $[0, 2\pi]$ distribution, as spherical symmetry is often assumed, while the polar angle is sampled from a flat distribution for particles that scatter isotropically, a Heyney Greenstein [11] one for particles that scatter mostly forward (Eq.11), or a combination of both, as the specific medium under consideration requires.

$$p(\theta) = \frac{1}{2\pi} \frac{1 - g^2}{(1 + g^2 - 2g\cos(\theta))^{3/2}} \tag{11}$$

Reflections at the boundaries are included using Fresnel relations averaged over different polarizations, when the polarization is not taken into consideration. Roughness can also be included as a random process, allowing photons that are encountering a boundary to *"see"* that boundary at angles given from a certain PDF, again characteristic to the problem at hand. Different ways of handling absorption in a MCS of light scattering have been introduced. In general, a weight is associated to each photon that enters the medium, and that weight is decreased in a specific manner as the photon propagates inside the medium. The photon is then terminated if its weight decreases under a certain value, or if its pathlength exceeds a pre-set propagation length.

In this work, the MCS has been used extensively either to look at effects that have been discovered both experimentally and analytical, or to understand experimental situations where an analytical description of the phenomena was not readily available. Moreover, insight was gained in specific problems of interest, even before any experiment was performed. The specifics of each of the simulations performed are described in the next chapters.

2.3 Factors influencing the light scattering process

In all attempts at inhomogeneous media characterization through light scattering there are approximations and assumptions that have to be made on the properties of

the system under consideration. These properties, that influence greatly the outcome of an experiment, include but are not limited at the coherence properties of the radiative source, scattering and absorption regimes, particle size distributions, and boundary conditions. The primary goal of the present work was to gain insight onto how these factors influence the outcome of a light scattering process, and consequently, to use light scattering measurements for a complete and accurate characterization of diverse inhomogeneous media.

2.3.1 Coherence properties of light sources

Fully coherent beams (both temporally and spatially) are an idealization; real sources are not perfectly monochromatic or spatially coherent. Moreover, some light scattering based techniques, such as low coherence interferometry, use broadband radiation to increase the resolution of the detection process. However, as the coherence of the radiative source is changed, the outcome of a scattering experiment might be influenced as well.

In terms of the spatial coherence of the radiative source, it has been recently shown both theoretically and experimentally that a partial coherent beam (PCB) will be degraded less by turbulence than a spatially coherent beam [12, 13]. Moreover, the spatial coherence properties of the radiative source will influence the speckle statistics at the exit surface of the inhomogeneous medium. Consequently, the effects of an inhomogeneous medium on the partially coherent beam propagation is a problem that is of interest in various fields, from atmospheric propagation to optical investigations on biological

materials. In Chapter 3, a novel Monte Carlo simulation is introduced to study the characteristics of beams with adjustable spatial coherence properties that propagate through highly scattering media.

The temporal coherence of the source needs also careful consideration. In response to the increasing interest in noninvasive techniques for in-vivo tissue imaging and characterization, low-coherence interferometry has been extensively used over the last years for imaging and characterization of tissue samples. In an attempt to improve the depth resolution of this interferometric technique, the bandwidth of the incident radiation has been increased considerably. In spite of this trend, all of the models introduced to explain images of heterogenous tissue, use a quasimonochromatic description of the heterodyne detection process [14, 15, 16]. Although this might not be problem for narrow-band sources (for example, a $30nm$ bandwidth at a central wavelength of $800nm$) one must cautiously describe the process for larger bandwidth-central wavelength fractions. The bandwidth influence on the heterodyne efficiency of a polychromatic interferometric system is also studied in Chapter 3.

2.3.2 Scattering and absorption

The scattering regime in a inhomogeneous media depends on the concentration of the scattering centers. For very low concentration of scatterers we have generally a single scattering regime, where the incoming light is scattered only once inside the medium and then is detected. Once the concentration starts increasing such that light suffers more

than two-three scattering events before detection, one deals with a multiple scattering regime. When the concentration of scatterers is very high, the scattering ceases to be independent, i.e. collections of particles may act as a single particle, and this is the so-called collective scattering regime (Figure 2.7). Each of these regimes have to be clearly identified before any attempt is made to obtain information on the inhomogeneous media Moreover, as the coherence properties of the radiative source are changed, the scattering regimes might change as well.

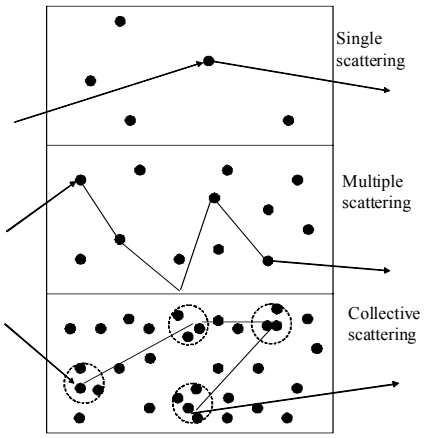

Fig. 2.7 Different scattering regimes: single scattering - light is only scattered once; multiple scattering - more than two, three scattering events; collective scattering - the scattering centers are so close that they act like a single, effective particle.

Absorption complicates greatly the interpretation of a scattering process in an inhomogeneous medium. For example, if the absorption is present at the level of scatterers, not only the amount of detected light is decreased, but the scattering efficiency of the scatterer and the phase function is modified as well (see Figure 2.8). Although there have been extensive studies on the influence of the surrounding medium absorption on the scattering process, there have been few studies of absorbing scatterers. However, for

biological media for instance the cells are both scatterers and absorbers. Two Monte Carlo simulation are developed in Chapter 4, to describe the two different regimes of absorption.

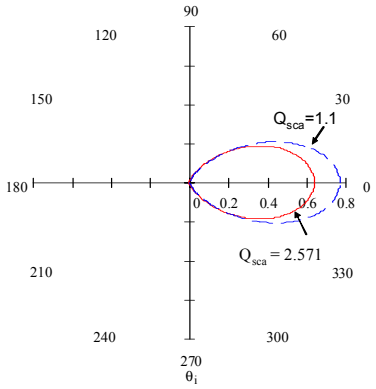

Fig. 2.8 Phase functions and scattering efficiencies for a $0.2\mu m$ spherical particle illuminated with $\lambda = 0.5\mu m$ when the particle is not absorbing $(n = 1.5 + 0.0i)$ - continuos line, and absorbing $(n = 1.5 + 0.5i)$ - dashed line

2.3.3 Size distributions

The monodispersivity of the scattering centers in an inhomogeneous media is, most of the time, an idealization, and size distributions have to be accounted for. Whenever the scattering is assumed to be independent, i.e. the scattering centers are so far apart that each scatters light independently, the scattering coefficient of the system μ_s is determined as the sum of the independent scattering coefficients μ_{s_i} with i denoting the size (r_i) of each scatterer.

As an example, Figure 2.9 shows the differences in between the phase function for a spherical particle and the equivalent phase function for a distribution with the average size

equal to the one of the particle. Understanding the influence of the particle size distribution on the scattering process is important, for example in the diffusive coatings industry, such as paper or paint industry, where predictive knowledge on the optical properties of the finite product from a given composition (chemical and size) of the diffusers would greatly improve the development process. A novel technique for the non-invasive characterization of the pore size distributions and porosities in diffusive coatings is presented in Chapter 4.

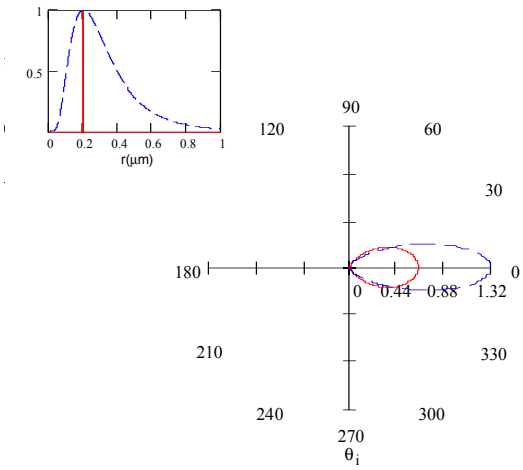

Fig. 2.9 Phase functions for $0.2\mu m$ spherical particle (continuos line) and a distribution of particles (dashed line) with average size $0.2\mu m$ illuminated with $\lambda = 0.5\mu m$. The upper left corner of the image shows the distribution of sizes.

2.3.4 Boundary conditions

Roughness and refractive index contrast at the boundaries of an inhomogeneous medium will influence the way light is transmitted and reflected at the boundaries. For example, for a high refractive index at the boundary, light can be reinjected through total

internal reflection into the medium and thus forced to scatter more. Due to this effect, in diffusive processes, an extrapolation length has to be defined in order to specify correctly the boundary conditions while solving the diffusion equation (Figure 2.10).

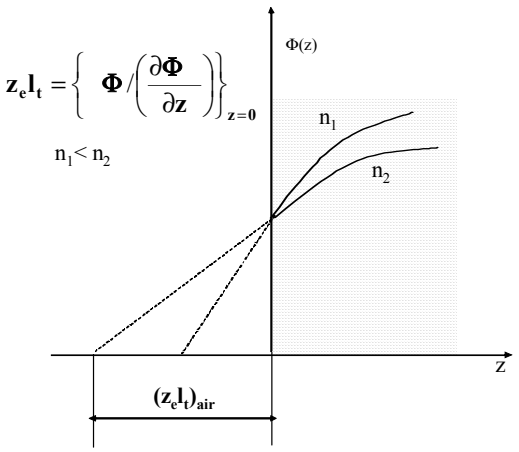

Fig. 2.10 The extrapolation length, needed to define the boundary conditions when solving the diffusion equation, is increasing as the refractive index contrast at the boundary increases due to total internal reflection effect.

Whether the value of this extrapolation length is influenced only by the refractive index contrast or by the size of the scatterers as well is a problem that has been greatly debated recently [17, 18, 19]. Moreover, rough layers at the surface of an otherwise ideal diffusing system will also influence the outcome of the scattering measurements. A Monte Carlo simulation is developed in Chapter 4 to describe the influence of the anisotropy of the scattering center on the extrapolation length. Moreover, a novel model is introduced in the same chapter to account for roughness at the boundary, modeled as a last scattering event.

CHAPTER 3

PROPERTIES OF THE RADIATIVE SOURCE

As briefly described in Chapter 2, Section 2.3.1, the coherence of the radiative source is expected to influence the outcome of a scattering experiment. This chapter studies this influence, as determined by both spatial and temporal aspects of the source coherence.

3.1 Statistics of partially coherent beams: a numerical analysis

The analysis of partially coherent beams propagating in scattering media has been attempted both analytically and numerically. However, due to the complexity of the problem, there are many obstacles that have to be overcome, such as the description of the complex interferences that occur between fields scattered by different scattering centers and the boundary effects. Here, we present a way to solve this problem numerically using Monte Carlo simulations (MCS). The new method, subject to certain conditions and limitations that will be presented in detail below, has the advantage of providing solutions for problems not covered by analytical descriptions and approximations. Moreover, a single simulation for a given optical density (OD) and anisotropy is used for the characterization of any light beam/scattering system interaction, for any degree of coherence of the input beam.

Light propagation through multiple scattering media is a random process, thus, it can be characterized using the probability density function defined in Section 2.2.2. MCS make use of this probabilistic behavior to determine, generally, the energy transport inside such media [8]. Energy packets, i.e. photons, are sent one by one inside the scattering sample, and their trajectories are followed as they are scattered, reflected and/or absorbed in the medium. Depending on the physical quantities to be scored with the MCS, record is kept of different photon characteristics such as optical pathlength and coordinates of exit point. Due to the probabilistic nature of the processes, a high number of photons is usually required to obtain good statistics. A more detailed description of the MCS for light scattering has been presented in Section 2.2.2.

Although MCS have been used extensively to study energy transport in scattering media, they have been rarely used in treating wave coherent phenomena. There are few notable exceptions. Coherent backscattering [20] has been treated with MCS without accounting for any "photon interferences", since the shape of the coherent backscattering cone is given by the Fourier transform of the radial intensity distribution. The heterodyne detection processes were treated with MCS [21, 14] by introducing criteria that a photon must meet in order to contribute to the detected signal. The wave properties of light have been incorporated in a MCS when studying the effects of diffraction in pulsed laser scanning microscopy through a scattering medium [22]. More recently, the mechanisms of ultrasonic modulation of multiply scattered coherent light have also been studied with this technique [23], good agreement with an independent diffusion-based analytical model being obtained. The approach was to let the photon accumulate phase by propagation and

other mechanisms. This procedure of simply attaching phase information to the photons has been disputed [24], as MCS of light propagation in a scattering medium is describing the photon-medium interactions as random processes characterized by a set of probability functions. Moreover, interference effects inside the scattering media cannot be accounted for since the photons are not being sent and followed all at once inside the medium.

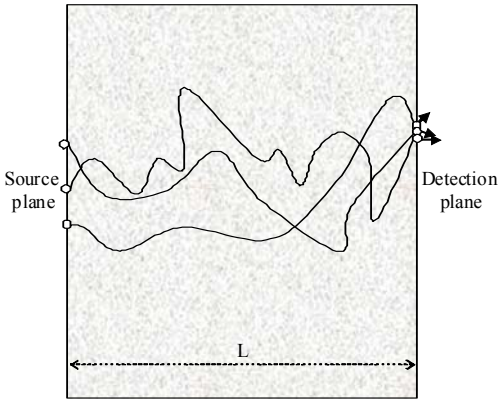

Fig. 3.1 Distribution of paths inside the scattering medium generated through the MCS approach

Indeed, attempting to analyze the intensity distribution of light inside an inhomogeneous medium when interference effects are at play is a complex problem that can be solved rigorously using Maxwell equations together with appropriate boundary conditions. Without considering the exact field distribution within the medium, one can formulate some of the properties at the exit interface by adopting an "optical fibers model". Accordingly, we can think at the MCS as a way to provide the statistics of paths that light will follow inside a scattering medium. All these paths can be considered as a collection of optical fibers that connect the source to the detection plane. Geometrical phase will be accumulated due to propagation along the fibers, and, depending on the coherence

properties of the source, interference effects will be observed when any number of these fibers cross in the detection plane (Figure 3.1).

Due to the linearity of the optical processes, even if the fibers cross inside the medium, the outcome at the output plane should not be influenced. In this MCS context, a photon can be used to trace the length, i.e. the accumulated geometrical phase, and the start/end positions of such optical fibers. Moreover, initial phases added to the photons could account for the coherence properties of the light source. Using the suggested MCS approach, in the following we investigate the intensity fluctuations at the output face of the scattering medium. Although the intensity fluctuations will be influenced by polarization effects, for the purpose of this study we consider only a scalar description of the coherent effects. Moreover, the change in the scattering phase function due to illumination with partially coherent beams is not taken into consideration as the simulation deals with rotationally invariant scatterers [25].

3.1.1 A photon description of the wave interference

The theory of partially coherent beams propagation can be described in either the space-time domain or space-frequency domain. However, for the purpose of studying the interaction with scattering media, usually described by frequency-dependent scattering potentials, the space-frequency domain is the method of choice [26]. The spectral interference law given by the Eq. (12) shows that, in general, the spectral density of the light at the interference site can be considerably different from the sum of spectral densities

$S_j(\mathbf{r},\omega)$ $(j=1,2)$ of the two interfering fields [27]:

$$\begin{aligned} S(\mathbf{r},\omega) &= S_1(\mathbf{r},\omega)+S_2(\mathbf{r},\omega)+ \\ &+2\sqrt{S_1(\mathbf{r},\omega)S_2(\mathbf{r},\omega)}\,\mathrm{Re}[\mu(\mathbf{r}_1,\mathbf{r}_2,\omega)\exp(-i\omega\frac{s_1-s_2}{c})], \end{aligned} \tag{12}$$

where s_1 and s_2 are the optical paths and $\mu(\mathbf{r}_1,\mathbf{r}_2,\omega)$ is the spectral degree of coherence of the light at the two sources defined as

$$\mu(r_1,r_2,\omega)=\frac{W(r_1,r_2,\omega)}{\sqrt{S_1(r_1,\omega)}\sqrt{S_2(r_2,\omega)}}. \tag{13}$$

The cross-spectral density $W(r_1,r_2,\omega)$, defined as the ensemble average of the auto-correlation of the Fourier transforms of the fluctuating fields at points r_1 and r_2, $<\widetilde{V_1^*}(r_1,\omega)\widetilde{V_2}(r_2,\omega')>=W(r_1,r_2,\omega)\delta(\omega-\omega')$, is a measure of the correlations between the spectral components of frequency ν of the light vibrations at r_1 and r_2. Generally, the modulus of the spectral degree of coherence satisfies the inequality $0\leq|\mu(r_1,r_2,\omega)|\leq 1$, where the limits 0 and 1 correspond to the complete spatial coherence and incoherence, respectively.

To account for the interference effects described above in the MCS, each photon is sent into the medium, from a position $\mathbf{r}_m$, with an initial phase ϕ_{r_m} and an initial weight w_{0m}, associated with the spectral intensity profile $S(\mathbf{r},\omega)$ of the incident beam. As the photon propagates inside the scattering medium, its weight can decrease to w_m due to cumulative absorption effects along its path. Once the photon exits the scattering medium, it's position, weight, and optical pathlength are recorded. To describe the random interference, i.e. the intensity fluctuations, we consider that all the N photons that exit the scattering medium at a given position will "interfere" according to a law similar to Eq.(12):

$$S(\omega) = \sum_{m,n}^{N} w_m w_n \left|\mu_{r_m,r_n}(\omega)\right| \cos[\Phi_{r_m,r_n}(\omega) - i\omega \frac{s_m - s_n}{c}] \tag{14}$$

where $m, n = 1, 2....N$. Here, $\left|\mu_{r_m,r_n}\right|$ and $\Phi_{r_m,r_n}$are the modulus and the phase of the spectral degree of coherence of the light source at the pair of source points $\mathbf{r}_m$ and $\mathbf{r}_n$ from which the photons originated. The trajectory length and the weight of each photon of frequency ω are s_m and w_m, while the accumulated geometrical phase is given by $\frac{2\pi}{\lambda} s_m$.

3.1.2 Simulations of the statistical properties of speckles

To avoid averaging out the effects of random interference, the detection area (collection bin) needs to be smaller than the wavelength. However, the statistical nature of the MCS requires the bin to be large enough in order to contain a statistically significant number of photons.

As mentioned previously, we are interested in simulating the propagation of a partially coherent beam through a scattering medium and, in particular, in studying the influence of the spatial coherence properties of the beam on the interaction with the medium. To recover that, MCS should be repeated for each of the insertion points $\mathbf{r}_i$ chosen to describe the initial input beam, and this is computationally inefficient. However, in the case of a dense scattering medium with no transversal limitations and transversal invariance of the optical properties, the distribution of pathlengths between two pairs of points separated by the same distance is statistically similar. Accordingly, the probability distributions of paths corresponding to two injection points differ only by a deterministic distance Δ

of the order of ϖ^2/L, with ϖ being the spread of the input beam and L the thickness of the medium. In the limit where $\Delta < l_s$, and $\varpi << L$, an initial phase added to the photon will account for the small differences in paths in between the two injection points and the detector. Thus, a single Monte Carlo simulation with appropriate input photon parameters can be used. Explicitly, the algorithm that we propose is described as follows. We first simulate the light propagation inside a scattering medium using common codes for incoherent light transport, for an injection point $\mathbf{r}_0 = (0, 0, 0)$ and record the positions ρ_m, weights w_m, and trajectory lengths s_m of all transmitted photons. Next, we separate the photons in bins, assign each photon an initial position r_i, sampled randomly from a flat distribution $[0, \varpi]$, with $\varpi << L$ and adjust the output weight of the photon according to the intensity profile of the input beam (Figure 3.2). Finally, we calculate the contribution of each pair of incoming photons m, n to the final spectral density according to Eq.14. This final step requires defining the modulus and phase of the spectral degree of coherence for each pair of injection points $(\mathbf{r}_m, \mathbf{r}_n)$.

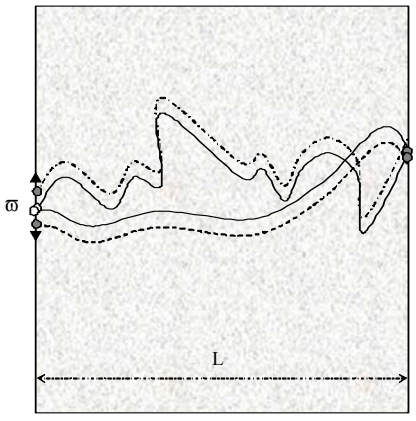

Fig. 3.2 The paths generated through an MCS with light source at $r = (0, 0, 0)$ can be considered as statistically similar to an MCS with an extended source of diameter ϖ, in the condition $\Delta < l_s$ (Δ =deterministic distance of the order ϖ^2/L), and $\varpi << L$.

Following the procedure outlined above, intensity distributions were obtained at the exit surface of the scattering medium for beams of different spatial coherence, and for different properties of the scattering medium.(see Figure 3.3) A Gaussian Schell-model beam [27], was used to describe the intensity

$$I(r,\omega,z) = \frac{A^2}{\left[\Delta\left(z\right)\right]^2} \exp\left[-\frac{r^2}{2\sigma_I^2\left[\Delta\left(z\right)\right]^2}\right] \tag{15}$$

and the spectral degree of coherence of the beam at the input face of the scattering medium

$$\mu(r_1,r_2,\omega,z) = \exp\left(-\frac{\left(r_2-r_1\right)^2}{2\sigma_g^2\left[\Delta\left(z\right)\right]^2}\right) \exp\left(\frac{i\left(r_2^2-r_1^2\right)}{2cR(z)}\omega\right) \tag{16}$$

where A, σ_I and σ_g are positive quantities, $\Delta\left(z\right) = \Delta\left(z\right)\left(z,\sigma_I,\sigma_g,\lambda\right)$ is the expansion coefficient of the intensity width ($\Delta\left(z\right) = 1$ for $z = 0$) and $R(z) = R(z,\sigma_I,\sigma_g,\omega)$ the radius of curvature of the beam. For simplicity we considered that the beam enters the scattering medium at $z = 0$. The degree of global coherence $q = \frac{\sigma_g}{\sigma_I}$ (with σ_g and σ_I representing the effective width of the spectral degree of coherence and of the spectral density, respectively) was used as a measure of the spatial coherence of the input beam, with $q << 1$ corresponding to a spatially incoherent beam and $q >> 1$ to a spatially coherent beam.

To prove the effectiveness of the proposed procedure, we calculated the speckle size of the interference image as a function of the bin size. As shown in Figure 3.4, the speckle size is independent on the bin size as long as the bin size is smaller than $\lambda/2$ proving that coherent phenomena can be correctly investigated with the MCS approach, in spite of the

inherent statistical nature of the procedure. The increase in speckle size for large bins is due to spatial averaging.

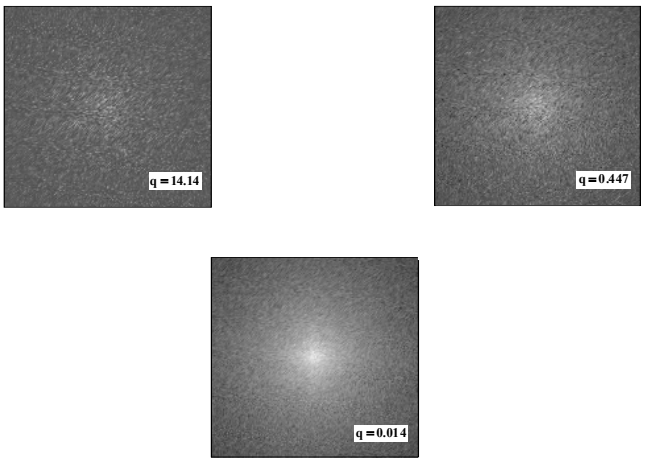

Fig. 3.3. Typical speckles at the exit surface of the scattering medium, when illuminated with beams with coherence properties described by the global degree of coherence q, as indicated.

Characterization of intensity fluctuations is usually done in terms of first and second order statistics. However, for smaller OD's and in the given MCS geometry, the intensity also has a radial distribution, hence the statistical properties are non-stationary. This radial distribution of intensity varies with both the OD and the anisotropy of the scatterers. To remove the non-stationarity, we divided the two dimensional intensity distribution at the exit surface of the scattering medium by the two dimensional intensity distribution obtained for a spatially incoherent input beam which produces no intensity fluctuations and calculated both the probability density function of the intensity $p(I)$ and the contrast $C = \frac{\sigma_I}{<I>}$ (with σ_I being the standard deviation and $< I >$ the mean intensity) for the final image. The optical density for the scattering medium was $OD = 3$, the anisotropies

considered were 0.1, 0.3 and 0.5, while the incident beam had a wavelength of $\lambda = 6 \cdot 10^{-3} l_s$ (l_s - scattering length).

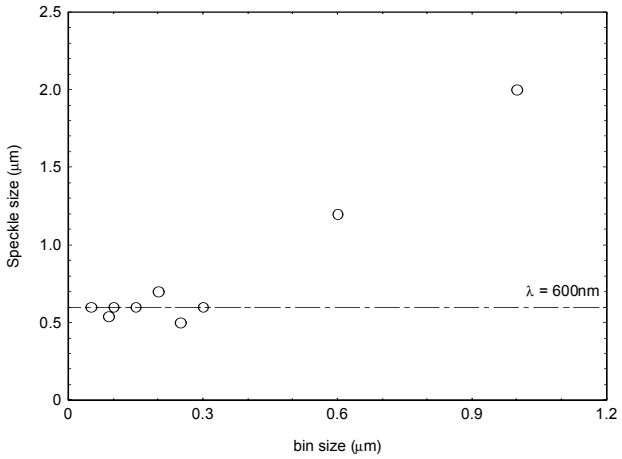

Fig.3.4 Intensity correlation length - speckle size - as function of the bin size (the unit cell in which the photons are added coherently).

The probability density function of the intensity is presented in Figure 3.5 for different degrees of global coherence of the beam illuminating the scattering medium with anisotropy $g = 0.1$ and all the other parameters described before. As the global degree of coherence decreases, $p(I)$ changes from an almost negative exponential decay for $q >> 1$ to a gamma distribution for $q << 1$. This is in agreement with the theory of the speckle patterns statistics [28], which shows that for perfectly coherent, fully developed speckles the statistics of the intensity obeys negative exponential statistics. The partially coherent case is equivalent with the summation of speckle patterns, where $p(I)$ is given by a gamma function, as was proved both theoretically [28] and experimentally [29]. The contrast of the intensity fluctuations increases as the global degree of coherence is increasing, and becomes very close to one for a spatially coherent beam, as seen in Figure 3.6.

As expected, the statistical properties of the intensity fluctuations are not influenced by the scatterer anisotropy, as long as the scattering introduces path difference greater than one wavelength (Figure 3.6). Accordingly, the radial intensity distribution can be related to the size of the scatterer and the OD, while the statistics of the intensity fluctuations is determined primarily by the spatial coherence properties of the input beam.

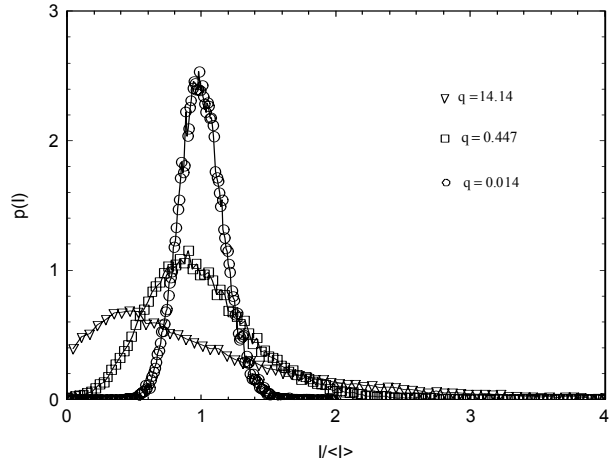

Fig.3.5 Output intensity probability distribution, for different degrees of coherence of the input beam, for a scattering medium with $g = 0.1$ and $OD = 3$.

In conclusion, we studied the statistics of the intensity fluctuations obtained in initially partially coherent beams after the propagation through a scattering medium. We have demonstrated that, treating the wave phenomena statistically, a MCS technique reproduces correctly the expected results fort the intensity distribution obtained after propagation through diffusive media. In this case the influence of the scattering medium on the intensity fluctuations statistics is negligible, as long as the scattering introduces path differences greater than the wavelength. The method can be used to provide solutions for propagation and scattering of partially coherent beams in situations that cannot

be described analytically or by approximations, such as low order scattering and sub-diffusive regimes, or in media with strong local inhomogeneities. Once the simulation has been performed for a certain set of optical and geometrical characteristics of the scattering medium, the statistics of the intensity fluctuations at the exit surface can be obtained for any value of the degree of global coherence q. The same simulation can be used to determine the output spectrum $S(\omega)$ if the optical parameters do not change across the input spectrum.

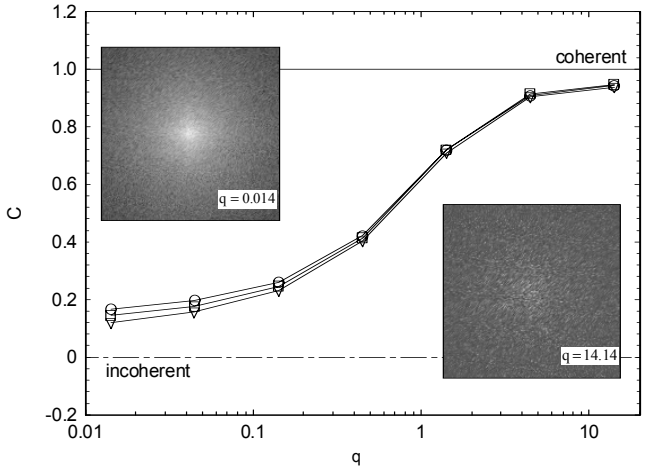

Fig.3.6 Contrast of intensity fluctuations C after propagation of different partially coherent beams through a medium with $OD = 3$ (O) $g = 0.1$, ($\square$) $g = 0.3$ and ($\triangledown$) $g = 0.5$. The insets present the intensity distribution images for beams with q as indicated

3.2 Bandwidth dependence of the heterodyne efficiency in low coherence interferometry

The temporal coherence properties of the radiative source have been used to interferometrically select scattering at different distances from the light source. Low-coherence interferometry, also known as optical coherence tomography (OCT) [30] is an optical

technique that has been extensively improved over the last years, in response to the increasing interest in noninvasive techniques for in-vivo tissue imaging and characterization. Based on the different scattering properties of tissue constituents, this technique acquires a backscattering map of the tissue sample which is inherently related to the tissue morphology and physiology. However, extracting such quantitative information from an image is not straightforward, especially for highly scattering tissues. Not only the multiple scattering and interference effects decrease the image contrast but, as we will see in the following, the detection process is also influencing the outcome. In an attempt to improve the depth resolution of this interferometric technique, the bandwidth of the incident radiation has been increased considerably. In spite of this trend, all of the models introduced to explain OCT images of heterogenous tissue, use a quasi-monochromatic description of the heterodyne detection process [14, 15, 16]. Although this might not be problem for a narrow-band source (for example $30nm$ bandwidth at a central wavelength of $800nm$), one must cautiously describe the process for larger bandwidths.

In this section we address the problems that arise in OCT due to different spectral composition of the reference and the sample beams. Dispersion, absorption, and scattering processes in the tissue are all sources of differences between the spectral compositions of the reference and sample beams. They are generally system specific and, at least for the scattering process, their effect is not obvious. Let us take for instance the process of building an OCT *en-face* image which requires scanning the sample beam across the tissue. In this case, the contrast between different regions is given by the specific scattering properties (reflectance) of each region. However, such regions are usually highly structured

and spatially inhomogeneous and they could lead to different spectral compositions of the scattered beam. In other words, the contrast between different regions will be system specific. To compensate for dispersion effects in optical fibers and refractive optics more or less elaborated schemes have been developed and integrated in OCT systems [31]. On the other hand, accounting for dispersion, absorption and scattering induced effects in the sample implies a priori knowledge of the properties of the investigated tissue.

3.2.1 Heterodyne detection efficiency

For the purpose of this study we will limit the discussion to scattering induced-changes in the heterodyne detection efficiency. Following the heterodyne efficiency definition given by Osche [32], and assuming that the responsivity of the detector is uniform across the wavelength range of interest we consider the heterodyne efficiency of a polychromatic interferometric system to be

$$\eta = \frac{\left| \int \sqrt{S_0(\omega) S(\omega)} d\omega \right|^2}{\int S_0(\omega) d\omega \int S(\omega) d\omega}, \tag{17}$$

where $S_0(\omega)$ and $S(\omega)$ are the spectral densities of the reference and sample beam, respectively. Of course, in general, $\eta \leq 1$ and the equality holds only when the sample beam is not spectrally modified, i.e. when $S(\omega) = \alpha S_0(\omega)$. For most practical situations however $S(\omega) = M(\omega) S_0(\omega)$, and $\eta < 1$. The spectral modifier $M(\omega)$ describes the spectral changes in the sample beam and although the instrument dependent dispersion effects can also be included in $M(\omega)$, they are not considered here because they can be easily

accounted for by instrument calibration. We thus consider that $M(\omega)$ describes only the scattering induced changes. In analogy with the mixing theorem, that states that for any mismatch in phase and amplitude between the local oscillator and the signal beam, the detected signal will be less than optimal, the above definition in Eq.(17) implies that any mismatch between the spectral density of the reference and sample beams will decrease the signal detected in the heterodyne process.

Not long ago, a number of situations have been described where correlated scattering induces spectral changes [33]. To obtain the wavelength dependent spectral modifier for situations pertinent to tissue constituents we will follow the procedure outlined by Dogariu and Wolf [34], that describes the spectrum of the light scattered by a static system of particles at a distance r to be given by

$$S(r\mathbf{u},\omega) = \frac{1}{r^2}\left\langle \left| \widetilde{F}(k(\mathbf{u}-\mathbf{u}_0),\omega) \right|^2 \right\rangle S_0(\omega), \tag{18}$$

where $\widetilde{F}(k(\mathbf{u}-\mathbf{u}_0),\omega)$ is the three dimensional Fourier transform of the scattering potential, and $\mathbf{u}$ and $\mathbf{u}_0$ are the scattering and the illumination directions, respectively. As the OCT systems acquire a backscattering map of the tissue, we only deal in this study with $\mathbf{u} = \mathbf{u}_0$, no other angularly dependent chromatic effects are considered.

3.2.2 Scattering induced spectral changes

To illustrate the influence of the scattering-induced spectral changes on the heterodyne detection efficiency, let us consider systems of identical, spherical particles, illuminated with an incident field whose spectrum is Gaussian, centered at $\lambda = 800nm$ and has a variable bandwidth ($\Delta\lambda = 50 \div 150nm$). As OCT is mainly used for tissue characterization, the properties of the scattering media were chosen to be close to those of typical tissue [35], with average refractive index contrast 1.05 (1.42 - scattering centers; 1.354 - background medium), and sizes from $50nm$ to $25.6\mu m$ (organelles - hundreds of nm size; cell nuclei - μm size). As the concentration of the scattering centers in biological tissue is sometimes very high, correlated scattering was also taken into account, in this case by means of the Percus-Yevick approximation for the structure function $Y(\mathbf{u})$. A measure of the degree of correlation between the fields scattered by individual scattering centers, the structure function is dependent on the relative positions of the scattering centers [36]

$$Y(\mathbf{u}) = \sum_{i,j=1}^{N} \exp(-i\mathbf{u} \cdot (\mathbf{r}_i - \mathbf{r}_j)) \tag{19}$$

where $\mathbf{r}_i$ denotes the position of the i scattering center. After ensemble averaging over the scattering volume V, the structure factor can be calculated as

$$Y(\mathbf{u}) = 1 + < \exp(-i\mathbf{u} \cdot (\mathbf{r}_i - \mathbf{r}_j)) >= 1 + \rho \int G(\mathbf{r}) \exp(-i\mathbf{u} \cdot \mathbf{r}) d\mathbf{r} \tag{20}$$

where $G(\mathbf{r})$ is the pair correlation function, that describes the statistical properties of the spatial arrangement of the scattering centers, and ρ is the scattering centres concentration.

In the case of independent scattering, $Y(\mathbf{u}) = 1$, as there is equal probability of finding the scattering centers anywhere in the volume. For higher concentrations, the pair correlation function $G(\mathbf{r})$ depends on the size and concentration of scattering centers and $Y(\mathbf{u}) \neq 1$. Thus, the structure factor takes into account the effects of collective scattering (see Figure 2.7 and Section 2.3.2 in Chapter 2 for a detailed description of the scattering regimes). In a Percus-Yevick approximation for the structure function, the three dimensional Fourier transform of the scattering potential is

$$\left|\widetilde{F}(k(\mathbf{u}-\mathbf{u}_0),\omega)\right|^2 = |f_1(\mathbf{u},\mathbf{u}_0;\omega)|^2 = \frac{\sigma_t}{4\pi} P_{PY}(\mathbf{u},\mathbf{u}_0;\omega) \tag{21}$$

where $f_1(\mathbf{u},\mathbf{u}_0;\omega)$ is the scattering amplitude (generally complex) of the scattering center in the direction $\mathbf{u}$ when illuminated from $\mathbf{u}_0$, and $p_{PY}(\mathbf{u},\mathbf{u}_0;\omega)$ is the Percus-Yevick modified phase function defined as the product between the single scattering phase function and the structure factor $Y(u)$ of the scattering system

$$p_{PY}(\mathbf{u},\mathbf{u}_0;\omega) = p(\mathbf{u},\mathbf{u}_0;\omega)Y(u). \tag{22}$$

For exemplification, Figure 3.7 presents typical structure functions for systems of identical hard spheres of various concentrations, calculated in Percus-Yevick approximation.

Thus, the scattering-induced spectral changes for various volume fractions of $200nm$ radius scatterers are presented in Figures 3.8. It is clearly seen that the spectrum of the incoming radiation $S_0(\omega)$ is dramatically modified due to scattering; it changes from a Gaussian shape to a two-lobed distribution. Moreover, note that the collective scattering effects influence the shape of the scattered spectrum as well. As can be seen, the spectral

density for 5% volume fraction is quite different than the one corresponding to 45% volume fraction.

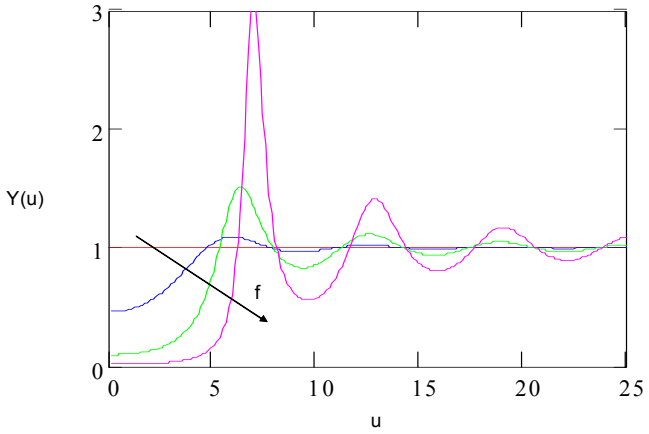

Fig.3.7 Typical structure functions $Y(u)$ as a function of the scattering vector u for increasing volume fractions f of the scattering centers. $Y(u) = 1$ corresponds to the independent scattering regime.

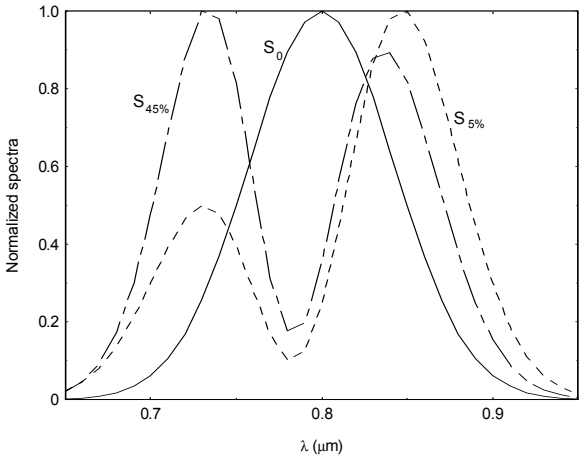

Fig.3.8 Spectrum of the scattered light for monodisperse systems of scatterers with radius of $200nm$ and two different volume fractions of 5% and 45% as indicated. For comparison, the spectrum of the incident light S_0 is also included ($\Delta\lambda = 100nm$).

As a consequence of the concentration dependent spectra of the scattered light, the heterodyne detection efficiency changes also with the concentration as shown in Figure 3.9. Note that the efficiency η decreases with more than 10% as the spectral width of the incoming radiation increases, indicating that precautions must be taken when increasing the spectral width of the source. Calculating the efficiency η as a function of the volume fraction $f(\%)$ for different scattering systems, we have also determined that this variation is influenced by the size of the scattering centers and the refractive index contrast.

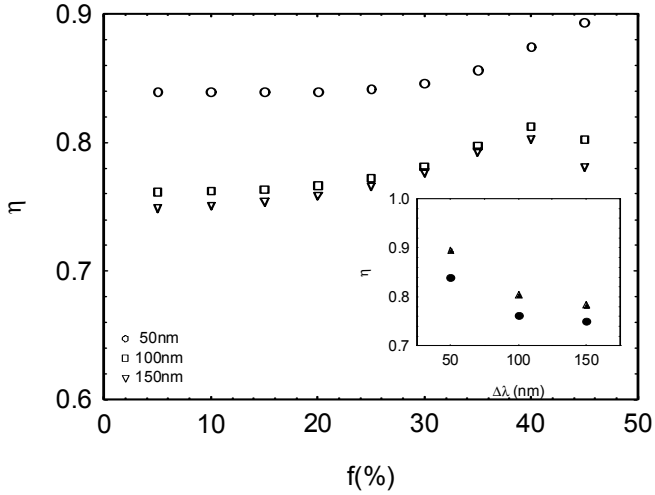

Fig. 3.9 Heterodyne detection efficiency evaluated from Eq.(17) as a function of the volume fraction of the scattering centers ($200nm$ radius; 1.05 refractive index contrast). The three curves represent the detection efficiency for different spectral widths $\Delta\lambda$ of the incident beam as indicated. The inset presents the heterodyne detection efficiency versus the spectral width of the incident radiation, for two different concentrations of scatterers 45% (triangles) and 5% (circles).

To illustrate the effects of the scattering-induced spectral changes on the contrast detected between regions with different scattering properties we considered two different OCT imaging scenarios: (a) a system of identical scatterers with the volume fraction

varying across the detected plane and (b) different systems of scatterers. As an OCT image is built by scanning the sample beam onto the tissue, transversal, pixel by pixel, this contrast is a measure of the image quality. Not only the contrast needs to be high in order to discern between different tissue constituents, but its value should also be representative of the difference in the scattering properties when a quantitative analysis is desired. In a direct backscattering measurement, the optical contrast between two regions with different scattering properties is determined by evaluating the differences in the backscattering cross-section per unit area of the region (considered to be a slab of thickness equal to the coherence length l_c of the incident radiation)

$$C_{bks} = \left| \frac{R_{b1} - R_{b2}}{R_{b1} + R_{b2}} \right|, \tag{23}$$

where

$$R_b = \frac{\sigma_b}{2\sigma_t}[1 - \exp(-2\rho\sigma_t l_c)] \tag{24}$$

and σ_b and σ_t are the backscattering and the extinction cross sections, respectively. The scattering cross-sections are integrated over the entire wavelength range and the density of scatterers is denoted by ρ. Similar to Eq. (23), the contrast for the heterodyne detection process can be calculated as

$$C_{het} = \left| \frac{R_{het1} - R_{het2}}{R_{het1} + R_{het2}} \right| \tag{25}$$

where R_{het} represents the heterodyne signal detected with the corresponding efficiency as defined in Eq.(17).

The image contrasts obtained by either heterodyne detection C_{het} or by a direct backscattering measurement C_{bks}, are presented in Figures 3.10 and 3.11 for the two sensing scenarios described above. The sizes and refractive index contrast used have been chosen to be representative for tissue constituents (organelles - hundreds of nm size; cell nuclei - μm size). The scattering coefficients for these systems are $\mu_s = 5 \div 40 mm^{-1}$ for $200nm$ size of the scattering centers, and $\mu_s = 40 \div 400 mm^{-1}$ for $2.5\mu m$ size of the scattering centers, values similar to those measured in human tissue [35, 16].

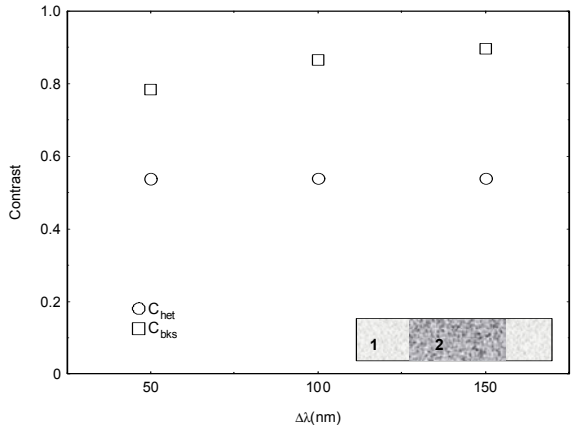

Fig.3.10 Image contrasts C_{het} and C_{bks} versus the bandwidth of the incident radiation. Regions 1 and 2, as indicated in the inset, have scattering centers of the same size $2.5\mu m$ but different volume fractions: 5% and 45%, respectively. The relative refractive index between the scattering centers and the background is $n_s/n_b = 1.05$.

As shown in Figures 3.10 and 3.11, the contrast determined by the heterodyne detection between regions with different optical properties is quite different in magnitude from the one obtained in a direct backscattering measurement. The heterodyne efficiency is, in general, lower when the bandwidth increases, indicating that the sharpness of an

image is actually reduced. Moreover, one can see that the contrast variation with the bandwidth is different for the two methods of detection, hence this effect needs to be carefully accounted for in a quantitative assessment of the heterodyne image.

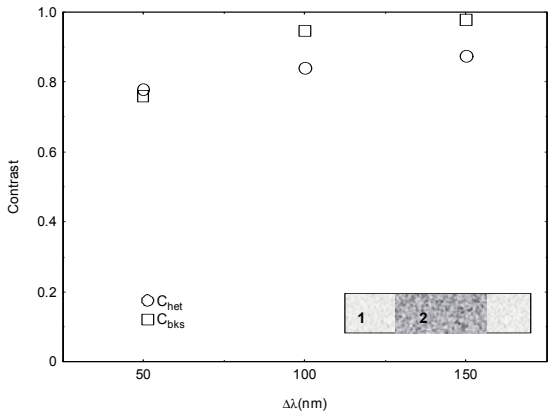

Fig.3.11 Image contrasts C_{het} and C_{bks} versus the bandwidth of the incident radiation. Regions 1 and 2 have same volume fractions of the scattering centers (5%) but different sizes: $0.2\mu m$ and $2.5\mu m$, respectively. The relative refractive index between the scattering centers and the background is $n_s/n_b = 1.05$.

The present treatment did not include any depth degradation effects due to the multiple scattering processes and loss of spatial coherence of the sample beam, as described by Levitz et al. [16]. However, these effects could be included in a generalization of this formalism in the space frequency domain.

Our results demonstrate that, although neglected in current formalisms, the spectral changes induced by scattering alone will in general decrease the detection efficiency in a heterodyne detection process. The effect is stronger when the bandwidth of the incoming radiation is increased and it is dependent on the specific scattering system. The bandwidth

dependence needs to be carefully considered when OCT techniques are to be used as a quantitative tool for characterizing inhomogeneous media.

3.3 Discussion on chapter 3

The influence of the spatial and temporal coherence properties of the radiative source on the outcome of a scattering experiment have been presented in this chapter.

We have seen that, using Monte Carlo simulations, one can study the characteristics of beams with adjustable spatial coherence properties that propagate through highly scattering media. Moreover, it was demonstrated that a single simulation is sufficient to obtain the intensity distribution at the exit surface of the scattering medium for any degree of global coherence of the input beam. The efficient numerical procedure correctly reproduces the first and second order statistics of the intensity distribution obtained after propagation through diffusive media. Most importantly, this new technique has the advantage of providing solutions for problems not covered by analytical descriptions and approximations.

Most sensitive scattering investigations are performed interferometrically, the reflection of the sample being enhanced by heterodyne detection. The effect of radiation bandwidth on the heterodyne detection process was also discussed. Although neglected in current formalisms, the spectral changes induced by the scattering process are decreasing the heterodyne detection efficiency. This effect depends on the bandwidth of the radiation used and we found that the spectral induced spectral changes decrease the contrast

obtained in a low coherence interferometric imaging system between regions with different optical properties. Hence a quantitative analysis of the images obtained by optical coherence tomography needs to be carefully considered.

The results of this chapter represent the basis of a quantitative approach to solve the inverse problem associated with scattering from biological media.

As described in Chapter 2, the information obtained through a light scattering experiment is influenced not only by the source and the detection process, but also by the structural characteristics and geometry of the sample. Consequently, in the next chapters we will examine both interface and multilayer effects and describe novel approaches that we developed to characterize such inhomogeneous media.

CHAPTER 4

INFLUENCE OF INTERFACE AND ABSORPTION

The analytical description of the light transport in the bulk of a highly scattering medium has been introduced in Chapter 2, section 2.1.2. In the so-called P1 approximation, the diffusion equation of light transport is introduced. To solve the diffusion equation, one must apply appropriate boundary conditions and impose limits on the absorption levels ($\mu_a << \mu_s(1-g)$), as described in detail in Section 2.1.2. Consequently, in practical applications, subtle boundary and absorption effects should be considered carefully. However, one needs to find an appropriate tool to study these effects. The pathlength distribution of light $P(s)$ inside inhomogeneous media is influenced by the scattering and absorption inside the scattering medium, and the boundary conditions as well. We show in the following that looking at changes in $P(s)$ one can obtain information on subtle effects introduced by the last scattering event on the scattering from diffusive media, when there is refractive index contrast at the boundaries. Moreover, we study the effects of absorption on $P(s)$, by taking advantage of the unique capability of optical pathlength spectroscopy to recover $P(s)$ experimentally, even for sub-diffusive regimes. We also asses the influence of the absorption distribution inside the sample, because the situation where the absorbing centers are also the scatterers has been barely studied previously, and introduce a model to describe the influence of the rough bound-

aries of an otherwise diffusive media on the spectral diffuse reflectance. The implications are discussed in the context of several applications.

4.1 Refractive index mismatch at the surface - a Monte Carlo study

Solving the diffusion equation for bounded media requires special conditions, such that the behavior of the energy density at the interfaces is taken into account. Due to the refractive index contrast at the boundaries, light is often reinjected (by total internal reflection) into the medium and forced to travel a new diffusive path. Accordingly, the diffusion process is modified and the introduction of a new scale length that characterizes the specific medium interface is necessary. This new scale length (Figure 4.1), called the "extrapolation length" (z_e), measures the distance outside the medium where the energy density vanishes linearly. Accurate value of this length is needed to interpret any experiment based on diffusion of light.

Although it is accepted that the extrapolation length depends on the refractive index mismatch at the boundary, no dependence on the anisotropy g of the particle has been considered. However, recent experimental [17], theoretical [18], [37] and numerical [19] results has led us to believe that the influence of the scattering anisotropy on the extrapolation length needs to be carefully examined. Both experimental and theoretical studies of this influence have been conducted. [6]. To complement these approaches and to get more insight into possible $z_e(g)$ effects, a comprehensive numerical experiment was performed, i.e. a Monte Carlo simulation of photon transport inside a semi-infinite

medium (see details of probability distribution functions in Section.2.2.2). The optical properties of the medium: l_a- mean absorption length, l_s- mean free path, g, n_i- index of refraction inside the medium, n_o-index of refraction outside the medium, were all variable. For this particular experiment, l_a was chosen to be 100 times larger than l_t such that the absorption can be considered negligible. Multiple data files containing the properties of the photons returning into the semi-space $z < 0$ were recorded and then used to get the pathlength-resolved reflectivity.

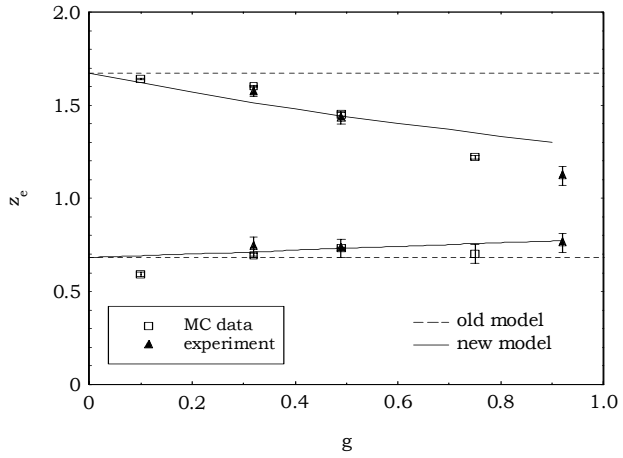

Fig. 4.1. Values of the extrapolation coefficient as obtained with the Monte Carlo simulation, compared with both experimental results and theoretical models.

As described in Section 2.2.2, a large number of detected photons is required to reduce the statistical variance. This means that the time necessary for collection over a small area becomes prohibitively long. However, similar information on z_e can be obtained by integrating the reflected photons over the entire area of the sample and using the expression derived for the path-length resolved integrated reflectance to fit our data [38]:

$$R(s) = Bl_t^{1/2} z_e s^{-3/2} \exp(-\frac{3z_e^2 l_t}{4s}), \tag{26}$$

where B is a constant that depends on the source strength and the light speed inside the medium.

Simulations have been performed for $g = 0.1, 0.32, 0.49$ and 0.75 and a decrease in the extrapolation length is obtained as the anisotropy factor g increases (see data in Figure 4.1). The results are consistent with previous Monte Carlo calculations [19] and are also in agreement with the experimental data obtained by Popescu [6].

MCS are thus a viable approach in providing solutions for the light transport in inhomogeneous media. This is especially true for scattering systems that cannot be described analytically, and where the approximations that have been introduced to simplify the solutions of light transport cannot be applied, such as for example, inhomogeneous media that are in a subdiffusive regime, have roughness at the surface and/or regions with different optical properties. Several other applications of the MCS in the context of absorbing, porous and multilayered media are introduced below in Sections 4.3, 5.1.1 , and 5.2.1 respectively. We continue in the next section with the description of another change induced by the *"last scattering event"*, in the case of rough surfaces.

4.2 Spectral changes in reflectance induced by the last scattering event

In some conditions, the integrated reflectance spectrum of a highly scattering sample can be modeled using the time dependent diffusion equation. As described in Section 2.1.2

the diffusion approximation assumes an isotropic light source, small absorption, elastic scattering, and neglects all polarization and interference effects. Light propagation inside the medium is characterized by the linear scattering coefficient μ_s, the linear absorption coefficient μ_a and the scattering anisotropy g. In the case of a monodisperse system of scattering centers these optical properties can be calculated based on the Mie formalism for scattering from spherical particles. Consequently, the reflectance spectra $R(\lambda)$, in the diffusion approximation, can be calculated as [1]

$$R(\lambda) = \frac{3Q(1+Q+gQ)(\frac{Q}{3(1-g+Q)})^{-1/2}+3[(1+Q)^2+g(-1+Q+Q^2)]}{(-1+g-Q)(3+2\sqrt{3}(\frac{Q}{1-g+Q})^{1/2})} \tag{27}$$

where $Q(\lambda) = \frac{\mu_a(\lambda)}{\mu_s(\lambda)}$, and the anisotropy is also wavelength dependent.

According to Eq.27, depending on the size of the scattering centers d and the absorption coefficient, the shape of $R(\lambda)$ changes from decreasing with the wavelength for $d << \lambda$, to being independent of the wavelength for $d \simeq \lambda$ and finally increasing with the wavelength for $d >> \lambda$. The slope of $R(\lambda)$ is, however, very small, and it can be increased only by increasing the absorption in the limits of the diffusion approximation. One example is illustrated in the following.

It has been observed experimentally that the surface of natural marble that has been cleaned with a specific laser radiation (Q-switched Nd:YAG with $\lambda = 1064nm$) exhibits a reflectance spectra (acquired either with an integrating sphere - $R_{IS}(\lambda)$, or by hyperspectral imaging - $R_{HI}(\lambda)$) that increases with the wavelength over the visible range. In other words. there is a yellowing effect that cannot be explained due to chemical changes. In the following we show that, despite strong diffusion and very low absorption, spectral

changes can be induced due to the last scattering event in the sample. For this purpose we analyzed two marble samples, one clean and the other cleaned as described above.

A marble sample, due to its intrinsic inhomogeneity, strongly scatters light. Visual inspection shows a white appearance of the clean marble, thus, one can assume that, over the visible range, the absorption is constant and small. In this respect, the marble can be considered, in a first approximation, as a diffuse medium. To describe its scattering properties, one can consider that the scattering centers are particle-like (spheres). For a better description, a size distribution of the scattering centers has to be considered as well, and the effective properties of the distribution (g, μ_s, μ_a) have to be calculated for each wavelength.

However, using Eq.27 to recover, in a diffusion based model, the slope and shape of $R_{HI}(\lambda)$, we observed that, even for a clean marble sample, we need to increase the absorption such that $\frac{\mu_a}{\mu_s} = 0.36$. This certainly exceeds the validity limits $\mu_a << \mu_s^{'}$ of the diffusion approximation, as introduced in Section 2.1.2. It becomes obvious that this approach by itself fails to properly account for the shape of the measured reflectance $R_{HI}(\lambda)$. There are two main aspects that are not considered in the diffusion model and which will prove to be really important in the modeling process.

First aspect is the measuring geometry. Eq.27 describes the diffuse reflectance $R_{IS}(\lambda)$, as it would be obtained by using an integrating sphere. $R_{HI}(\lambda)$, on the other hand is measured with a hyper-spectral camera, placed normal to the sample at $50cm$ distance. Thus $R_{HI}(\lambda)$ represents the reflectance of the sample in the backward direction, over a solid angle determined by the numerical aperture of the setup. Accordingly, knowledge on the

angular distribution of the marble reflectance is critical. To verify the importance of the measuring geometry, we measured the diffuse reflectance $R_{IS}(\lambda)$ of the marble with an integrating sphere. Indeed, as is presented in Figure 4.2, the integrated reflectance of both clean and cleaned marble exhibited a much smoother dependence on the wavelength Moreover, when $R_{IS}(\lambda)$ for the clean and cleaned marble samples in Figure 4.2 are compared, it is observed that the spectrum of the clean marble the spectrum is almost flat, while for cleaned marble sample the absorption effects are important. Visual inspection of the cleaned marble shows the presence of a thin layer on top of the diffusive bulk. This layer is probably created at the interaction of laser radiation with the encrustation particles. The combined absorption of the diffusive bulk and the top layer gives the deviation from the flat reflection spectra expected for a totally diffusive media.

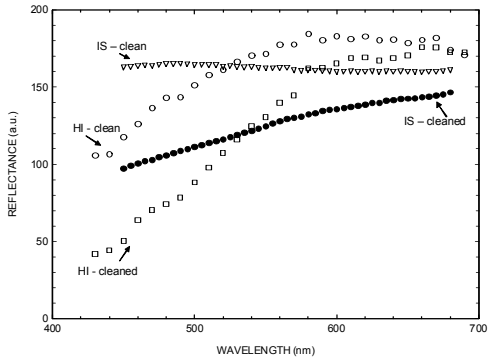

Fig. 4.2 Comparison between $R_{HI}(\lambda)$ and $R_{IS}(\lambda)$ for both marble samples (HI - hyper-spectral imaging; IS - integrating sphere). Note that the units for the reflectance are arbitrary. The integrating sphere measurements were scaled to be in the same magnitude range as the hyper-spectral imaging measurements.

The second aspect not considered in the derivation of Eq. 27 is the roughness at the surface of the marble samples. As described in Sections 2.1.2 and 4.1, the diffu-

sion approximation is based on very specific boundary conditions, i.e. smooth interfaces with possible refractive index contrast. However, the marble surface is rough, and this roughness could change the angular distribution of the reflectance considerably. In other words, although light transport is diffusive in the bulk, the angular distribution of the reflectance is influenced by the last scattering event, a process that depends on the scattering anisotropy of these last scattering centers, as shown in Section 4.1. One way to account for this effect is by introducing an imaginary boundary that separates the sample into two parts, a completely diffusive bulk and a thin layer of scattering centers on top of that. The angular distribution for the waves originating from the diffusive bulk ($\mu_a << \mu_s$) is given in the frame of the diffusion approximation by [39]

$$T(\theta) = \frac{1}{2\pi} \frac{z_e \cos(\theta) + \cos^2(\theta)}{\frac{z_e}{2} + \frac{1}{3}}, \tag{28}$$

where z_e is the extrapolation length ratio and takes the value 2/3 since the bulk and the skin layer have the same refractive index. Each scattering center in the skin layer has a probability of scattering light that depends on the effective anisotropy g and the angle between the incident and scattering direction. The Henyey - Greenstein distribution [11], gives a good approximation for this probability:

$$H_g(\alpha) = \frac{1 - g^2}{(1 + g^2 - 2g\cos(\alpha))^{3/2}} \tag{29}$$

Thus, the angular distribution of light scattered by the skin layer when $T(\theta)$ is incident on it becomes

$$F_g(\theta,\varphi) = C\int_0^{2\pi}\int_0^{\pi/2} H_g(\theta,\varphi;\theta',\varphi') T(\theta')\sin(\theta')d\theta' d\varphi' \quad (30)$$

where C is a constant such that $\int_0^{2\pi}\int_0^{\pi/2} F_g(\theta,\varphi)d\theta d\varphi = 1$.

Because g is a function of λ and n (the refractive index), the spectral distribution of light emerging from the sample can be calculated. In the approximation that the scattering center is large compared to the wavelength, the Henyey-Greenstein distribution can be approximated with a step function, such that the probability to have light scattered with an angle θ is 1 if $\theta \in [0, \frac{\lambda}{d}]$ and is 0 otherwise. In these conditions, the spectral distribution of light emerging from the sample in the direction normal to the sample ($\theta = 0$) surface becomes:

$$F(\lambda, d; \theta = 0) = 2\pi\int_0^{\lambda/d} T(\theta')\sin(\theta')d\theta' \quad (31)$$

Using this equation, one can now calculate the reflectance spectra in the backward direction for different sizes d of the scattering centers ($d >> \lambda$). Again, we want to emphasize that these last scattering centers are introduced to model the surface roughness of the sample. Because for the clean marble sample we already know that the absorption is very small, we can use d as an adjustable parameter in our model to recover the experimental dependence of the hyper-spectral imaging measurement (Figure 4.3a; $d = 2\mu m$).

The prevailing mechanism of marble cleaning by the Q-switched Nd:YAG laser with $\lambda = 1064nm$ has been found to be the selective explosive vaporization of the dark par-

ticulates present in the body of the preserved layer [40]. Thus, the surface of the cleaned marble sample is rougher than the clean one, large voids appearing at the surface due to encrustation particles explosion during laser irradiation. The average behavior of the reflectance is well described by our model. However, as can be seen in Figure 4.3b, by simply increasing d to $5\mu m$ one cannot recover the detailed features of $R_{HI}(\lambda)$ for the cleaned marble. This is to be expected since we have shown in Fig.4.2 that the cleaned marble also selectively absorbs light.

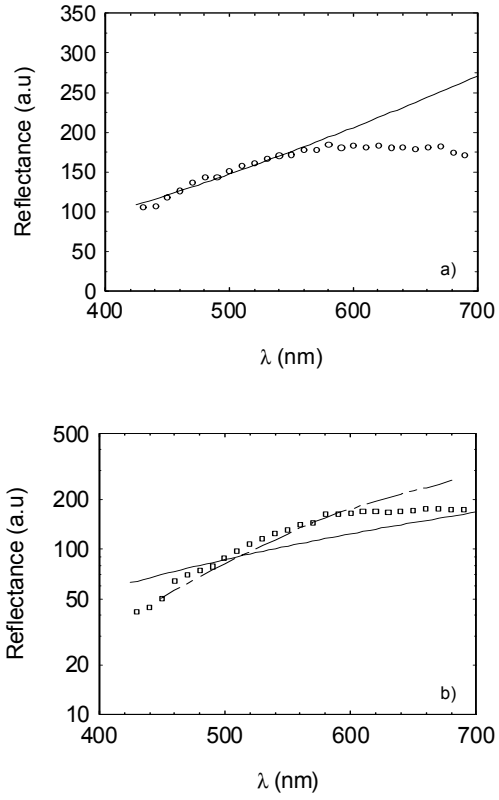

Fig. 4.3 Comparison between $R_{HI}(\lambda)$ (points) and the proposed model (lines) for (a) clean marble sample ($d = 2\mu m$) and (b) cleaned marble sample ($d = 5\mu m$). The dashed line in b represents the results obtained after considering absorption effects, as described in text.

Thus, our model predicts a monotonic increase of the flux with the wavelength by taking into account roughness at the surface (modeled as a single scattering layer), and without considering any absorption effects. This is a remarkable result because, in most previous descriptions, it was customary to attribute all the spectral changes to absorption or, in the case of single scattering situations, to Mie type form factors. Here, we demonstrated that despite strong diffusion, wavelength dependence is generated through a mechanism other than absorption.

Although we have recovered the general trend of the reflectance spectra, as measured using hyper-spectral imaging, one still needs to refine the model in order to completely recover the shape of $R_{HI}(\lambda)$. One way to do so is by including the wavelength dependent absorption. In a first approximation, for the clean marble, the absorption dependence on the wavelength is determined through the integrating sphere measurements. Multiplying the measured $R_{IS}(\lambda)$ with the result of the proposed model, we obtain a slightly flatter shape of the spectra at higher wavelengths. For the cleaned marble, on the other hand, we have to deal with a more complex situation. The integrated reflectance measurements show selective wavelength absorption due to the thin layer of absorbent material that one visually observes on top of the marble. In the assumption that the bulk reflectance has no wavelength dependence, the integrated reflectance measurement actually represents the transmission of the thin absorbent layer. Now, the light has to get to the diffusive bulk and back through the thin absorbent layer. Consequently, in order to make absorption corrections to the model we need to multiply the theoretical curve for the reflectance with

the squared transmission of the layer. The results are presented in Figure 4.3b - dashed curve.

A much better agreement is observed for the $400 - 600nm$ range, but the reflectance is still overestimated for larger wavelengths. This simple way of introducing absorption, as a multiplicative factor, is obviously not able to remove all the discrepancies between the model and measurement. A better way to go would be to introduce the absorption effects in the *"diffusion-last scattering event"* model, from the beginning. However, this would require finding the absorption dependence of the angular distribution coming from the bulk. This is not possible anymore in a diffusion approximation and the much more complex transport theory has to be applied.

4.3 Simultaneous determination of scattering and absorption coefficients

The first sections of this chapter presented the interface effects on the diffusion approximation of light transport inside the medium. However, it was clear at the end of the last section, that, for a complete description of the wavelength resolved reflectance, one needs to also have knowledge of the absorption in the bulk of the sample. In the limits that the diffusion approximation is valid, i.e. the condition $\mu_a << \mu_s(1-g)$ is satisfied, the absorption coefficient of a scattering sample can be determined [41, 42, 43, 44]. Most previous techniques, however, used either sophisticated time of flight configurations or measurements of the diffuse reflectance and mean arrival time from a medium at different source-detector separation, or different modulation frequencies of the light source. In this

section we asses the capability of simultaneous determination of scattering and absorption coefficients, with a single measurement of the pathlength distribution of light inside the sample, determined with OPS. Moreover, we study the influence of the absorption distribution inside the sample, as the case where the absorbing centers are also the scatterers has been barely studied previously.

OPS, as described in detail in Section 2.2.1, is a technique that is able to recover experimentally the pathlength distribution of light $P(s)$ inside a scattering media. In the particular OPS geometry (pencil beam incident on the sample, source and detector overlapped), and using the diffusion approximation of light transport within the medium, the pathlength dependence of the energy flux detected can be evaluated to be [5, 38]

$$J(s) = A z_e l_t^{-3/2} s^{-5/2} \exp(-\frac{z_e^2 l_t^2}{4Ds}) \exp(-\mu_a s) \tag{32}$$

where D is the diffusion coefficient, A is a constant dependent on the source strength and s is the pathlength traveled through the medium. It is apparent from Eq. 32 that the scattering coefficient influences the distribution at small (although large enough for the diffusion approximation to be valid) pathlengths s, while the absorption coefficient is influencing the distribution mostly at long pathlengths s.

The pathlength resolved reflectance $R(s)$ was determined in silica microspheres ($a = 0.5\mu m$, $n = 1.46$) suspensions in water, in a 20% volume fraction. The absorption was modified by adding IR absorbing dye to the solutions. The absorption coefficient of the IR absorbing dye (IR absorbing powder and acetone) was determined using the Cary spectrophotometer. As presented in Fig.4.4, as the absorption increases the overall re-

flected power decreases while the slope at long pathlengths s increases, as longer paths are cut-off due to absorption effects. According to Eq.32, the deviation of the slope from a $s^{-5/2}$ dependence gives direct information on the absorption coefficient of the liquid.

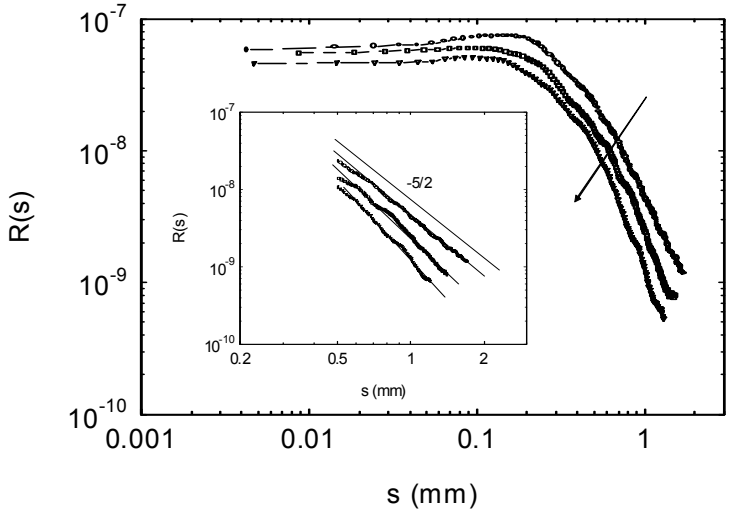

Fig. 4.4 Pathlength resolved reflectance $R(s)$ in 20%, 0.5μm Si microspheres suspensions in a mixture of water and IR absorbing dye. The inset shows that as absorption increases, the longer paths are cut-off and increasing deviations from the $s^{-5/2}$behavior are observed.

From the pathlength resolved reflectance $R(s)$, the pathlength distribution of light through the medium can be calculated by a simple normalization procedure. The tail of this distribution is then fitted with Eq. 32 to recover the scattering and absorption coefficients. A very good agreement was obtained when comparing the absorption coefficient determined by OPS measurements with the one determined with a Cary 500 spectrophotometer in transmission through solutions of different dye concentrations in water (Figure 4.5).

To obtain the reduced scattering coefficient as well, one needs to include the exact dependence of the diffusion coefficient D on the absorption dependence. Recently, there

has been a lot of controversy in the literature regarding this dependence. At one end, some authors [45], [46], [47], [48] claim that the diffusion coefficient does indeed depend on absorption, and that it is given by the relation $D = \frac{1}{3(\alpha\mu_a+(1-g)\mu_s)}$, with $\alpha \in [0.2, 0.5]$. On the contrary, some other authors [49], [50], [51], [52] claim that the diffusion coefficient does not depend on absorption, and it is simply given by the relation $D = \frac{1}{3(1-g)\mu_s}$. However, in the present case, the absorption is much smaller than the scattering coefficient, hence it is safe to assume that $D = \frac{1}{3(1-g)\mu_s}$. The values obtained for the reduced scattering coefficient were very close ($\sim$ 100 cm^{-1}; small variations due to small changes in the volume fraction induced by adding the dye) to the one determined using Mie theory.

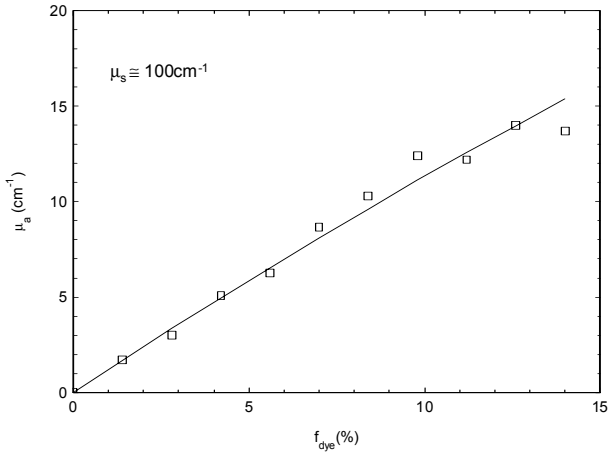

Fig. 4.5 The absorption coefficient μ_a determined by fitting the tail of the pathlength distribution of light inside the medium as determined with OPS (squares) as a function of the dye concentration. The line represents μ_a measured using transmission measurements in water-dye solutions.

In conclusion, OPS allows for the determination of the reduced scattering and absorption coefficients of a sample, as long as the diffusion approximation of light transport can be applied. Given the influence of the absorption on the long paths inside the scattering

medium, the absorption coefficient can be determined independently from the reduced scattering coefficient, just by considering the deviations from a $s^{-5/2}$ dependence at long paths. The reduced scattering coefficient can also be determined very precisely, once the correct form of the diffusion coefficient is determined. Consequently, having access to the pathlength distribution of light inside the medium, and in the limits described in detail above, a simultaneously determination of the scattering and absorption coefficients is possible from a single measurement.

Another important problem that was barely studied experimentally, is to account for absorption when the absorbing center is the scattering particle itself. The importance of such study is to asses the ability of obtaining information on the complex index of refraction of one single particle and to determine if, in certain measuring geometries, one is able to distinguish between absorption at the level of particulates or in the host medium. This is a significant problem for optical diagnostics of biological media.

For the purpose of this study, two Monte Carlo simulations were performed. The scattering and the reflections at the boundaries were taken into account as described in Section 2.2.2. For the absorption mechanism however, two distinct procedures have been considered. For absorption at the level of particulates, the photon loses a part of its weight at each scattering event, such that the final weight w_f of the photon is

$$w_f = w_0 - \sum_i w_{i-1}(1 - \frac{\mu_s}{\mu_s + \mu_a}) \tag{33}$$

where w_0 is the initial weight, and μ_a and μ_s the absorption and scattering coefficients of the inhomogeneous medium. The photon is terminated if its weight becomes smaller than

a predetermined value. Conversely, the absorption in the host medium is simulated by generating an absorption length L_a for each photon. This absorption length is sampled from the probability

$$p(l) = \mu_a \exp(-\mu_a l) \tag{34}$$

and the final final weight w_f of the photon is

$$w_f = w_0(1 - \frac{L}{L_a}) \tag{35}$$

with L being the length of the photon trajectory. The photon is terminated if the length of its trajectory becomes larger than the absorption length.

Figure 4.5 presents the results of these simulation, in terms of the pathlength distribution of light transport inside the inhomogeneous media, and in the geometry of optical pathlength spectroscopy.

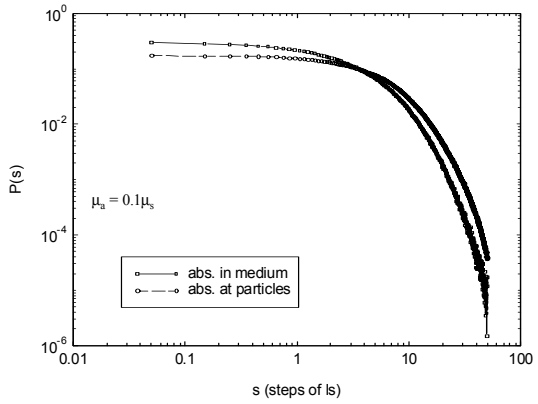

Fig. 4.6 Pathlength distribution of light inside an inhomogeneous media obtained with MCS. Each curve is obtained using a different MCS, as described in the text.

As it can be observed in Figure 4.6 the distributions of paths determined with the two MCS are different, suggesting that there are differences between the absorption in the particulates versus the absorption in host medium..This effect is decreasing when the absorption becomes much smaller than the scattering. The simulations recovered the correct shape of the pathlength distribution of light inside the medium without absorption ($\mu_a = 0$) according to Eq. 32.

Thus, although the scattering and absorption coefficients are the same in the two situations, it is apparent from Figure 4.5 that the pathlength distribution of light is different for the two absorbing scenarios. These results need to be substantiated with experimental studies of the pathlength distributions of light that can be obtained with optical pathlength spectroscopy.

4.4 Discussion on chapter 4

It is important to emphasize that the results presented above have been obtained for highly scattering samples for which the light transport in the bulk can be described as being diffusive. The surface and absorption effects proved to be quite important.

To summarize, we have initially shown, using a Monte Carlo simulation, that the diffusion process close to the boundary is fundamentally different from that in the bulk in the sense that it is affected by the scattering properties of individual centers. The results were compared with other works and are supported by experimental evidence and an independent analytical model. Hence, the extrapolation length z_e, introduced to

describe the diffusion process for bounded media, is not only dependent on the refractive index contrast at the boundary, but depends also on the anisotropy g of the scattering centers. This study has important implications upon any diffusion experiment in bounded media, as the interpretation of the experimental results requires accurate knowledge on the extrapolation length z_e. Monte Carlo simulations, proved, once again, an important tool in description of subtle phenomena, that are not accessible through analytical approaches. For other important results obtained with Monte Carlo simulations, please see also Section 3.1, 5.1.1, and 5.2.1 of these dissertation.

Diffuse reflectance spectroscopy, is a simple experimental procedure that we have used to probe the structure of highly inhomogeneous media. In section 3.2 we showed that, when one takes into account the roughness at the surface, a layered model can be developed where the spectral reflectance increases monotonic with the wavelength. This is a remarkable result because, in most previous descriptions, it was customary to attribute all the spectral changes to absorption or, in the case of single scattering situations, to Mie type form factors. Here, we have demonstrated that despite strong diffusion, wavelength dependence is generated through a mechanism other than absorption.

In the last section, we have demonstrated that, using optical pathlength spectroscopy one can recover simultaneously the scattering and absorption coefficients of an inhomogeneous medium, by recovering the pathlength distribution of the light transport and fitting it with a solution of the diffusion approximation. Moreover, we have suggested with MCS that the absorption distribution inside the sample influences the pathlength distribution of light transport. This effect might be used for discerning in between absorption at the

level of particulates and absorption inside the host medium and determining the complex index of refraction of particulates in the presence of strong scattering.

Having concluded that the interface and absorption effects need to be carefully considered in interpreting a scattering measurement result, we will continue in the next chapter with a presentation of various methods for characterizing inhomogeneous media. This methods have been implemented by considering also the complex size distribution of the scatterers and/or the complex geometry of the sample.

CHAPTER 5

BULK AND MULTILAYER EFFECTS

As the sample structure and geometry become more complicated, the difficulty of solving the inverse problem increases considerably. Consequently, one must consider all of the variables and find the suitable experiments to be used. In this chapter we present the characterization of some highly scattering media, using optical pathlength spectroscopy and diffuse reflectance spectroscopy. We also discuss the different analytical or numerical techniques that need to be used depending on the sample geometry. These scattering techniques are used to characterize porous media such as membrane filters, diffusive coatings and caries lesions in natural teeth enamel.

5.1 Optical reflectance of porous media

Porous media are common in a wide variety of fields such as hydrology, chemical engineering, medicine and biological engineering. Many theoretical models and experimental methods have been developed to characterize their very complicated and irregular structure [53], [54].

Some of the important parameters that characterize the structure of the porous materials, are the porosity (defined as the fraction of the bulk volume of the porous sample that

is occupied by pore space), the average pore size, and the pore size distribution (PSD). Since the pore system consists of interconnected networks (see Figure 5.1), one has to use a specific model to define and describe the pore size. This model is usually related to the method that is used to characterize the medium. For a multiple light scattering technique, the most intuitive and simple model is to consider the voids (pores) as spherical scattering particles. In the following, we assess the possibility and the limits of using such approach for porous media characterization.

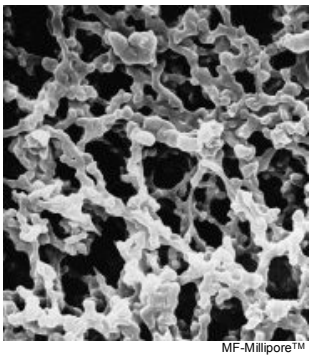

Fig. 5.1 Typical pore structure for a membrane filter

5.1.1 Pathlength resolved reflectance in porous membrane filters

In this section, we are investigating the possibility of using a multiple light scattering technique, i.e. optical pathlength spectroscopy (OPS), to determine the structural characteristics of the porous media. Many light scattering studies targeted porous materials [55], but the multiple scattering component was regarded as "noise". Nevertheless, the recent advances in the understanding of these phenomena imply that multiple scattering could be very useful in investigating the microstructure of random media [1].

As presented in detail in Section 2.2.1, OPS determines experimentally the pathlength resolved reflectance $R(s)$ of an inhomogeneous media. Consequently, it is important to consider the analytical descriptions of $R(s)$, for different characteristics of the sample. In a diffusion approximation, and in the given geometrical configuration source-detector of OPS, the analytical description of the pathlength resolved reflectance is given by [5]

$$R(s) = A l_t^{-3/2} z_e s^{-5/2} \exp(-\frac{3 z_e^2 l_t}{4s}) \tag{36}$$

where all the parameters have been introduced earlier. The transport mean free path l_t, that is essentially the path that the light travels inside the medium until its direction is randomized, is related to the number density ρ of the scattering particles, the scattering cross section σ_s for a single scattering event, and the anisotropy g of the scattering particle through $l_t = \frac{1}{\rho \sigma_s \ (1-g)}$.

Both the scattering cross section and the anisotropy depend on the particle size and the index contrast inside the medium. Accordingly, if the transport mean free path is measured for two different optical contrasts inside the same medium, the scatterer's size can be determined. As the scattering decreases and the transport mean free path becomes comparable with the thickness, the diffusion approximation is not valid anymore. Further improvement can be obtained by considering the medium as a diffusive slab of finite thickness. The pathlength-resolved reflection from a slab of thickness d is given by Eq. 37[38, 56],where B is a constant depending on the source strength. The number of terms that have to be taken in the sum depends on the optical characteristics of the sample and on the fraction d/l_t. When this method fails as well (generally for $l_t > d/3$), a MCS of the

light propagation inside the sample (see Section 2.2.2, for details on the procedure) needs to be performed to recover the pathlength-resolved reflectivity for the given thickness.

OPS was used to recover experimentally the pathlength resolved reflectance of porous membranes. The membranes under investigation were made by Millipore[1], and covered a wide range of materials (mixed cellulose esters, polyvinylidene fluoride and polycarbonate), thicknesses ($10 - 150\mu m$) and pore sizes ($0.4 - 1.2\mu m$). Each sample was placed under the measuring arm of the apparatus and the pathlength resolved backscattering signal was recorded. To decrease the noise introduced by specular reflections, the reflectance signal was averaged over multiple successive scans.

$$\begin{aligned} R(s) &= B \sum_{m=-\infty}^{\infty} [(2md + 4mz_e l_t + l_t) \\ &\quad \exp(-\frac{3}{4}\frac{(2md + 4mz_e l_t + l_t)^2}{l_t s}) \\ &\quad +(2md + (4m-2)z_e l_t - l_t) \\ &\quad \exp(-\frac{3}{4}\frac{(2md + (4m-2)z_e l_t - l_t)^2}{l_t s})] \end{aligned} \tag{37}$$

First, the thickness was measured by placing the membrane on top of a microscope slide on an $X - Y$ translation stage and taking measurements of the reflection from the membrane and from the glass. Since the reflection is pathlength resolved, the distance between the two reflection peaks gives the thickness of the membrane, as in Figure 5.2.

The experimental values obtained for the average thickness are very close to the ones given by the manufacturer (Table 5.1). Thus, a very high precision in measuring the membrane thickness can be achieved by using OPS. The only limitation in measuring the thickness is introduced by the coherence length of the source, as this determines

[1] Millipore, 290 Concord Rd., Billerica MA 01821, U.S.A. Tel: (978) 715-4321

the precision at which two points can still be separated in the optical path domain. This limitation is better reflected for the very thin sample ($10\mu m$) where the error in determining the thickness is large.

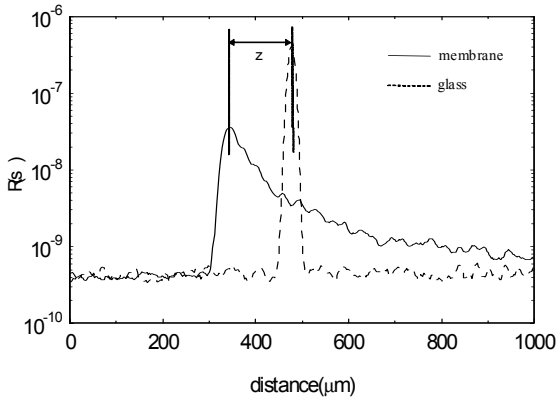

Fig 5.2. Measurement of the membrane thickness. The membrane was placed on top of a microscope slide on a $X - Y$ translation stage and the pathlength resolved reflectance of both membrane and glass was measured. The membrane thickness is calculated as the distance between the two peaks.

Table 5.1. Thickness measured with OPS as compared to the manufacturer values for different membranes

Membrane type	Mean thickness (μm)	Measured thickness (μm)
RA (mixed cellulose esters)	150	138
HVLP (polyvinylidene)	125	127
HTTP (polycarbonate)	10	20

As explained above, both the scattering cross section and the anisotropy of the scattering center depend on size and the index contrast inside the medium. Thus, if the transport mean free path is measured for two different optical contrasts inside the same medium,

the scattering center size can be determined. For this purpose $R(s)$ was measured for the membranes in two conditions, dry and wet, as presented in Figure 5.3. When the membrane is going from dry to wet, the optical contrast decreases inside the membrane, thus the scattering is decreasing and different $R(s)$ are obtained. Moreover, the shape of the reflectance is different from membrane to membrane, not only due to the difference in structure but due to the thickness difference as well.

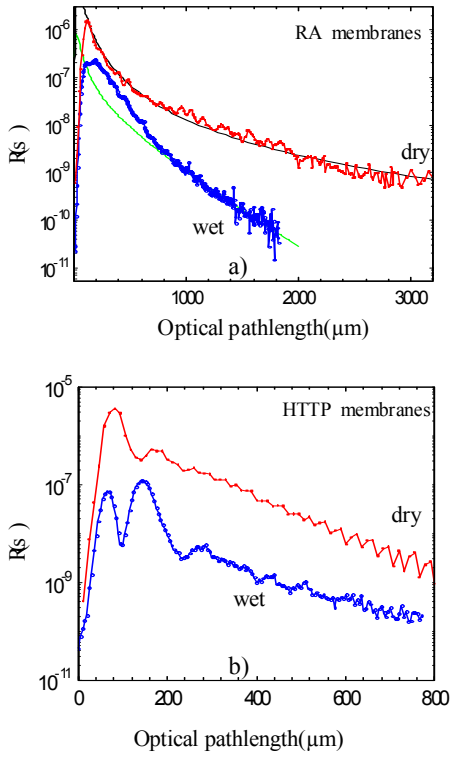

Fig 5.3. Reflectance measurements of the membrane filters in two measurement conditions dry and wet, as indicated. For the *RA* membrane (a) the continuous lines show the fit with Eq.36 for the dry case, and with Eq.37 for the wet case. For the *HTTP* membranes (b) numerical experiments must be performed to recover the experimental dependencies.

Only for the *RA*-dry membrane (Figure 5.3a), which is the thickest ($130\mu m$), the diffusion approximation and Eq.(36) can be used to fit the experimental $R(s)$. *RA*-wet,

however, has the trend given by Eq.(37). For the *HTTP*, membrane, which is very thin ($10\mu m$) only a numerical experiment can be used to recover the experimental $R(s)$. In this case, the finite thickness acts as a cutoff of the path that the photons can travel inside the membrane, thus becoming another important parameter in the membranes characterization with light scattering. A MCS was performed to assess the differences that can be observed experimentally as the thickness of the membrane decreases. The PDF used in the simulation are the ones introduced in Section 2.2.2. Reflection at the boundaries was also included. It can be observed in Figure 5.4 that as the transport mean free path becomes comparable with the thickness of the slab, $R(s)$ becomes steeper, as it was also observed experimentally.

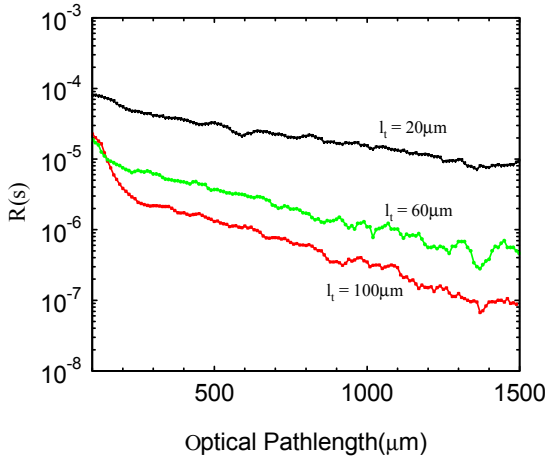

Figure 5.4. Numerical results for a slab of $130\mu m$ thickness and different values of the transport mean free path.

In conclusion, the interpretation of the experimental results require a careful analysis, as $R(s)$ is not only influenced by the scattering structure, but also by the number of scattering events that the light experiences inside the sample, i.e. the scattering regime.

In this respect, the thickness can act as a cut-off of long paths traveled inside the medium. When analytical solutions fail to recover $R(s)$, MCS becomes the only viable approach for the sample characterization, and it can also be used to design systems with desired optical properties. Moreover, measuring the pathlength resolved reflectance in porous media, one can also monitor real time structural changes.

5.1.2 Reflectance spectra of diffusive coatings

The previous study dealt with the characterization of the transport mean free path in porous media, for different scattering regimes, dictated either by the thickness or the optical contrast inside the sample. We now proceed by proposing a new characterization method for porous media which are in a multiple scattering regime and can be described by the diffusion approximation of light transport. This method uses optical measurements on a wider range of wavelengths to determine the size and PSD of a pore structure.

Predicting the optical properties of a diffuse coating from the physical parameters of the coating constituents is one of the current challenges in the paint and paper industry. Although extensive studies provided a general understanding of the pore size and pore size distribution influence on the coating optical properties, the physical measurements made on the coating constituents are still not directly linked to the light scattering observed. In this work we present an optical technique and model that can be used to probe simultaneously and non-destructively the structure and optical performance of a coating.

Kulbelka Munk (KM) description of the light propagation through an inhomogeneous media [1] has been the method of choice for the characterization of the optical properties of

a diffuse coating. The theory is based on the assumption of two diffuse fluxes traveling in the forward and backward directions. These fluxes can be described in terms of the number density and total cross section of the scattering centers, and also scattering (S) and absorption (K) coefficients. Solving the coupled equations for these two fluxes with the proper boundary conditions, the reflection and transmission of a slab of given thickness can be determined. One of the weaknesses of the theory is that the fraction of light scattered forward is considered equal to the backward one. This assumes isotropic scattering, which is not always the case. Another important weakness of the theory is that the values of S and K are not clearly related to the physical parameters of the scattering centers. Many attempts have been made to experimentally relate the KM coefficients to the transport coefficients but a general consensus in this matter has not been reached. By contrast, in the diffusion theory, as described by section 2.1.2, the physical parameters of the scattering centers are directly correlated with the optical properties of the inhomogeneous medium, and anisotropic scattering is included as well. Solving the diffusion equation with the appropriate boundary conditions, i.e. flat interface of a given refractive index contrast, the diffuse reflectance of the coating is given by Eq.27, a complicated function of the scattering and absorption coefficients, μ_s and μ_a respectively, and the anisotropy g.

Thus, if the properties of the scattering centers are known one can calculate the optical properties of the coating. Conversely, measuring the diffuse reflectance of the coating, the scattering and absorption of the inhomogeneous medium can be found through an iterative process. Since the scattering centers are not all of the same size, a size distribution (PSD) is assumed and used to calculate the effective scattering and transport coefficients

($\mu_{s-eff} = \sum_i \mu_{si}$; $\mu_{tr-eff} = \sum_i \mu_{si}(1-g_i)$) and the effective scattering anisotropy ($g_{eff} = 1 - \frac{\mu_{tr-eff}}{\mu_{s-eff}}$), which are then introduced into the previous equation to calculate the diffuse reflectance. Here i indexes the sizes within the PSD. Consequently, the effective scattering coefficient will depend on the PSD and the volume fraction f in the following manner

$$\mu_{s-eff} = f\frac{\sum_i p_i \sigma_{si}}{\sum_i p_i V_i} \tag{38}$$

where σ_{si}, p_i, V_i are the scattering cross section, normalized probability and volume of the scatterer i in the distribution, respectively.

The diffuse coatings used in the experiment consisted of a 50/50 mixture of kaolin and ground calcium carbonate deposited on a Mylar® transparent substrate. Diffuse reflectance spectra of these coatings were measured with the spectrophotometer equipped with an integrating sphere, in the configuration described in section 2.2.1. A general decreasing trend of the reflectance with the wavelength was observed over the $500-650nm$ range, as observed in Figure 5.5.

According to Eq.27, introduced in Section 4.2, depending on the size d of the scattering centers and the absorption coefficient, the shape of the reflectance spectra changes from decreasing with the wavelength for $d << \lambda$, to independent of wavelength for $d \simeq \lambda$ and finally increasing with the wavelength for $d >> \lambda$.

Comparing this general trend with the one recovered experimentally for the diffusive coatings, we can conclude that the scattering centers have to be much smaller than the wavelength. Thus, the scattering centers that will determine the optical parameters of

the coating are the micro-pores, i.e. voids in the coating structure, as the average size of the coating constituents (kaolin and calcium carbonate) is about $500nm$.

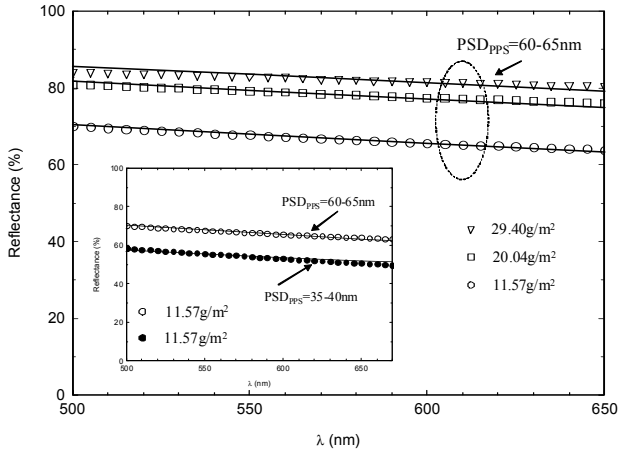

Fig. 5.5 Comparison between the reflectance spectra measured (symbols) and predicted by the diffusion approximation (continuous lines). The inset presents the differences observed and predicted for two different coatings *CM1* and *CM2* at the same coating weight.

Using an iterative procedure, the diffuse reflectance obtained in the diffusion approximation can be superimposed on the measured diffuse reflectance spectra $R(\lambda)$ (see Figure 5.5). As a result, both the concentration and the PSD of the scattering centers can be recovered, when the absorption coefficient is known. An important observation is that, for small scattering centers, the PSD dictates the slope of the $R(\lambda)$ and the concentration f the magnitude of the reflectance.

As it can be seen in Figure 5.5. the diffuse reflectance model fits very well the measured reflectance spectra, for different coating weights, i.e. concentration of scatterers, of the same coating mixture(*CM1*), and for different distributions of scatterers created by a different coating mixture (*CM2*). Moreover, the peak pore sizes needed to fit the

measured $R(\lambda)$, are very close to the ones that were obtained by a direct measure of the coating pore structure with mercury porosimetry (Table 5.2.).

The concentration of the scatterers can also be recovered from the fit of the measured $R(\lambda)$ with the diffusion model. In Table 5.3 we compare the ratios between the concentration of scatterers for different coating weight at the same coating mixture as determined by the diffusion model and the mercury porosimetry measurements.

Table 5.2. Comparison between peak pore radius of the two coatings measured.

	CM1	CM2
Pore radius by diffusion model	60-65	35-40
Pore radius by mercury porosimetry	75-80	35-40

Table 5.3 Comparison of pore volumes for different coating weights for CM1 and CM2

Coat weight (g/m^2)	$\frac{f_i}{f_{11.57}}\|_{CM1}$	$\frac{V_i}{V_{11.57}}\|_{CM1}$	$\frac{f_i}{f_{11.57}}\|_{CM2}$	$\frac{V_i}{V_{11.57}}\|_{CM2}$
11.57	1	1	1	1
20.04	1..66	1.42	1.69	1.54
29.40	2.12	1.75	2.19	1.88

where f is the pore volume fraction as determined by the diffusion model and V the total intrusion volumes as determined by mercury porosimetry.

In conclusion, it was proved that, using optical measurements on a wider range of wavelengths one can obtain information on the size distributions and the porosity of the

pore structure. Moreover, the data correlated very well with the values obtained from a traditional test method called mercury porosimetry. Although this method is currently the industry standard, it has several weaknesses, as it assumes rigid sample, is a destructive test, may induce a collapse of the coating structure that is being measured, and is time consuming. On the contrary, the optical method proposed allows for the non-invasive, real time monitoring of the coating structure. An important application of this work is the capability to forecast pigment particle types/distributions needed to optimize the performance properties of diffuse optical coatings.

5.2 Optical pathlengths in inhomogeneous media with complex structures

The previous two sections discussed the optical characterization of porous media with same scattering properties across the volume. A further complication is introduced when the scattering properties are locally different, as for example in a multilayered inhomogeneous media. Although predicting the size and size distributions of the scattering centers is increasingly difficult, we will show that one can define parameters that globally characterize the light propagation inside such samples, and that can be quantitatively related to the structure and inhomogeneity in the medium.

The inhomogeneous media under consideration are natural teeth with incipient caries lesions in the enamel. Enamel constitutes the outer layer of a tooth and has a thickness that varies in between $1 - 3mm$. Sound enamel has very high mineral content (87% hydroxyapatite-like crystals), while the rest is organic material (2%) and water (11%) [57].

As the caries lesion is developing, there is loss of mineral which results in a more porous structure than sound enamel Due to the increased inhomogeneity in carious enamel, one would expect a higher scattering coefficient [58] than in sound enamel, thus, different pathlength distributions of the waves scattered inside the two tissues. We will show in the following that the moments of these distributions can be used to quantify the differences in the scattering regimes, when the retrieval of the actual scattering and absorption coefficients is cumbersome.

5.2.1 Optical pathlength spectroscopy of incipient caries lesions

Recent investigations of the dental hard tissue with OCT and Polarization Sensitive-OCT [59], [60] provide information on the scattering properties of carious lesions. However, these techniques account only for the light which is single scattered inside the samples, and the multiply scattered light is eliminated as noise. In the following, we attempt to gain a better understanding of the multiple light scattering inside the tooth, and to evaluate how different characteristics of the sample will influence this process. Thus, commonly accepted qualitative explanations of the light interaction with the tooth can be verified, and ultimately, investigative methods can be improved.

The structure of a tooth is very complex (different layers with different optical properties and complicated boundaries) and analytical descriptions of light scattering phenomena cannot be used. Accordingly, we use OPS, described in detail in section 2.2.1, to determine experimentally the pathlength distribution of waves inside the tooth. Our

preliminary studies [61] with OPS in dental hard tissues have shown its ability to discriminate between sound enamel and carious lesions. Thus, intuitive explanations for the light propagation inside the material can be verified. Monte Carlo simulations may also be used to verify experimental results and to analyze various differences between samples.

In the second part of this section we investigate the correlations that exist between the pathlength characteristics of light waves propagating inside different caries lesions, as determined by OPS, and the properties of dental lesions determined with both QLF and transversal microradiography (TMR). Both QLF and TMR measurements have been performed by other groups. The QLF measurements were done by M.H van der Veen at Inspektor Research Systems in Amsterdam, while the slicing and the TMR measurements were done by J. Ruben at Department of Biomedical Engineering at the University of Groningen.All the further processing and analysis of data was done at the School of Optics.

QLF is a well-established method for dental lesion characterization [62]. In this method, the whole tooth is illuminated with blue light ($\sim 405nm$) which excites yellow fluorescence ($> 520nm$) in the tooth tissues. When observed in the dark through a high-pass filter with cut-off around $520nm$, the tooth appears brightly yellow. An incipient (i.e. a beginning) caries lesion, which in normal illumination appears as white spot, is visible as a dark spot. When a camera captures the image, dedicated software can quantify the loss of fluorescence from the normal value. This loss of fluorescence has been used as a measure of lesion severity, i.e. loss of mineral from the tooth enamel [63]. To explain this loss of fluorescence in lesions, it has been hypothesized [58] that the flu-

orescence predominantly originates in the enamel and, due to the increased scattering in lesions, the pathlength there is shorter than in sound enamel, which results in decreased fluorescence. This hypothesis, together with the other parameters that are influencing the QLF data are investigated.

Finally, the measured optical pathlength distributions must correlate with the physical characteristics of the lesions. For reference, TMR measurements were used, a standard quantitative contact microradiographic method in which a slice that includes the lesion is cut from the tooth (see Figure 5.6), transversely to the labial surface of the tooth [64]. The slice is microradiographed with $20KV$ X-rays on high-resolution film and from this film, the mineral content of the tooth as a function of depth is determined.

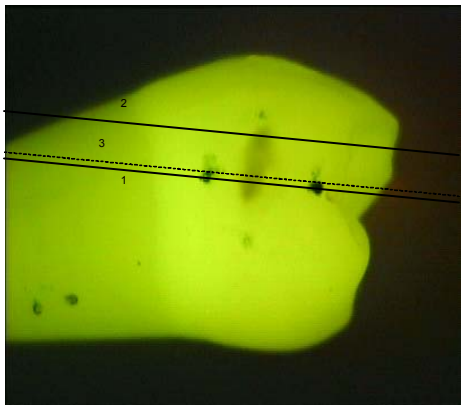

Courtesy of M.H. van der Veen and J.J. ten Bosch

Fig. 5.6 Fluorescence image of a tooth. The two cuts to prepare sections for TMR are indicated with lines 1 and 2, which are about $1mm$ apart. This thick section was further ground (800 mesh) from the side of line 2 to prepare a $80\mu m$ section for TMR, between lines 1 and 3, and thus through the lesion part used for all experiments.

To verify the above assumptions, twenty-five human premolar teeth, extracted for orthodontic reasons, were investigated with OPS. Nineteen of those teeth had incipient

lesions in the approximal surface, in different stages of demineralization, while the rest were sound. For these experiments, the bare fiber in the measuring arm of the interferometer was placed close to the tooth surface in the region of interest, and multiple scans (100) were acquired while the tooth is moved laterally over an area of $30x30\mu m$ to average the speckle. The observed separation between the reflection from the end of the fiber and the specular reflection of the tooth surface has been used to keep an approximately constant illumination distance for all samples.

For a high refractive index mismatch, especially true for sound enamel ($n = 1.6$), the amount of light delivered to the sample decreases considerably. To overcome this fact and to take advantage of the high dynamic range of the apparatus, teeth were first placed under deionized water, and the fiber tip was immersed as well, adjusted to be very close to the tooth surface. This measurement set-up is denoted in the next sections as ww - with water at tooth surface.

However, measurements were done also with the tooth kept outside of the water but still wet, to account for the high refractive index contrast at the tooth surface. To accomplish this task, each sample was measured immediately after removing it from the water. This measurement set-up is denoted in the next sections as wow - without water at tooth surface. Measuring with and without water at the surface is equivalent with changing the boundary conditions of light propagation in the bulk, as also described in Section 3.1. Consequently, it was expected that the pathlength distribution of light inside the medium change when the surface was wet or dry.

A typical result of the reflectance versus optical pathlength when the tooth is under water (ww) is presented in Figure 5.7, for the case of a sound tooth. One of the important features of this dependence is the peak at short pathlengths, which corresponds to the specular reflectance from the tooth surface. In order to obtain the pathlength distributions, the specular reflection peak is eliminated and the background noise is subtracted from the measured data. Knowing the instrumental response function of the interferometer guarantees that the elimination of the specular peak is consistent from one tooth to the next. In the end, the pathlength-resolved reflectivity is normalized with the total reflectivity, thus obtaining the density distribution of light pathlengths $P(s)$ inside the tooth as shown in the inset of Figure 5.7. The elimination of the specular peak and the normalization are necessary to compare the results from different samples without the need to take into account variations of surface reflections from one sample to the next, i.e. different incident intensities on the samples.

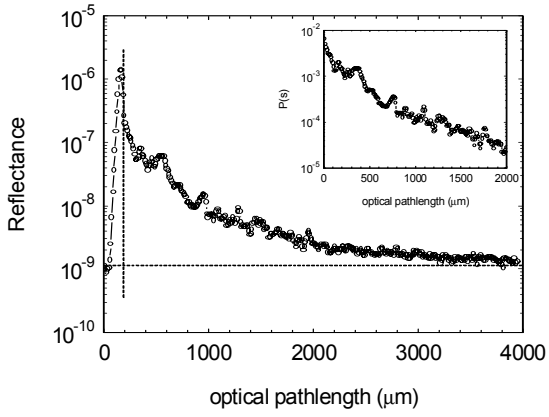

Fig 5.7 Sound tooth – typical reflectance versus optical path in the ww configuration. The specular reflectance peak is visible at short pathlengths and the noise level is indicated. The inset shows the light pathlength distribution obtained following the normalization procedure described in text.

Typical reflectance versus optical path curves for both deep and shallow incipient caries lesions in the ww configuration are presented in Figure 5.8. As we can see, there are big differences in both shape and extent of $P(s)$ when a deep versus a shallow lesion is investigated. This can be explained considering a two-layer model, where the top layer (lesion) has a higher scattering coefficient than the bottom one (sound enamel). The scattering with small optical pathlengths is stronger, but the finite thickness of the first layer acts as a cut-off, influencing the decay of the distribution at long pathlengths. In the case of a shallow lesion when the thickness of the first layer is small, the change from one scattering regime to another is very fast, thus a steeper distribution is obtained. For a deep lesion on the other hand, as the thickness of the carious layer increases, most of the scattering takes place in that layer and the distribution broadens, although diffusion is not yet achieved. A Monte Carlo simulation was performed below to substantiate this scattering model.

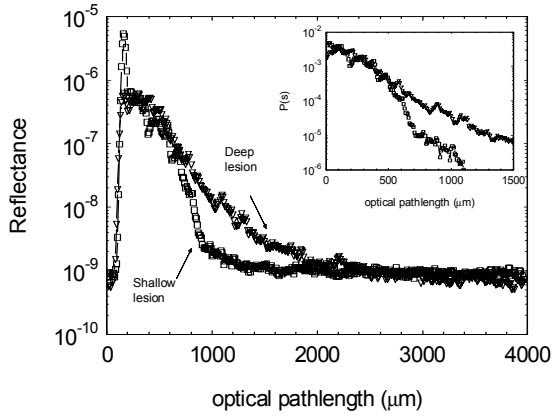

Fig. 5.8 Caries lesions – typical pathlength-resolved reflectance for both deep and shallow lesions in the ww configuration. The inset presents the normalized pathlength distributions $P(s)$. Differences in the shape and extent of the $P(s)$ distribution are clearly observed depending on the depth of lesion.

As can be seen in the inset of Figure 5.7, the direct inspection of the sound enamel $P(s)$ shows a gradual decrease in the probability to have longer and longer paths, and a penetration depth value of about $1mm$. In the carious enamel shown in Figure 5.8, on the other hand, we see a sharper decay with a penetration depth of 0.5 to $0.75mm$. This confirms the hypothesis that caries lesions have higher scattering coefficients than sound enamel.

To better quantify the scattering differences between sound enamel and lesions, the first moment, i.e. the average optical pathlength is calculated. For a semi-infinite medium, in a diffusion approximation of light transport, the average optical pathlength is influenced only by the scattering coefficient and the boundary conditions, in such a way that a higher scattering coefficient will determine a shorter average pathlength. For the complex tooth structure, the pathlength will be also influenced by the geometrical characteristics, such as number of layers, variations in scattering and refraction indexes and transversal extent of a layer. However, the scattering coefficient influence on the pathlength is still expected to be inversely proportional. When the average optical pathlength for multiple samples (6-sound and 19-lesions) is calculated and averaged, values of $0.37 \pm 0.03mm$ and $0.23 \pm 0.08mm$ are found for sound enamel and caries lesions, respectively. Thus, lesions scatter light stronger than sound enamel.

It is important to stress again that these results are obtained when the measured tooth, either sound or carious is kept under water and the refractive index contrast at the boundary is low. The value of 1.6 for the ratio between the measured average pathlengths in sound enamel and lesions is lower than the value of 2.9 for the ratio of Kubelka-Munk

scattering coefficients found by Ko et al [65]. Such a lower ratio is to be expected because we measured in the IR at a wavelength of $1300nm$, while Ko et al. used visible wavelengths where even higher scattering coefficients have been measured [58], [66], [67].

A larger variation in the average optical path is found in the case of caries lesions. This was to be anticipated because (i) biological variations have a significant role, and (ii) there are also differences in depth, transversal extent and demineralization from one caries lesion to another, which should influence the $P(s)$, hence, the average pathlength. Accordingly, the value of the average pathlength in lesions cannot be used to calculate a scattering coefficient for the lesion material, since it is a characteristic of the layered system lesion/enamel, and it is dependent on the lesion depths.

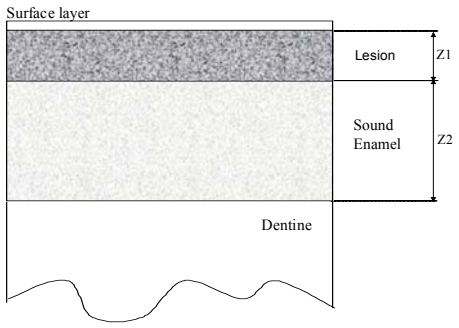

Fig. 5.9 Schematic description of the layered structure of a carious tooth. The overall thickness of the lesion and the enamel $z = (z1 + z2)$ varies from 1 to $3mm$; In the MCS, the overall thickness z is $3mm$, and the photons that escape into the dentine are not followed.

The basic geometry of a lesion is presented in Figure 5.9 and consists of a very thin surface layer, a layer formed by lesion, the sound enamel, and the dentine. The surface layer can be considered transparent for the purpose of a simulation because it is very thin

and homogeneous. The dentine can be modeled as a perfectly absorbing layer, because it is deep inside the tooth structure and its contribution to the P(s) should manifest only at long paths, which are not detected in the present experiment, being buried into the instrumental noise. Accordingly, we are left with two important layers, the lesion (1) and the sound enamel (2) with scattering coefficients $\mu_{s1/2}$, absorption coefficients $\mu_{a1/2}$, thicknesses $z_{1/2}$ and indexes of refraction $n_{1/2}$. Although all these parameters have been measured at visible wavelengths [65]-[70], for wavelengths around $1300nm$ only the attenuation coefficient of sound enamel has been measured recently [71] to be about $0.3mm^{-1}$. No data is available for the scattering coefficient for lesions at $1300nm$. Consequently, a MCS of the light propagation in the two layer system, i.e. lesion/sound enamel, can only be performed for visible wavelengths. Thus, a quantitative comparison between the experimental results and the MC simulation is not possible at this time.

For illustrative purposes, however, the simulation was performed with the measured values of the scattering coefficients at visible wavelengths ($632nm$), as it should be qualitatively indicative of the general influence of the lesions size. In the simulations, absorption [66], [67], ($\mu_a = 0.1mm^{-1}$) is considered to be the same for both the lesion and the sound enamel. The other parameters of interest chosen for the simulation are summarized in Table 5.4.

A pencil beam configuration together with commonly used probabilities for scattering and absorption length and azimuth are used in the simulations. To account for both Mie and Rayleigh scatterers present in dental enamel, the polar angle is selected from a linear combination of an isotropic scattering phase function and a Henyey-Greenstein

distribution $\phi(\cos(\theta)) = f+(1-f)\phi_{HG}(\cos(\theta))$, with $g = 0.96$ and $f = 0.35$, as determined by Fried et al. [67]. Reflection at the boundaries is accounted for using the polarization-averaged Fresnel reflection coefficient. When passing from one layer to the other, the scattering lengths are recalculated according to the specific scattering coefficients of the layers. Once the photons exit the medium, their coordinates, pathlength, and polar angle are recorded, and used to calculate the pathlength distribution, in the OPS measurement configuration.

Table 5.4. Parameters used in the MC simulation (measured for $\lambda = 632nm$)

Caries lesion	z_1/z_2	n_1/n_2	μ_{s_1}/μ_{s_2}
shallow	0.1/2.9	$1.54^a/1.6^{a,b}$	$157^c/6^b$
deep	0.3/2.7	$1.54^a/1.6^{a,b}$	$157^c/6^b$

^{a}[68]; ^{b}[67];^{c}[66].

As can be seen in Figure 5.10, the pathlength distribution in the deeper lesion decays slower than in the shallow lesion, as it was also observed experimentally in Figure 5.8. In deep lesions, the scattering process takes place primarily in the first layer. For shallow lesions, as the thickness decreases, the scattering contributions from the second layer increase. There is a rapid change from a high scattering regime to a low scattering regime, which determines a steeper distribution of optical paths, as also observed experimentally. In conclusion, the Monte Carlo simulation proves that the two-layer model for caries lesions suggested above is valid and that the qualitative assumptions made are correct.

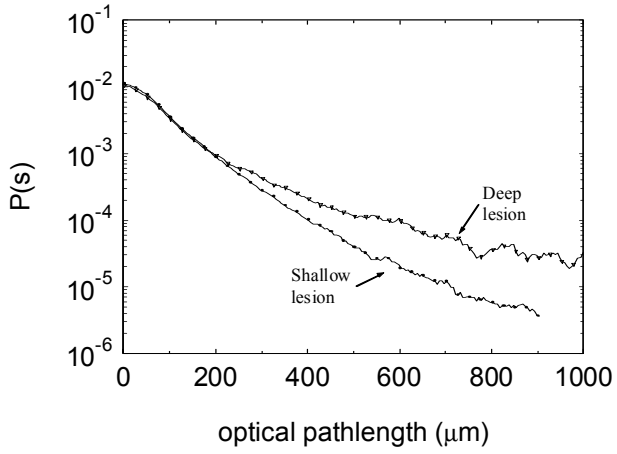

Fig. 5.10 Pathlength distribution of light simulated in both deep and shallow lesions. The simulation parameters are given in Table 5.4. The collection was made over an area of $2500\mu m^2$, with an acceptance angle smaller than 10°.The thickness of the shallow and deep lesion was $100\mu m$ and $300\mu m$ respectively.

Light fluorescence measurements in teeth have been used in the last decades to determine, non-invasively, the demineralization of carious lesions. Multiple qualitative hypotheses [62] to explain less fluorescence in lesions as compared to sound teeth have been introduced and they are mostly based on different scattering properties in the two tissues. Since OPS allows measurements of quantities that directly relate to the scattering properties of the sample under consideration, we looked for correlations between the results of the two techniques, to determine which of those hypotheses were valid.

To examine the correlations between the OPS and QLF measurements, it is important to evaluate carefully the differences between the two measurement procedures. One should consider what are the effects of different wavelengths ($1300nm$ for OPS, $404nm$ for QLF) and detection geometries (point source point detector for OPS, wide beam illumination and point detection for QLF) used for investigations. If the fluorescence process is indeed

influenced by light scattering effects inside the carious lesion, the effect should just be stronger at visible wavelengths as compared to IR, due to the higher scattering coefficients in the visible range, as was discussed before. As for the detection geometry, although a point source - point detection is used in OPS, the averaged pathlength distribution obtained is essentially three-dimensional, i.e. it is affected by the whole lesion and not by a particular injection point. When the average pathlength measured with the tooth covered with water ($< s >_{ww}$), is plotted against the maximum fluorescence loss (ΔF) measured with QLF, a very small correlation factor ($r = 0.32$) is obtained. Small improvement ($r = 0.43$) is observed when the only two discolored, i.e. brown, spots measured are removed.

Another difference in the way QLF and OPS are collecting the information stems from the boundary conditions at the tooth surface. As described previously, to reduce the reflection at the boundary in OPS, the tooth is covered completely with water and the fiber is immersed as well, such that the boundary is more or less index matched. This was most important in the case of sound teeth when the boundary reflection is very high, reducing therefore the amount of light available for being scattered inside. In QLF on the other hand, the tooth is removed from the water, the water is wiped off and the measurement is taken immediately. To study the importance of these subtle boundary effects that include both index variation and roughness, we measured the caries lesions in different conditions of refractive index contrast. The correlation in the average pathlength $< s >_{wow}$ (without water) and the fluorescence loss ΔF are presented in Figure 5.11. As can be seen, the correlation factor increases significantly, to 0.76 when the discolored spots are included

and to 0.91 when those are excluded. This remarkable increase in the correlation between average pathlength and fluorescence loss proves that the boundary effects (roughness and index contrast) are influencing the fluorescence loss and the pathlength distribution in the same manner. When the tooth is taken out of the water, the index contrast at the surface increases; due to reflections at the boundaries, the photons are re-injected into the scattering medium and longer, well-defined optical paths are developed.

The initial qualitative explanation [58] for the QLF measurements was that the longer the pathlength inside the tooth, the more fluorescence would be measured. This was hypothesized assuming that the fluorescence originated in the enamel only, the concentration of fluorescing chromophores being the same in lesions and sound enamel. Thus the longer the pathlength, the more fluorescence would be excited. Consequently, larger fluorescence loss ΔF in a lesion would imply a smaller average pathlength $< s >$. However, the correlation obtained, as it can be seen in Figure 5.11., is in the opposite direction, the more fluorescence loss the longer the path. This implies that the original hypothesis is not correct and that another common cause for both effects should be hypothesized.

The alternative explanation is based on the assumption that the fluorescence measured in QLF stems primarily from the dentin or the enamel-dentin boundary, the so-called enamel-dentin junction (EDJ). A highly scattering lesion then simply "screens" the EDJ fluorescence from being observed. One could envision in QLF a process of diffuse transmission through the multilayer structure - lesion/enamel - towards the dentine for the excitation photons and in the opposite direction for the fluorescence photons. This process is different from the one measured with OPS, which is representative for the

volume reflection of the lesion/enamel region. The high correlation that is observed experimentally between the average pathlength and the fluorescence loss in lesions should be explained by the influence of the scattering properties of the lesion on both processes. Consequently, one can consider that QLF is influenced by the overall transmission through and OPS by the integral reflection from a more or less scattering medium. When the total reflection, i.e. long OPS paths, increases, the diffuse transmission reduces and QLF signal diminishes, and high fluorescence loss is observed. Moreover, the increase in correlations observed when the discolored spots are excluded implies that the optical processes taking place in such lesions are different, as expected.

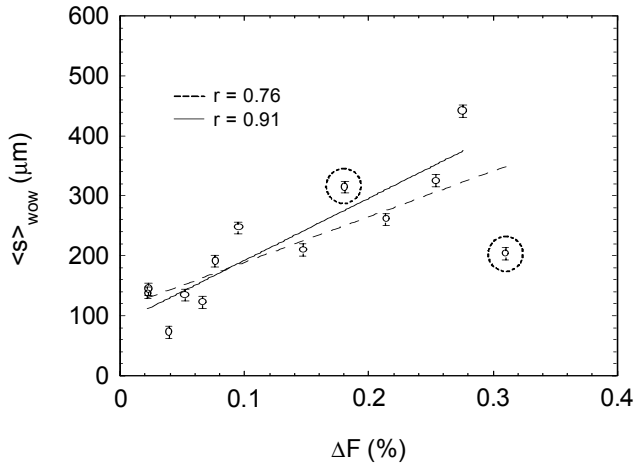

Fig. 5.11. Average pathlength (wow configuration) vs. fluorescence loss when the discolored spots are included (dashed line;$r = 0.76$) and excluded (continuous line; $r = 0.91$).

The pathlength distribution of light waves inside the caries lesion is influenced, as shown previously in measurements and simulations, by the size of the lesion (both depth and transversal extent), boundary conditions (index contrast and roughness), and the

scattering coefficients of both lesion and sound enamel. As stated previously, it has been determined [66], [67] that, at these wavelengths, the absorption coefficients are much smaller than the scattering coefficients and will not affect the path distributions up to $1 - 2cm$. One would expect the lesion scattering parameters to be influenced by the demineralization of the lesion; i.e. the more demineralized, the more porous a lesion will be. Accordingly, a direct measure of the demineralization $\Delta Z(vol\%\cdot\mu m)$ and depth $d(\mu m)$ of a caries lesion is desirable and transversal microradiography (TMR) of the carious teeth was used.

A systematic examination of the possible correlations between the average optical pathlength and the depth and demineralization of the lesions has been conducted. When the tooth is under water (ww), the correlations found are small, i.e. 0.48 and 0.47 for depth and demineralization respectively. This can be understood by realizing that both depth and demineralization are indicative of volume properties of the lesion. When in the ww configuration, due to the high scattering inside the lesion, the penetration of light is limited and, accordingly, the bulk structure of the lesion is only partially explored.

As shown in Figure 5.12, much better correlations are found when the average pathlength is measured with the tooth removed from water (wow). In this case the index contrast is higher, the light has an increased chance to be reflected back into the medium; the optical pathlengths become longer improving therefore the interaction length with the lesion. Consequently, the pathlength distribution becomes indicative of the three-dimensional bulk structure of the lesion and one could argue that the optical waves pro-

vide a better sensing mechanism for both depth and demineralization. All the correlation parameters obtained are summarized in Table 5.5.

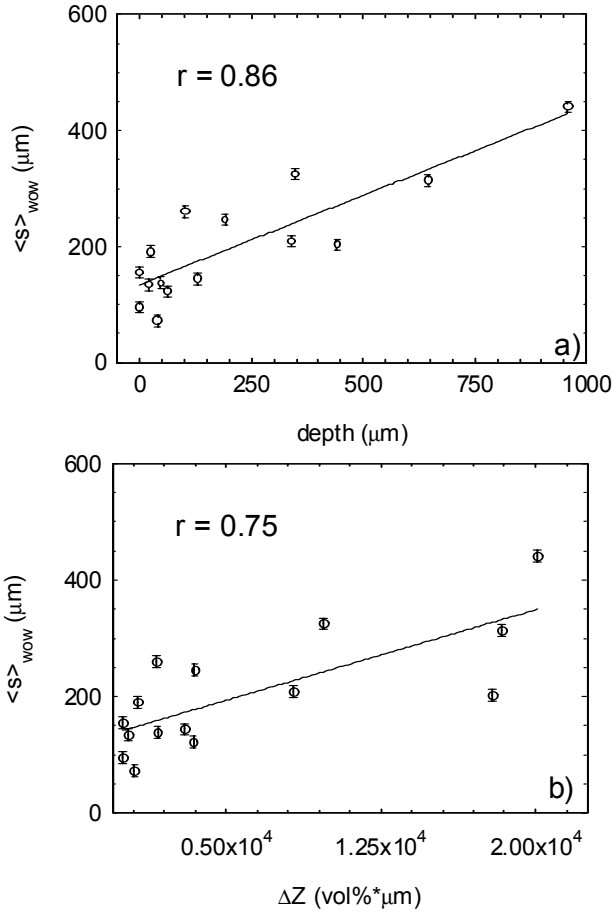

Fig. 5.12 Average pathlength (wow configuration) for different caries lesions as a function of the lesion depth (a) and demineralization (b).

In conclusion, a systematic characterization of dental caries lesions has been conducted by investigating their optical scattering properties using OPS, their fluorescence properties with QLF and finally their physical characteristics using TMR. Moreover, the comparison between the experimental investigation methods improved the understanding of the complex optical processes inside carious lesions and inspected some of the previous

assumptions. Accordingly, optical scattering provides a good sensing mechanism for both depth and demineralization of caries lesions.

Table 5.5. OPS - QLF and OPS - TMR correlations factors

Measuring configuration	<s>-ΔF	<s>-d	<s>-ΔZ
ww[1]	0.32/0.43*	0.48	0.47
wow[2]	0.76/0.91*	0.86	0.75

[1]Tooth covered with water; [2]Tooth wet but removed from water;

*Removed discolored spots.

5.2.2 The influence of drying on optical pathlengths and QLF in incipient natural caries lesions

The refractive index contrast inside the scattering sample will influence the strength of a scattering process. Thus one would expect that monitoring the refractive index contrast changes in a scattering medium could bring additional knowledge on the properties of the medium under consideration. A similar procedure was proposed in section 5.1.1, for the membrane filters characterization with OPS. Having proved above that scattering is a good sensing mechanism for the depth and demineralization of the caries lesions, we will proceed in the present section to study the effects of drying on the optical pathlengths in natural incipient caries lesions, in an attempt to non-invasively quantify the porosity of the surface layer of a lesion, and thus asses the activity of a caries lesion, i.e. the speed at which the caries process will continue in time.

As any changes in the body of the lesion will require exchange of material with the environment, lesion activity will be related to the surface layer porosity, in addition to solubility of the remaining tooth material and lesion environment such as number and kind of bacteria, sucrose and carbohydrate intake, etc. The main assumption is that the more demineralized the surface layer is, the more active is the lesion [72, 74]. Thus, in attempting to characterize lesion activity, one should be able to non-invasively provide quantitative information on the surface layer porosity.

A procedure already proposed [74] for lesion activity characterization is based on monitoring the drying process of a lesion in air, which seems to be implicitly related to the porosity of the surface layer of the lesion. QLF was chosen for these studies due to differences in light propagation in wet versus dry samples.

Because the QLF signal is related to light-scattering in the material [62, 58] and light-scattering is strongly influenced by the absence or presence of water within the pores, the drying behavior of lesions should be also detectable with more direct experimental scattering studies. Light is multiply scattered inside the incipient lesions, but, a straightforward application of a light diffusion model is not valid because the number of scattering events from the tissue is too low to assume diffusion. Moreover, description of the light interaction with the inhomogeneous medium is very difficult for such biological samples, as different scattering and absorption properties are inhomogeneously distributed, and the boundary conditions are affected by the refractive index contrast and roughness at the surface [6]. In this study, we combined measurements of the average optical pathlength by OPS with QLF of natural lesions. After these measurements lesion characteristics such as

depth (l_{lesion}) and mineral loss (ΔZ) of the lesion and thickness ($l_{surface\ layer}$) and mineral loss ($ml_{surface\ layer}$) of the surface layer (see Figure 5.13) were determined using TMR and the results were related to the time-dependence of the optical quantities.

In total 14 lesions in the approximal surface were investigated. When not being measured, teeth were stored on a wet cotton ball with some thymol to prevent bacterial growth.

In order to have some relations to clinical judgment, the appearance of the lesion was first judged visually according to Nyvad et al. [73] by two clinically trained observers from the appearance of the lesion (shiny and opaque respectively). However, in order to avoid any damage to the surface of the lesion and because visual shininess (gloss) finds its cause in surface smoothness, tactile examination was not performed. Each observer judged each lesion two and three times, respectively, at different moments in time. The fraction of opaque scores was then calculated for each lesion (for example if a lesion was judged 5 times and was found shiny 4 times, the fraction of opaque scores was 0.2). As the visual judgment will be influenced by a random confounder, this fraction is a measure of the probability that the lesion is active according to the Nyvad et al. [73] criteria.

Lesions were light-photographed and the location of most severe lesion formation according to clinical judgment was marked on the photograph. Also, four points were marked on the tooth outside the lesion with waterproof ink, such that the intersection of the lines connecting the points indicated the same site. This site was used in all measurements including TMR.

OPS measurements: The average pathlength was calculated following the procedure presented in detail before. For the drying experiment, the water was removed with a pipette and measurements were taken at intervals of $1min$ for $20min$. The teeth were not touched in order to make sure that both wet and dry measurements were taken in the same spot. No air stream was blown over the lesion. The average temperature and humidity in the laboratory were $20°C$ and 50%, respectively.

QLF and TMR measurements: The QLF measurements were done by M.H van der Veen at Inspektor Research Systems in Amsterdam. The measurements were taken following the procedure presented in detail in the previous section. For the drying experiment, a time series of QLF images of the teeth was made. At the start of the drying process the time intervals were $1s$, but increased as drying time progressed. The relative fluorescence $F_{rel}(t)$ was used for further analysis. The slicing and the TMR measurements were done by J. Ruben at Department of Biomedical Engineering at the University of Groningen. The thickness of the surface layer ($l_{surface\ layer}$), and its mineral loss ($ml_{surface\ layer}$) were estimated as shown in Figure 5.13. When no surface layer existed, $l_{surface\ layer}$ was defined 0 and the mineral loss at the surface was recorded as $ml_{surface\ layer}$. As usual, the lesion depth l_{lesion} is defined as the depth onto the 95%-of sound position, and the total mineral loss ΔZ ($Vol\% \cdot \mu m$) as the area between the measured mineral content and the line of mineral content of sound enamel. Because the transport of water is expected to be related to, or even proportional to, the 'penetrability' of the surface layer, this quantity was defined as the quotient of mineral loss from the surface layer and its thickness $penetrability = \frac{ml_{surface\ layer}}{l_{surface\ layer}}$.

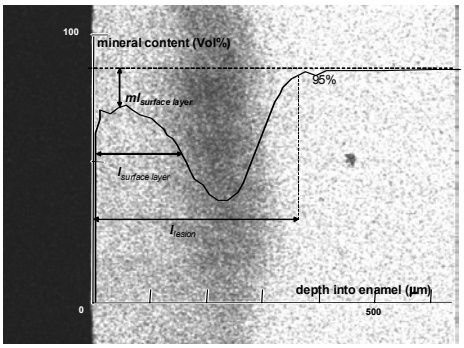

Courtesy of J.L Ruben and J.J. ten Bosch

Fig.5.13 Microradiograph and retraced microradiogram of a tooth section. The mineral loss ΔZ corresponds to the area between the dashed line and the thick full line in the microradiogram, the lesion depth l_{lesion} is defined as the depth at which the full line reaches 95%of the mineral content of sound enamel. The surface layer thickness ($l_{surface\ layer}$) and surface layer mineral loss ($ml_{surface\ layer}$) are indicated.

Drying curves were characterized with the difference between the values observed in the wet and the dry state and, whenever possible, with a decay time (t_{c-Frel}, $t_{c-<s>}$) and an initial speed of the drying curve. The decay time was obtained as follows. Decay curves without a clear plateau were fitted to single exponentials,

$$y = a \cdot \exp(-\frac{t}{t_c}) + c \tag{39}$$

with t being the drying time and a, c and t_c the fit parameters. For curves that showed an initial plateau we removed the plateau until the bending point of the curve, and fitted the remaining curve with the equation

$$y = (F_{wet} - c) \cdot \exp(-\frac{t - \Delta t}{t_c}) + c \tag{40}$$

with F_{wet} the value of the relative fluorescence at the beginning of the drying process ($t = 0$). The initial speeds of change ($\frac{dF_{rel}}{dt}|_{t=039,t=\Delta t40}$) were then calculated from the exponential fits.

To test the correlations between the different properties of the lesions and the characteristics of the drying curves, the Pearson product moment correlation coefficient r was used because a linear dependence was not excluded. Tests on instrumentally measured parameters between two groups of clinical judgment were performed with a Student t-test.

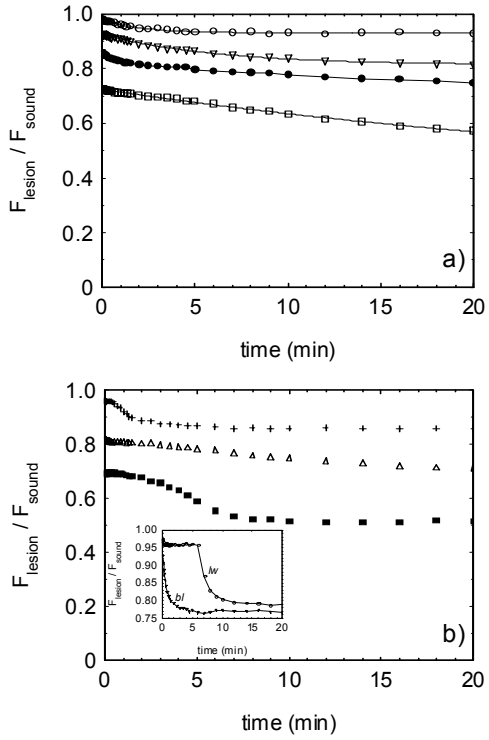

Fig.5.14 Relative fluorescence F_{rel} versus drying time for typical lesions. The full curves in Fig. 5.14a correspond to exponential decay, fitted to the points. Fig. 5.14b shows results of samples where the relative fluorescence did not follow exponential decay but started with an initial plateau. The lesions not shown follow an exponential decay of the relative fluorescence with time, similar to (a). Insert of Fig.5.14b shows a typical result of a later control experiment in which 'new' teeth were subjected to drying in air after being blotted dry (marked bl) and left wet (marked lw), respectively.

Figure 5.14 shows the time dependence of the relative fluorescence as the teeth were drying in air, determined with QLF. Most lesions showed an exponential decrease in the relative fluorescence F_{rel} (Figure 5.14a), while some started with a plateau (Figure 5.14b). The inset of Figure 5.14b shows a typical result of the control experiment for different conditions of initial drying.

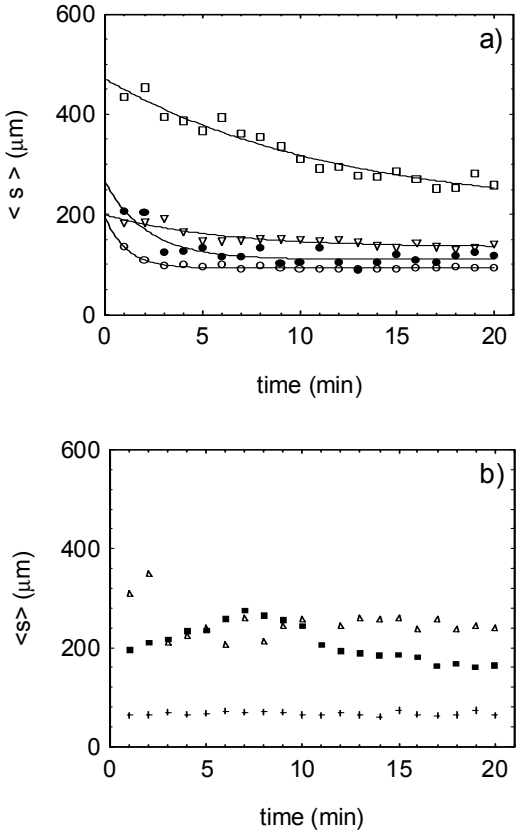

Fig.5.15 Average pathlength $< s >$ versus time of drying. For comparison, the same teeth shown in Fig. 3.18a and b are presented here, with same symbols. Again, full lines show a fit to an exponential decay.

The time dependence of the average pathlength $< s >$ as the lesion dried is presented in Figure 5.15. For comparison with the fluorescence behavior, Figures 5.15a and b show the results obtained with OPS for the same teeth as presented in Figures. 5.14a and b,

respectively. In the average pathlength we observed three different patterns of change with time when looking at different lesions. In most white spot lesions, the decay could be fitted to an exponential (Figure 5.15a). For very small, early lesions (crosses in Figure 5.15b) the average pathlength was fluctuating around an average value; the dependence was even more complicated for the investigated brown lesions (triangles and squares in Figure 5.15b).

All lesions showed a decrease in both relative fluorescence and average pathlength with the dehydration time. This was expected for the light scattering measurements because as the lesion dries, the refractive index contrast increases in the lesions, generating stronger scattering, which in turn determines a decrease in the average optical pathlength. Higher scattering also induces a lower fluorescence of the lesions, either due to the decrease in the amount of light that hits the fluorescing centers, or due to the screening of the fluorescence from the dentin or enamel-dentin boundary.

Quantitatively, it was therefore expected that the total changes over the $20min$ period could be related to the wet and dry properties of the lesion body, respectively, i.e. the amount of the water present in the wet lesion and supposedly removed in the dry lesion. Thus a relation with total mineral loss ΔZ and/or lesion depth l_{lesion} was expected. The relations of these quantities with the total changes in average pathlength $< s >$ are shown in Figures 5.16. Pearson correlation coefficients are included. The total change in relative fluorescence correlated poorly with both depth and demineralization ($r \sim 0.3$). Consequently, we conclude that fluorescence effects are mostly due to the screening by the lesion of the fluorescence from the dentin and enamel-dentin boundary. This confirms the

conclusion we reached previously based on the correlations between the average pathlength and fluorescence loss in wet lesions.

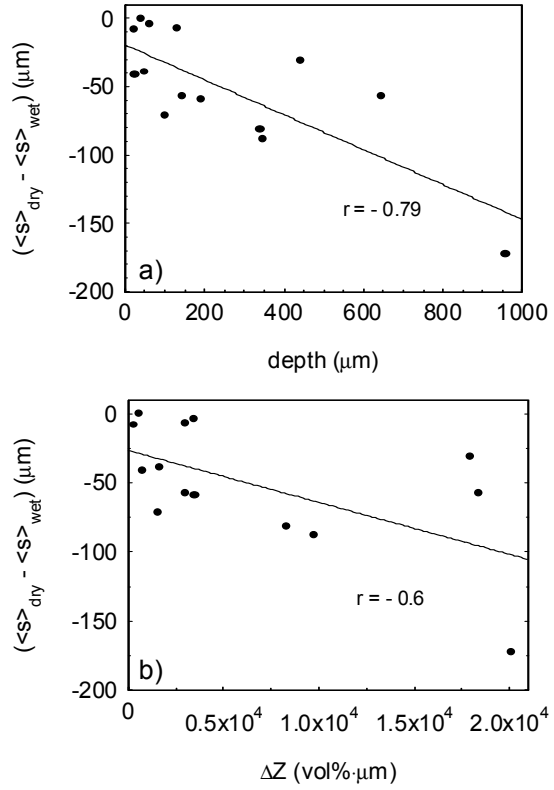

Fig.5.16 Change in average optical pathlength dry-wet versus depth l_{lesion} (a) and demineralization ΔZ (b) of lesions.

It is to be expected that the decay time of the observed optical effects of drying as a function of drying time is not only related to the amount of water present, but also to the water vapor barrier, i.e. the properties of the surface layer of the lesion.

The shape of the drying curves was analyzed on the basis of a crude theoretical model. Since scattering is dependent on the difference in refractive index of particles and the surrounding medium, and hence on water content, we applied the diffusion model for a planparallel porous sheet from which water evaporates through a permeable surface

barrier on one side of the sheet. Crank [76] gives equations for the mass evaporated from a sheet $(-l, l)$ filled with diffusive substance (diffusion constant D), with surface layer barriers on both sides. For reasons of symmetry, this is equivalent to our situation where we have a layer $(0, l)$ with a barrier at 0. We thus find that the total amount of water M_t leaving the sheet between time 0 and time t is given by the equation:

$$\frac{M_t}{M_\infty} = 1 - \sum_{n=1}^{\infty} \frac{2L^2 \exp(-\beta_n^2 Dt/l^2)}{\beta_n^2(\beta_n^2 + L^2 + L)} \tag{41}$$

In here, L is $L = l\alpha/D$ and α is a surface layer parameter, i.e. the diffusion coefficient of water vapor in the surface layer divided by the surface layer thickness. When there is no surface layer, L approaches infinity. β_n are the positive roots of $\beta tan\beta = L$ (for $L \to 0$ $\beta_n = \frac{(2n-1)\pi}{2}$) and M_∞ is the end water loss (per unit area of the sheet) at infinite time.

Eq. 41 was numerically evaluated by Carslaw and Jaeger [77] in their book on heat conduction, which process follows the same equations as diffusion. In that book, curves describing M_t/M_∞ for several values of L are given. Except for very low values of time, these curves can be approximated by an exponential decay with a dimensionless decay time $T_c(L)$.The theoretical decay time in units of time, $t_{c\ theory}$, is related to $T_c(L)$ by:

$$t_{c\ theory} = \frac{l_{lesion}^2 T_c}{D_{lesion}}$$

This model is applicable to water loss from our lesions, under several severe approximations:

i) the lesion is a plan-parallel homogeneous sheet with a surface layer;

ii) the surface layer is thin compared to the sheet thickness (lesion depth);

iii) the diffusion coefficients are proportional to the porosities of the material and thus to the mineral loss (ml, in $Vol\%$): $D_{lesion} = \lambda \cdot ml_{lesion}$ and $D_{surface\ layer} = \lambda \cdot ml_{surface\ layer}$,

in which the D's are diffusion coefficients of water in lesion and surface layer respectively, and λ a proportionality constant with equal values in lesion and surface layer;

iv) the mineral content in the lesion is homogeneous, i.e. the mineral loss (ml_{lesion} in $Vol\%$) in the lesion equals $\Delta Z/l_{lesion}$.

Under these assumptions we calculated $t_{c\ theory} \cdot \lambda$ in $\mu m^2/Vol\%$ from T_c to be:

$$t_{c\ theory} = \frac{l_{lesion}^2 T_c}{D_{lesion}}$$

Values of the experimentally obtained decay times of fluorescence during drying of the lesions are plotted in Figure 5.17 versus $t_{c\ theory} \bullet \lambda$. When the theory is applicable, this plot should show linearity.

Figure 5.17 shows that the theory is not applicable for small decay times. For large values, it may be, but supported by two points (teeth). In these teeth both the *penetrability* is low and the total mineral loss ΔZ is large. Thus, we cannot conclude whether large values of the decay time are caused by a lot of water that has to be evaporated, or to a severe surface barrier. Therefore we plotted the decay times also versus the penetrability of the lesion. Figure 5.18 gives the result for both the relative fluorescence and the average pathlength. Apparently, only small penetrability values ($\approx 0.1 vol\% \mu m^{-1}$) play a role in that they extend the decay time. This means that at higher penetrabilities the drying is not limited by the surface layer, but by the speed of water transport in the lesion itself. This conclusion is also supported by the small decay times observed for lesions where the surface layer was indistinguishable from the lesion itself. These are indicated in Figure

5.18 with arrows towards infinity because the surface thickness was zero, thus implying an infinite surface penetrability.

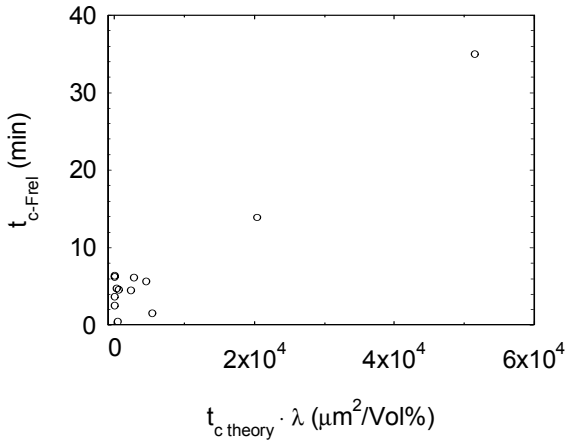

Figure 5.17 Experimental decay time of fluorescence versus $t_{c\ theory} \cdot \lambda$ predicted on the basis of a water vapor diffusion model. When the model is valid, a straight line should appear.

In conclusion, it was firstly observed that the total changes in the average pathlength correlate ($|r| > 0.6$) with the lesion bulk properties, i.e. with the total volume of water present in the lesions, while the relative fluorescence total changes do not ($r \sim 0.3$). Consequently, we conclude that fluorescence effects are mostly due to the screening by the lesion of the fluorescence from the dentin and enamel-dentin boundary. Secondly, we observed that the decay time of the drying process for the relative fluorescence seems to correlate well with a theoretical model based on water diffusion in lesion and surface layer, but only for large decay times. It cannot be decided whether these large times are due to a large lesion or to a low penetrability. The surface penetrability showed only influence on decay time for very low penetrability ($\approx 0.1 vol\% \mu m^{-1}$), i.e. a large thickness and/or

a small mineral loss of the surface layer.

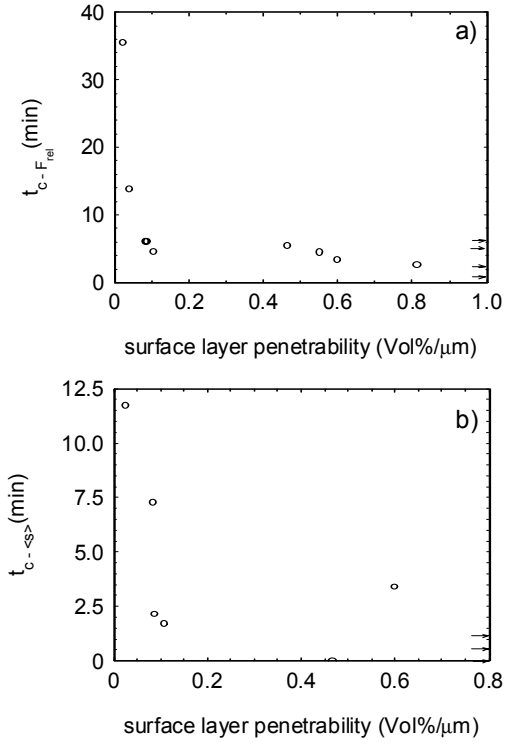

Fig. 5.18 Decay times of the relative fluorescence (a) and the average path length (b) as a function of surface penetrability. The arrows point to decay-time values at infinite penetrability, i.e. the value for lesions without a surface layer.

5.3 Discussion on chapter 5

The characterization of inhomogeneous media with complex structures has been discussed in this chapter. The methods used, optical pathlength spectroscopy and diffuse reflectance spectroscopy, recover information on the light propagation inside the inhomogeneous medium, which is implicitly related to the optical and geometrical characteristics of the sample. By modifying the index contrast inside the medium, changing the boundary conditions, and/or properly taking advantage of the experimental methods and analytical

solutions available, structural information was recovered from membrane filters, diffusive coatings and incipient lesions in natural teeth.

In the case of membrane filters, we can recover an important characteristic of the medium, the transport mean free path by fitting the pathlength resolved reflectance obtained with optical pathlength spectroscopy, either with the results of the diffuse approximation in semi-infinite or bounded media, or with distributions obtained by Monte Carlo simulations. Different approaches are necessary depending on the thickness of the membrane, as this will dictate the scattering regime in the sample.

For diffuse coatings, we have shown that, using the diffusion approximation instead of the Kubelka Munk description of light propagation, a much better understanding of the light transport can be obtained. This is true mainly because in the diffusion theory the physical parameters of the scattering centers are directly correlated with the optical properties of the inhomogeneous media. Moreover, we have shown that using optical measurements over a large range of wavelengths, one can obtain accurate information on the pore size distribution of the pore structure as well as the porosity of the medium. This non-invasive, real time optical technique is a good alternative for the current industry standard, mercury porosimetry, which is invasive, expensive and time consuming.

A basic understanding of the light scattering processes that take place inside the dental tissue (either sound or carious) was obtained using both measurements of the photon pathlength distribution of light inside such media and Monte Carlo simulations. Furthermore, correlations between different moments of the photon pathlength distribution of light inside caries lesions, the fluorescence loss determined with quantitative light fluores-

cence and/or the demineralization and depth of caries lesions determined with transversal microradiography were investigated. It was concluded that the light paths inside both carious and sound enamel are influenced considerably by the refractive index contrast at the tooth surface, as also shown in Section 4.1. Moreover, light scattering provided a good sensing mechanism for both depth and demineralization of caries lesions.

Drying effects in natural lesions were also studied with optical pathlength spectroscopy and compared to other methods currently used, with the final goal of characterizing the surface layer porosity of a caries lesions Because the refractive index contrast inside the scattering sample influences the strength of a scattering process, we considered that monitoring the refractive index contrast changes in a scattering medium could bring additional knowledge on the properties of the medium under consideration, as also proved in section 5.1.1, for the membrane filters characterization with OPS. The results were compared with clinical judgments of the lesion surface and microradiographical characterizations of the lesions. We demonstrated that water evaporation in lesions conforms to the diffusion laws only in large lesions with low surface layer penetrability.

CHAPTER 6

SUMMARY AND CONCLUSIONS

This dissertation presented novel approaches for the characterization of inhomogeneous media using light scattering techniques. Although light scattering techniques have been extensively used for characterizing inhomogeneous media, most of the previous attempts were insufficient to describe situations of practical interest, such as random media with inhomogeneous boundaries, highly scattering media with various absorption properties, and unique scattering regimes generated by sources with specific coherence properties. In this dissertation we obtained solutions for such practical problems by using novel experimental techniques complemented by either a superior modeling of the scattering phenomena or by using Monte Carlo simulations to describe experimental results that cannot be modeled theoretically.

We examined the influence of the radiative source properties on the scattering regime in the inhomogeneous media. Using a new approach based on Monte Carlo simulations, we have been able to predict the statistics of the intensity fluctuations produced when partially coherent beams propagate through scattering media. This treatment of wave phenomena should find applications in remote sensing and materials diagnostics. The appealing feature of the new method is that it can be used to provide solutions for propagation and scattering of partially coherent beams in situations that cannot be described

analytically or by approximations, such as low-order scattering and sub-diffusive regimes, or in media with strong local inhomogeneities. Moreover, once the simulation has been performed for a certain set of optical and geometrical characteristics of the medium, the statistics of the intensity fluctuations can be obtained for any value of the degree of global coherence of the input beam[2]. The influence of the temporal coherence of the source on the scattering process, and in particular the effect of radiation bandwidth on the heterodyne detection process, was also addressed. Although neglected in previous formalisms, the spectral changes induced by the scattering process are decreasing the heterodyne detection efficiency. This effect is stronger when the bandwidth of the radiation used is increased and it is dependent on the scattering system under investigation. We demonstrated that the scattering induced spectral changes also decrease the contrast obtained in a low coherence interferometric imaging system between regions with different optical properties, hence a quantitative analysis of the images needs to be carefully considered[3].

The influence of the boundaries of the inhomogeneous medium on the outcome of a scattering process was also analyzed. We have supported, with a Monte Carlo simulation, the experimental evidence that the diffusion process close to the boundary is fundamentally different from the bulk diffusion in the sense that it is affected by the scattering properties of the individual centers[4]. Hence, the extrapolation length introduced to describe the diffusion process for bounded media is not only dependent on the refractive

[2] **C. Mujat and A. Dogariu**, "*Statistics of partially coherent beams: a numerical analysis*", J. Opt. Soc. Am. A, *in press*

[3] **C. Mujat and A. Dogariu**, "*Bandwidth dependence of the heterodyne efficiency in low coherence interferometry*", submitted

[4] **G. Popescu**, **C. Mujat and A. Dogariu**, "*Evidence of scattering anisotropy effects on boundary conditions of the diffusion equation*", Phys. Rev. E 61, 2000

index contrast at the boundary, but also depends on the anisotropy of the scattering centers. It is important to acknowledge that dependence when performing a quantitative analysis of the inhomogeneous media's optical properties. We have also shown that, for rough boundaries, modeled as a single scattering layer, the spectral reflectance increases monotonically with the wavelength. Although in most previous descriptions it was customary to attribute all the spectral changes to absorption or, in the case of single scattering situations, to Mie type form factors, we have shown here that despite strong diffusion, wavelength dependence can be practically generated through a different mechanism. The implications of this effect in practical situations has been demonstrated[5].

The influence of absorption in highly scattering media was then studied. We proved the capability of optical pathlength spectroscopy to simultaneously determine the scattering and absorption coefficients, using a single measurement of the pathlength distribution of light inside the sample. Moreover, we studied, with a Monte Carlo simulation, the influence of the absorption distribution inside the sample on the pathlength distribution of light. The combined methods can be applied for discerning between absorption at the level of particulates and absorption in the host medium, and could also be used for simultaneous non-invasive determination of the complex index of refraction of a small particle[6].

The quantitative and non-invasive characterization of inhomogeneous media with complex structures, such as porous membranes, diffusive coatings, and incipient lesions in

[5] **V. Zafiropulos, C. Balas, A. Manousaki, Y. Marakis, C. Mujat and A. Dogariu**, "Yellowing effect and discoloration of pigments: experimental and theoretical studies", Journal of Cultural Heritage, 4 (Suppl.1), 249-256, (2003).

[6] **C. Mujat and A. Dogariu**, "Light absorption effects in concentrated colloidal systems", *in preparation*

natural teeth was then demonstrated. We have shown that using diffuse reflectance spectroscopy over a large range of wavelengths, one can obtain information on the size distribution as well as the porosity of the investigated pore structure[7]. This technique can be used as a non-invasive alternative to mercury porosimetry, the invasive, time consuming technique that is now the industry standard. Another application of the method is the capability to forecast pigment particle types/distributions needed to optimize the performance properties of diffuse optical coatings. A basic understanding of the light scattering processes that take place inside the dental tissue (either sound or carious) was also obtained using both measurements of the photon pathlength distribution of light inside such media and Monte Carlo simulations. Furthermore, correlations between different moments of the photon pathlength distribution of light inside caries lesions, the fluorescence loss determined with quantitative light fluorescence and/or the demineralization and depth of caries lesions determined with transversal microradiography were investigated. It was concluded that the light paths inside both carious and sound enamel are influenced considerably by the refractive index contrast at the tooth surface. Very good correlations were obtained between the optical characteristics and physical parameters of lesions when the optical measurements are performed such that there is high refractive contrast at the tooth surface. This proved that optical pathlength spectroscopy can be used for non-invasive qualitative and quantitative characterization of incipient caries lesions[8]. Drying

[7] **G. M. Freeman, D. Carter, J.N. Ishley, C. Mujat and A. Dogariu**, "Diffusion model for predicting coated paper scattering", in 2002 Coating and Graphic Arts Conference and Trade Fair Proceedings, TAPPI, 157-164, May 2002

[8] **C. Mujat, M. H. van der Veen, J.L. Ruben, J. J. ten Bosch and A. Dogariu**, "*Optical path-length spectroscopy of incipient caries lesions in relation to quantitative light fluorescence and lesion characteristics*", Appl. Opt. 42, 2003

effects in natural lesions were also studied with optical pathlength spectroscopy and quantitative light fluorescence. Results were compared with clinical judgments of the lesion surface and microradiographical characterizations of the lesions. It was concluded that fluorescence effects are mostly due to the screening by the lesion of the fluorescence from the dentin and enamel-dentin junction water evaporation in lesions conforms to the diffusion laws only in large lesions with low surface layer penetrability and the evaporation process is controlled by the surface layer only for small surface penetrabilities[9].

This dissertation presented theoretical, numerical and experimental studies on the interaction of light with different inhomogeneous media. As a result, novel approaches for the quantitative characterization of random media of practical interest have been developed.

[9] **C. Mujat, M. H. van der Veen, J.L. Ruben, A. Dogariu and J.J. ten Bosch**, "The influence of drying on QLF and optical pathlengths in incipient natural caries lesions", Caries Research, *in press*

APPENDIX A

PUBLICATIONS AND CONFERENCE PRESENTATIONS

A.1 Refereed papers

1. C. Mujat and A. Dogariu, "Bandwidth dependence of the heterodyne efficiency in low coherence interferometry", Opt. Express, *in press.*

2. C. Mujat and A. Dogariu, "Statistics of partially coherent beams: a numerical example", J. Opt, Soc. Am. A, **21** (2004), *in press.*

3. C. Mujat, M. H. van der Veen, J.L. Ruben, A. Dogariu and J.J. ten Bosch, "The influence of drying on QLF and optical pathlengths in incipient natural caries lesions", Caries Res. **251**, (2004), *in press.*

4. C. Mujat, M. H. van der Veen, J.L. Ruben, J. J. ten Bosch and A. Dogariu, "Optical path-length spectroscopy of incipient caries lesions in relation to quantitative light fluorescence and lesion characteristics", Appl. Opt. **42**, 2979 (2003).

5. V. Zafiropulos, C. Balas, A. Manousaki, Y. Marakis, P. Maravelaki-Kalaitzaki, K. Melesanaki, P. Pouli, T. Stratoudaki, S. Klein, J. Hildenhagen, K. Dickmann, B. S. Luk'Yanchuk, C. Mujat and A. Dogariu, "Yellowing effect and discoloration of pigments: experimental and theoretical studies", Journal of Cultural Heritage **4** (Suppl.1), 249 (2003).

6. A. N. Rissanou, S. H. Anastasiadis, I. A. Bitsanis, J. de Joannis, C. Mujat, and A. Dogariu, "The Information Content of Multiple Scattering Data: Monte-Carlo and Laboratory Experiments", Progr. Colloid Polym. Sci. **118**, 276 (2001).

7. G. Popescu, C. Mujat and A. Dogariu, "Evidence of scattering anisotropy effects on boundary conditions of the diffusion equation", Phys. Rev. E **61**, 4523 (2000).

A.2 Non-refereed papers

8. G. M. Freeman, D. Carter, J.N. Ishley, C. Mujat and A. Dogariu, "Diffusion model for predicting coated paper scattering", in 2002 Coating and Graphic Arts Conference and Trade Fair Proceedings, TAPPI, 157 (2002).

9. B. T. Amaechi, A. G. Podoleanu, C. Mujat, A. Dogariu, S. M. Higham, D. A. Jackson, "Optical Coherence Tomography correlated with a functional fluorescence imaging for detection and quantification of dental caries", in Proc. SPIE **4619**, 253 (2002).

10. C. Mujat, M. van der Veen, J.J ten Bosch and A. Dogariu, "Dental caries characterization with optical pathlength spectroscopy", in OSA Technical Digest - Biomedical Topical Meetings, OSA, (Optical Society of America, Washington DC 2002), 397 (2002).

11. C. Mujat, J.J. ten Bosch and A. Dogariu, "Optical pathlengths in dental caries lesions", in Lasers in Dentistry VII, P. Rechmann, D. Fried and T. Hennig, eds., Proc. SPIE **4249**, 92 (2001).

12. C. Mujat, L. Denney and A. Dogariu, "Optical characterizations of porous membranes", in MRS Symposium Proceedings **613**, E6.10.1 (2000).

A.3 Conference presentations

13. C. Mujat, M. H. van der Veen, J. L. Ruben, A. Dogariu, J. J. ten Bosch, "QLF and OPS investigation of drying in natural incipient caries lesions", to be presented at Biomed 2004, April 14-17, 2004 – *poster presentation*

14. C. Mujat and A. Dogariu, “Statistics of partially coherent beams propagating through scattering media – a numerical approach”, to be presented at Biomed 2004, April 14-17, 2004 – *poster presentation*

15. C. Mujat and A. Dogariu, "Numerical analysis of partially coherent beams propagating in inhomogeneous media", presented at the OSA Annual Meeting, Orlando, Sept.29 - Oct. 3, 2002 – *oral presentation*

16. C. Mujat, M. H. van der Veen, J. L. Ruben, A. Dogariu, J. J. ten Bosch, "The influence of drying on QLF and optical path lengths in incipient natural caries lesions", presented at the 49th Annual Congress of the European Organization for Caries Research - ORCA 2002, Naantali, Finland, July 3-6, 2002 – *poster presentation*

17. C. Mujat and A. Dogariu, "Light absorption effects in concentrated colloidal systems", presented at the 223rd ACS National Meeting–Orlando, Florida, April 7-11, 2002 – *oral presentation*

18. G. Popescu, C. Mujat and A. Dogariu, "Optical pathlength spectroscopy of multiple-scattering media", presented at the OSA annual meeting, Santa Clara, Sept. 26-Oct.1, 1999 – *oral presentation*

LIST OF REFERENCES

[1] A. Ishimaru, "Wave propagation and scattering in random media", Academic Press (1978).

[2] H.C. van de Hulst, "Light scattering by small particles", Dover Publications Inc. (1981).

[3] C.F. Bohren and D.R. Huffman, "Absorption and scattering of light by small particles", JonnWiley and Sons (1983).

[4] S. Chandrasekhar, "Radiative transfer", Oxford Univ. Press London (1950).

[5] G. Popescu and A. Dogariu, "Optical path-length spectroscopy of wave propagation in random media," Opt. Lett. **24**, 442 (1999).

[6] G. Popescu, C. Mujat, and A. Dogariu, "Evidence of scattering anisotropy effects on boundary conditions of the diffusion equation," Phys. Rev. E **61**, 4523 (2000).

[7] G. Popescu and A. Dogariu, "Dynamic light scattering in subdiffusive regimes," Appl. Opt. **40**, 4215 (2001).

[8] B.C. Wilson and G. Adam, "A Monte Carlo model for the absorption and flux distributions of light in tissue", Med. Phys. **10**, 824 (1983).

[9] S.T. Flock, M.S. Patterson, B.C Wilson and D. R. Wyman, "Monte Carlo modeling of light propagation in highly scattering tissues-I. Model predictions and comparison with diffusion theory", IEEE Transactions on Biomedical Engineering **36**, 1162 (1989).

[10] L.H. Wang, S.L. Jacques and L.Q. Zheng, " MCML - Monte Carlo modeling of light transport in multi-layered media", Computer methods and Programs in Biomedicine **47**, 131 (1995).

[11] L.G. Henyey and J.L. Greenstein, "Diffusion radiation in the galaxy", Astrophys. J. **93**, 70 (1941).

[12] G. Gbur and E. Wolf, "Spreading of partially coherent beams in random media", J. Opt. Soc. Am. A **19**, 1592 (2002).

[13] A. Dogariu and S. Amarande, "Propagation of partially coherent beams: turbulence-induced degradation", Opt. Lett. **28**, 10 (2003)

[14] Y. Pan, R. Birngruber, J. Rosperich and R. Engelhardt, "Low-coherence optical tomography in turbid tissue: theoretical analysis", Appl. Opt. **34**, 6564 (1995).

[15] J.M. Schmitt and A. Knüttel, "Model of optical coherence tomography of heterogeneous tissue", JOSA A **14**, 1231 (1997).

[16] D. Levitz, L. Thrane, M.H. Frosz, P.A. Andersen, C.B. Andersen, J. Valanciunaite, J. Swartling and S. Andersson-Engels, P.R. Hansen, "Determination of the optical scattering properties of highly scattering media in optical coherence tomography images", Opt. Express **12**, 249 (2004).

[17] M.U. Vera, P.A. Lemieux, and D.J. Durian, "Angular distribution of diffusively backscattered light", J. Opt. Soc. Am. A **14**, (1997).

[18] E. Amic, J.M. Luck, and Th. M. Nieuwenhuizen, "Anisotropic multiple scattering in diffusive media", J. Phys. A: Math. Gen. **29**, (1996).

[19] Nan Guang Chen and Jing Bai, "Monte Carlo approach to modeling of boundary conditions for the diffusion equation", Phys. Rev. Lett. **80**, 5321 (1998).

[20] Lenke R and Maret G, in *Scattering in Polymeric and Colloidal Systems*, ed. W. Brown and K. Mortensen, (Gordon and Breach Science Publishers, Amsterdam, 2000), pp.1-73.

[21] J. Schmitt, A. Knuttel, and M. Yadlowski, "Confocal microscopy in turbid media", J. Opt. Soc. Am. A **11**, 2226 (1994).

[22] V.R. Daria, C. Saloma and S. Kawata, "Excitation with a focused, pulsed optical beam in scattering media: diffraction effects", Appl. Opt. **39**, 5244 (2000).

[23] L.V. Wang, "Mechanisms of ultrasonic modulation of multiply scattered coherent light: a Monte Carlo model", Opt. Lett. **26**, 1191 (2001).

[24] A. Tycho and T.M. Jorgensen, "Comment on "Excitation with a focused, pulsed optical beam in scattering media: diffraction effects"", Appl. Opt. **41**, 4709 (2002).

[25] E. Baleine and A. Dogariu, "Propagation of partially coherent beams through particulate media", J. Opt. Soc. Am. A **20**, 2041 (2003).

[26] E. Wolf, "A new description of the second order coherence phenomena in the space frequency domain," in *Conference proceedings #65 -Optics in four dimentions-1980, ICO, Ensenada*, M.A Machada and L.M. Narducci, eds., American Institute of Physics, New York, (1981), pp. 42-48.

[27] L. Mandel and E. Wolf, *Optical Coherence and Quantum Optics*, Cambridge Univ. Press, NY, (1995) pp. 276-287.

[28] J.C Dainty, *Laser speckle and related phenomena*, Springer-Verlag, Berlin, Heidelberg, New York, (1975).

[29] H. Fuji and T. Asakura, "Statistical properties of image speckle patterns in partially coherent light", Nouv. Rev. Optique **6**, 5 (1975).

[30] D. Huang, E. Swanson, C.P. Lin, J.S. Schuman, W.G. Stinson, W. Chnag, M.R. Hee, T. Flotte, K. Gregory, C.A. Puliafito, and J.G. Fujimoto, "Optical coherence tomography", Science **254**, 1178 (1991).

[31] W. Drexler, U. Morgner, F.X. Kärtner, C. Pitris, S.A. Boppart, X.D. Li, E.P. Ippen, and J.G. Fujimoto " *In vivo* ultrahigh-resolution optical coherence tomography", Opt. Lett. **24**, 1221 (1999).

[32] G. R. Osche, "Optical detection theory for laser applications", Wiley Series in Pure and Applied Optics, (2002).

[33] E. Wolf and D.F.V. James, "Correlation induced spectral changes", Rep. Prog. Phys. 59, 771-812 (1996).

[34] A. Dogariu and E. Wolf, "Spectral changes produced by static scattering on a system of particles", Opt. Lett. **23**, 1340 (1998).

[35] J.M. Schmitt and G. Kumar, "Optical scattering properties of soft tissue: a discrete particle model", Appl. Opt. **37**, 2788 (1998).

[36] A. Dogariu, "Volume scattering in random media," in Handbook of Optics, vol III, M. Bass, J.M Enoch, E.W. van Stryland and W. Wolfe, eds. (McGraw-Hill, New York, NY, 2001), pp. 3.1-3.18.

[37] M.C.W. van Rossum, Th. M. Nieuwenhuizen, "Multiple scattering of classical waves: microscopy, mesoscopy, and diffusion", Rev. Mod. Phys. **71**, (1999).

[38] M. S. Patterson, B. Chance and B.C. Wilson, "Time resolved reflectance and transmittance for the noninvasive measurement of tissue optical properties", Appl. Opt. **28**, 2331 (1989).

[39] M.U. Vera and D. J. Durian, "Angular distribution of diffusely transmitted light", Phys Rev. E **53**, 3215 (1996).

[40] J.F. Asmus, M. Seracini and M.J. Zetler, "Surface morphology of laser cleaned stone", Lithoclastia **1**, (1976).

[41] S. J. Madsen, B.C. Wilson, M.S. Patterson, Y.D. Park, S.L. Jacques and Y. Hefetz, "Experimental tests of a simple diffusion approximation for the estimation of scattering and absorption coefficients of turbid media from time-resolved diffuse reflectance measurements", Appl. Opt. **31**, 3509 (1992).

[42] J. Farrell, B.C. Wilson and M.S. Patterson, "The use of a neural network to determine tissue optical properties from spatially resolved diffuse reflectance measurements", Phys. Med. Biol. 37, 2281 (1992).

[43] S.J. Madsen, E.R. Anderson, R.C. Haskell and B.J. Tromberg, "Portable, high bandwidth frequency domain photon migration instrument for tissue spectroscopy", Opt. Lett. 19, 1934 (1994).

[44] M. Kohl, R. Watson and M. Cope, "Determination of absorption coefficients in highly scattering media from changes in attenuation and phase", Opt. Lett. **21**, 1519 (1996).

[45] R. Aronson, N. Corngold, "Photon diffusion coefficient in an absorbing medium", J.Opt. Soc. Am. A 16, 1066-1071, 1999.

[46] D.J. Durian, "The diffusion coefficient depends on absorption", Opt. Lett 23, 1502-1504, 1998.

[47] R. Graaff and J.J ten Bosch, "Diffusion coefficient in photon diffusion theory", Opt. Lett. 25, 2000.

[48] R. Elaloufi, R. Carminati and J.J. Greffet, "Definition of the diffusion coefficient in scattering and absorbing media", J. Opt. Soc. Am. A 20, 678-685, 2003.

[49] K. Furutsu and Y. Yamada, "Diffusion approximation for a dissipative random medium and the applications", Phy. Rev. E 50, 3634-3640, 1994.

[50] M. Basani, F. Martelli and G. Zaccanti, "Independence of the diffusion coefficient from absorption: experimental and numerical evidence", Opt. Lett. 22, 853-855, 1997.

[51] T. Durduran et al., "Does the photon diffusion coefficient depend on absorption", J. Opt. Soc. Am. A 14, 3358-3365, 1997.

[52] T. Nakai et al., "Expression of optical difusion coefficient in high-absorption turbid media", Phys. Med. Biol. 42, 2541-2549, 1997.

[53] F.A. L. Dullien, "Porous Media - Fluid Transport and Pore Structure", Academic Press, San Diego (1992).

[54] J. Rouquerol, F. Rodriguez-Reinoso, K.S.W. Sing and K.K. Unger (ed.), "Characterization of Porous Solids III", Elsevier, The Netherlands (1994).

[55] L. Cipelletti, M. Carpineti and M. Gioglio, "Microporous membrane filters: a static light scattering study", Physica A **235**, 248 (1997).

[56] D. Contini, F. Martelli, and G. Zaccanti, "Photon migration through a turbid slab described by a model based on diffusion approximation. I. Theory", Appl. Opt. **36**, 4567 (1997).

[57] G.N. Jenkins, The physiology and biochemistry of the mouth (Blackwell Scientific, Oxford, 54-112, 1978).

[58] J.J. ten Bosch, "Light scattering and related methods in caries diagnosis", in Early Detection of Dental Caries I, Proceedings of the 1st annual Indiana Conference, G. Stookey, ed. (Indianapolis, Indiana University School of Dentistry, 1996), pp. 81-90.

[59] D. Fried et al., "Imaging caries lesions and lesion progression with polarization sensitive optical coherence tomography", in Lasers in Dentistry VIII, P. Rechmann, D. Fried and T. Henning, eds., Proc. SPIE **4610**, 113 (2002).

[60] B. T. Amaechi et al., "Optical coherence Tomography for dental caries detection and analysis", in Lasers in Dentistry VIII, P. Rechmann, D. Fried and T. Henning, eds., Proc. SPIE **4610**, 100 (2002).

[61] C. Mujat, J.J. ten Bosch and A. Dogariu, "Optical pathlengths in dental caries lesions", in Lasers in Dentistry VII, P. Rechmann, D. Fried and T. Hennig, eds., Proc. SPIE **4249**, 92 (2001).

[62] B. Angmar-Månsson and J.J. ten Bosch, "Quantitative light-induced fluorescence (QLF): a method for assessment of incipient caries lesions," Dentomaxillofac. Radiol. **30**, 298 (2001)..

[63] J.J. ten Bosch, "Summary of research of quantitative light-induced fluorescence", in Early Detection of Dental Caries II, Proceedings of the 4th annual Indiana Conference, G. Stookey, ed. (Indianapolis, Indiana University School of Dentistry, 2000), pp. 261-277.

[64] M.D. Lagerweij, E. de-Josselin-de-Jong, J. ten-Cate, "The video camera compared with the densitometer as a scanning device for microradiography," Caries-Res. **28**, 353 (1994).

[65] C.C. Ko, D. Tantbirojn, T. Wang, and W.H. Douglas, "Optical scattering power for characterization of mineral loss," J. Dent. Res. **79**, 1584 (2000).

[66] D. Spitzer and J.J. ten Bosch, "Luminescence quantum yields of sound and carious enamel," Calcif. Tissue Res. **24**, 249 (1977).

[67] D. Fried, R.E. Glena, J.B. Featherstone and W. Seka, "Nature of light scattering in dental enamel and dentin at visible and near-infrared wavelengths," App. Opt. **34**, 1278 (1995).

[68] J.R Zijp, Optical properties of dental hard tissues, Doctoral Dissertation, University of Groningen, the Netherlands, (2001).

[69] D. Spitzer and J.J. ten Bosch, "The absorption and scattering of light in bovine and dental human enamel," Calcif. Tissue Res. **17**, 129 (1975).

[70] J. Vaarkamp, J.J. ten Bosch and E.H. Verdonschot, "Propagation of light through human dental and dentine," Caries Res. **29**, 8 (1995).

[71] R. Jones and D. Fried, "Attenuation of 1310-nm and 1550-nm laser light through sound enamel", in Lasers in Dentistry VIII, P. Rechmann, D. Fried and T. Henning, eds., Proc. SPIE **4610**, 187 (2002).

[72] K. Kaneko, K. Matsuyama, S. Nakashima, "Quantification of early carious enamel lesions by using an infrared camera in vitro" in: G.K. Stookey, Ed. Early detection of dental caries II. Indianapolis, Indiana University School of Dentistry, 2000; pp 83-99.

[73] B. Nyvad, V. Machiulskiene, V. Baelum, "Reliability of a new caries diagnostic system differentiating between active and inactive caries lesions", Caries Res. **33**, 252 (1999)..

[74] S. Al-Khateeb, R.A. Exterkate, E. de Josselin de Jong, B. Angmar-Månsson, J.M. ten Cate, "Light-induced fluorescence studies on dehydration of incipient enamel lesions", Caries Res **36**, 25 (2002).

[75] D. Inaba, O. Takagi, J. Arends, "A computer-assisted videodensitometric method to visualize mineral distributions in vitro and in vivo formed root caries lesions", Eur. J. Oral Sci. **105**, 74 (1997).

[76] J. Crank, "The mathematics of diffusion", Clarendon Press, Oxford, U.K (1975).

[77] H.S. Carslaw, J.C. Jaeger, "Conduction of heat in solids", 2nd ed. Clarendon Press, Oxford, UK (1959), pp 119-125.